UNIVERSIDADE FEDERAL DE MINAS GERAIS - UFMG
Instituto de Ciências Exatas - ICEX
Programa de Pós-Graduação em Física

Alan Custódio dos Reis Souza

AB INITIO INVESTIGATIONS IN TWO-DIMENSIONAL NANOMATERIALS:

Electronic and structural properties

Belo Horizonte
2022

Alan Custódio dos Reis Souza

AB INITIO INVESTIGATIONS IN TWO-DIMENSIONAL NANOMATERIALS:

Electronic and structural properties

Tese apresentada ao Programa de Pós-Graduação em Física do Instituto de Ciências Exatas da Universidade Federal de Minas Gerais como requisito parcial para obtenção do título de Doutor em Física.

Orientador: Mario Sérgio de Carvalho Mazzoni

Coorientador: Matheus Josué de Souza Matos

Belo Horizonte

2022

Dados Internacionais de Catalogação na Publicação (CIP)

S729a Souza, Alan Custódio dos Reis.
Ab initio investigations in two dimensional nanomaterials: electronic and structural properties / Alan Custódio dos Reis Souza. – 2022.
85f., enc. : il.

Orientador: Mário Sérgio de Carvalho Mazzoni.
Coorientador: Matheus Josué de Souza Matos.
Tese (doutorado) – Universidade Federal de Minas Gerais, Departamento de Física.
Bibliografia: f. 67-81.

1. Nanomateriais. 2. Teoria do Funcional da Densidade. 3. Fônons. I. Título. II. Mazzoni, Mário Sérgio de Carvalho. III. Universidade Federal de Minas Gerais, Departamento de Física.

CDU – 620.3 (043)

Ficha catalográfica elaborada por Romário Martins Ribeiro – CRB6 3595
Biblioteca Professor Manoel Lopes de Siqueira – Departamento de Física - UFMG

UNIVERSIDADE FEDERAL DE MINAS GERAIS
INSTITUTO DE CIÊNCIAS EXATAS
PROGRAMA DE PÓS-GRADUAÇÃO EM FÍSICA

ATA DE DEFESA DE TESE

ATA DA SESSÃO DE ARGUIÇÃO DA 403ª TESE DO PROGRAMA DE PÓS-GRADUAÇÃO EM FÍSICA, DEFENDIDA POR ALAN CUSTODIO DOS REIS SOUZA, orientado pelo professor Mario Sérgio de Carvalho Mazzoni e coorientado pelo professor Matheus Josué de Souza Matos, para obtenção do grau de **DOUTOR EM CIÊNCIAS, área de concentração física**. Às 9:00 horas de trinta de agosto de dois mil e vinte e dois reuniu-se, por videoconferência, a Comissão Examinadora, composta pelos professores **Mario Sérgio de Carvalho Mazzoni** (Orientador - Departamento de Física/UFMG), **Matheus Josué de Souza Matos** (Coorientador - Departamento de Física/UFOP), **Ricardo Wagner Nunes** (Departamento de Física/UFMG), **Ariete Righi** (Departamento de Física/UFMG), **Roberto Hiroki Miwa** (Universidade Federal de Uberlândia) e **Solange Binotto Fagan** (Universidade Franciscana – UNIFRA/RS) para dar cumprimento ao Artigo 37 do Regimento Geral da UFMG, submetendo o Mestre **ALAN CUSTODIO DOS REIS SOUZA** à arguição de seu trabalho de Tese de Doutorado, que recebeu o título de **"Ab initio investigations in two dimensional nanomaterials: Electronic and structural properties"**. O candidato fez uma exposição oral de seu trabalho durante aproximadamente 50 minutos. Após esta, os membros da comissão prosseguiram com a sua arguição, e apresentaram seus pareceres individuais sobre o trabalho, concluindo pela aprovação do candidato.

Belo Horizonte, 30 de agosto de 2022.

Prof. Mario Sérgio de Carvalho Mazzoni	Prof. Matheus Josué de Souza Matos
Orientador do estudante	Coorientador do estudante
Departamento de Física/UFMG	Departamento de Física/UFOP
Prof. Ricardo Wagner Nunes	Profa. Ariete Righi
Departamento de Física/UFMG	Departamento de Física/UFMG
Prof. Roberto Hiroki Miwa	Profa. Solange Binotto Fagan

Universidade Federal de Uberlândia Universidade Franciscana - UNIFRA/RS

Candidato: Alan Custodio dos Reis Souza

Documento assinado eletronicamente por **Alan Custodio dos Reis Souza**, **Usuário Externo**, em 01/09/2022, às 09:32, conforme horário oficial de Brasília, com fundamento no art. 5º do Decreto nº 10.543, de 13 de novembro de 2020.

Documento assinado eletronicamente por **Ariete Righi**, **Professora do Magistério Superior**, em 01/09/2022, às 10:44, conforme horário oficial de Brasília, com fundamento no art. 5º do Decreto nº 10.543, de 13 de novembro de 2020.

Documento assinado eletronicamente por **Solange Binotto Fagan**, **Usuário Externo**, em 01/09/2022, às 11:01, conforme horário oficial de Brasília, com fundamento no art. 5º do Decreto nº 10.543, de 13 de novembro de 2020.

Documento assinado eletronicamente por **Mario Sergio de Carvalho Mazzoni**, **Membro**, em 01/09/2022, às 12:21, conforme horário oficial de Brasília, com fundamento no art. 5º do Decreto nº 10.543, de 13 de novembro de 2020.

Documento assinado eletronicamente por **Roberto Hiroki Miwa**, **Usuário Externo**, em 01/09/2022, às 12:37, conforme horário oficial de Brasília, com fundamento no art. 5º do Decreto nº 10.543, de 13 de novembro de 2020.

Documento assinado eletronicamente por **Matheus Josué de Souza Matos**, **Usuário Externo**, em 01/09/2022, às 12:50, conforme horário oficial de Brasília, com fundamento no art. 5º do Decreto nº 10.543, de 13 de novembro de 2020.

A autenticidade deste documento pode ser conferida no site https://sei.ufmg.br/sei/controlador_externo.php?acao=documento_conferir&id_orgao_acesso_externo=0, informando o código verificador **1726650** e o código CRC **532FA82A**.

Referência: Processo nº 23072.252357/2022-47 SEI nº 1726650

Este trabalho é dedicado aos meus pais, seu Carlinhos e dona Rodriga.

Agradecimentos

Esse trabalho só foi possível devido a um esforço colossal de diversas pessoas, de forma direta e indiretamente. Sr. Isaac Newton uma vez disse que se ele enxergou mais longe foi porque estava apoiado nos ombros de gigantes, e eu posso dizer com convicção que compartilho desse sentimento. Claro que eu não comparo as realizações desse doutorado com as de Newton (afinal eu sou um mero mortal comparado a ele), mas para um jovem da periferia de São Paulo, filho de pais nordestinos sem formação básica, chegar até esse ponto em uma das melhores universidades do Brasil, foi necessário muita luta coletiva.

Logo, eu gostaria de agradecer primeiramente as pessoas mais importantes da minha vida: seu Carlinhos e Dona Rodriga. Vocês sacrificaram tudo para que eu pudesse ter o que vocês nunca tiveram oportunidade, são meus heróis e minha motivação diária. A vocês eu devo tudo e por vocês eu sou o que sou hoje.

Eu gostaria de agradecer ao Mário por todos esses anos de orientação. Ele desempenhou um papel que, com certeza, vai muito além da formação acadêmica, sendo sempre um amigo, um conselheiro e me ajudando de formas que me permitiram finalizar esse doutorado. Muito obrigado por tudo.

Também agradeço ao Matheus pela coorientação, pela amizade, pelas discussões, pelos ensinamentos, pelos cafés e pela ajuda para compilar cada programa.

Deixo registrado também meu agradecimento ao Prof. Vincent Meunier que orientou nos Estados Unidos e que tive o privilégio de desenvolver um dos projetos dessa tese. Agradeço ao Maurício e ao Café por me acolherem enquanto estive nos EUA e que fizeram a minha experiência com o doutorado sanduíche muito melhor.

Agradeço enormemente aos meus professores, desde a graduação, o Léo, Natália, Romeu e Douglas pelas aulas e ensinamentos, ao Fabrício e ao Robson pela orientação durante tantos anos, pelos conselhos e ajuda. Aos professores da UFMG Reinaldo, Dickman, Rachid, Walber e Ado pelas aulas.

Agradeço aos meus amigos, que estão aqui e que já partiram, Black, Henrique, Bravim, Kassio, Titu, Peu, Aislan, David, Deivide, Latino, Vinicius (Boiologia), Léo Blue Eyes, George, Paulinho, Pedrinho, Tulio, Miguilin, Orlando, Nestor, Samuca, Idaiane, Natália, Guilherme, Isaac, Vitor, Vitão, Gustavo, Joãozinho, Maria Clara, Maria Eduarda, Jéssica e ao trenzin mais lindo do mundo chamada Tamires. Todos vocês contribuíram para que este momento acontecesse.

Também não poderia deixar de agradecer a Vaninha e ao melhor bar de Minas Gerais, o Cabral's Bar.

Agradeço a CAPES pelo apoio financeiro e a Fulbright por viabilizar meu doutorado sanduíche nos EUA mesmo durante a pandemia de Covid.

Resumo

A busca por novos materiais bidimensionais com propriedades adequadas para aplicações tecnológicas reúne um interesse cada vez maior dentro da comunidade de matéria condensada. De fato, é de grande importância a utilização de métodos teóricos para investigar as propriedades eletrônicas e estruturais desses materiais, dado que os mesmos podem apresentar uma série de propriedades exóticas com grande interesse físico e químico. Uma das teorias de maior sucesso nessa área é a teoria do funcional da densidade, que permite a investigação de nanomateriais sem a utilização de parâmetros empíricos e com excelente eficiência computacional. Buscamos nessa tese empregar a teoria do funcional da densidade para estudar a versão bidimensional do antimônio (o antimoneno) através de diferentes pontos de vista: Primeiro, estudamos as transições eletrônicas e estruturais sofridas por poucas camadas de antimoneno funcionalizadas por diferentes grupos químicos. Em segundo lugar, investigamos os mecanismos para emergência de bandas planas na estrutura de bandas eletrônicas de bicamadas de antimoneno giradas. Em seguida, também utilizamos dinâmica molecular livre de parâmetros empíricos para estudar os efeitos de baixa temperatura nos modos de vibração de uma monocamada de antimoneno. Por último, em colaboração com o laboratório de Nanoscopia da UFMG, estudamos as transições eletrônicas e estruturais sofridas por heteroestruturas de grafeno/nitreto de boro hexagonal ao serem pressionadas em experimentos de microscopia de força atômica. De forma geral, observamos diversas propriedades interessantes que ratificam o antimoneno como um nanomaterial promissor para aplicações tecnológicas e como plataforma para investigar propriedades físicas exóticas.

Palavras-chave: DFT. Antimoneno. Bandas flat. Grafeno.

Abstract

The search for new two-dimensional materials with properties suitable for technological applications is attracting growing interest among condensed matter physicists. It is very important to use theoretical methods to investigate the electronic and structural properties of these materials, given that they can present a series of exotic properties that are of great physical and chemical interest. One of the most successful theories in this area is the density functional theory, which allows the investigation of nanomaterials without the use of any empirical parameters and with excellent computational efficiency. In this thesis, we seek to use the density functional theory to study the two-dimensional version of antimony (antimonene) from several points of view: First, we studied the electronic and structural transitions undergone by few layers antimonene functionalized by different chemical groups. Second, we investigated the mechanisms for flat band emergence on the twisted antimonene bilayer electronic bandstructure. Then, we also used ab initio molecular dynamics to study the effects of low temperature on the vibration modes of the antimonene monolayer. Finally, in collaboration with the Nanoscopy laboratory at UFMG, we studied the electronic and structural transitions undergone by graphene/hexagonal boron nitride heterostructures compressed in atomic force microscopy experiments. In general, we observed several interesting properties that confirm antimonene as a promising nanomaterial for technological applications and as a platform to investigate exotic physical properties.

Keywords: DFT. Antimonene. Flat bands. Graphene.

Contents

Introduction

"If time was on my side, I'd still have none to waste"

Believe - Eminem

After almost 20 years since the synthesis of graphene [1], it is formidable how much we have learned about the physical properties of materials at the two-dimensional scale. Yet, there is an ever growing interest in the so called nanomaterials, not only in the discovery of novel compounds, but also in the modulation of their electronic, optical and structural properties through nanomanipulation. The reasoning behind this race is clear: the amount of new fundamental physical phenomena and technological applications provided by 2D materials is endless. Graphene, for instance, is promised to yield a wide range of applications such as ultra-sensitive chemical sensors, quantum dot devices, thin-film transistors, conductive films as well as biomedical and microelectronics applications [2–7]. Moreover, recent results showed again the capacity of graphene to surprise: Yuan Cao et. al. [8] reported the observation of unconventional superconductivity in a two-dimensional superlattice of twisted graphene bilayers. When the two sheets of graphene have a relative angle of approximately 1.1° (the first "magic" angle), flat bands emerge in the vicinity of the Fermi level in the electronic band structure, giving rise to correlated insulating states at half filling which can be tuned using electrostatic doping to zero-resistance states at 1.7 K. These correlated states are consistent with Mott-like insulator states, a consequence of electrons being localized in a superlattice generated by the moiré pattern [9]. The existence of such exotic properties in twisted graphene bilayers paves the way for the investigation of different kinds of 2D materials in similar situations. The van der Waals heterostructures - 2D materials obtained by the stacking of individual layers bonded by van der Waals forces - provide a never-ending playground to explore new physics [10, 11]. Exciton superlattices in twisted transition metal dichalcogenides [12, 13], topological polaritons and photonic superlattices in 2D twisted metal oxides [14], modulation of van der Waals potential in twisted hexagonal boron nitride (hBN) bilayers [15], and interlayer magnetism in the stacked 2D magnetic semiconductors [16] are only a few examples of how the moiré pattern in 2D materials can give rise to exotic and interesting physical phenomena. Part of this thesis is dedicated to extend the investigation of the flat band mechanism in novel 2D materials.

Alternatively, manipulation of the surface chemistry of 2D materials can also lead to interesting electronic and structural transitions. Adsorption of chemical groups on the top and/or bottom layers of 2D materials such as graphene and hBN few layers can favor the formation of 2D diamond-like structure under pressure [17, 18]. Moreover, chemical functionalization of graphene with fluorine (Fluorographene) [19], hydrogen (graphane) [20], and oxygen [21]

atoms can drastically change their electronic properties, becoming insulators that can be used in nanodevices [10]. On the other hand, Xihong Peng and Qun We [22] reported theoretical evidence of a different kind of structural and electronic modulation: Functionalization of phosphorene with OH, O, H, F, and Cl induced disruption of the covalent bonds, acting as a chemical scissor to cut phosphorene. The electronic structure of the final phosphorus nanochains ranges from insulator (fully hydrogenated case) to one-dimensional Dirac material (without any functionalization) in which the charge carriers are massless Fermions. In light of these results, we dedicated a major part of this thesis to investigate the electronic and structural transitions of 2D heterostructures under pressure and the chemical functionalization effects on novel 2D materials.

Furthermore, an important aspect of nanodevices development is to understand the temperature effects in their physical properties. Temperature-dependent Raman spectroscopy provides a crucial way of investigating the normal mode frequency of two-dimensional nanomaterial. Indeed, Damien Tristant et. al. [23] reported frequency downshifts to the Raman active modes of black phosphorus as well line width increases with increasing temperature. Tian Lan et. al. [24] performed similar measurements on rutile titanium dioxide (TiO_2) from 100 to 1150 K where they could discriminate the quasiharmonic effects of the thermal expansion from the anharmonic effects of the phonon-phonon interactions. From the theoretical point of view, one of the most successful ways of studying the temperature effects on the phonon modes is via the velocity autocorrelation function [23–26]. Using molecular dynamics, one can calculate the velocity of each timestep of the simulation, calculate the velocity autocorrelation function and obtain the phonon spectra through the Fourier transform. By combining theoretical and experimental methods, one can understand and hopefully manipulate the phonon scattering in 2D materials, which could result in better thermoelectric devices and improved heat dissipation on nanoscale transistors. As such, we will use this theoretical technique to investigate the low-temperature effects on the phonon bandstructure of novel 2D materials.

Finally, we can summarize the general objectives of this thesis in the following topics:

- Investigate the electronic and structural properties of promising 2D material antimonene through chemical functionalization;
- Study the flat band emergence mechanism in this new material and ways to tune the resulting flat bands;
- Explore the low-temperature effects on the phonon bandstructure of antimonene monolayer;
- And finally, investigate the electronic and structural transitions in two-dimensional heterostructures under pressure.

This thesis is organized as follows: In chapter 1 we discuss all the basic theoretical foundations for the investigation of the electronic and structural properties of 2D materials. In

chapter 2 we introduce the antimonene phases and properties, with a general description of bulk and two-dimensional structures. In chapter 3 we start investigating electronic and structural transitions induced by the chemical functionalization of antimonene few layers. In chapter 4 we investigate the flat band emergence on twisted antimonene bilayers. In chapter 5 we use molecular dynamics to study the low-temperature effects on the phonon bandstructure of antimonene monolayer. In chapter 6, the electronic and structural transition of compressed graphene/hexagonal boron nitride heterostructures are investigated. Finally, in chapter 7 we present our conclusions and future perspectives.

1 Electronic structure methods

"Time is never time at all
You can never ever leave
Without leaving a piece of youth"

Tonight, Tonight - The Smashing Pumpkins

In this chapter, we will discuss the theoretical methods to investigate the electronic and structural properties of 2D materials. We are interested in nanoscale systems, so a dive into the realm of quantum mechanics is necessary. Our descriptions start from the fundamental problem of the solid-state description: solving the Schroedinger equation for an interacting electron system.

1.1 The interacting electron problem

In a nutshell, the properties of atoms, molecules and solids can be investigated solving the Schroedinger equation for the electrons and nuclei, which defines a interacting quantum many-body problem:

$$\hat{\mathscr{H}}\Psi(\{\mathbf{r}_i\};\{\mathbf{R}_\alpha\}) = E\Psi, \tag{1.1}$$

where $\hat{\mathscr{H}}$ is the hamiltonian operator, Ψ is the wavefunction of all atomic and electronic coordinates represented by $\mathbf{R}_\alpha$ and $\mathbf{r}_i$ respectively. To solve the above equation, one needs to use several approximations. The first one is to consider the non-relativistic hamiltonian, composed of the sum of the kinetic energy and Coulomb interaction of the electrons and nuclei [27, 28]:

$$\begin{aligned}\hat{\mathscr{H}} &= -\frac{1}{2}\sum_{i=1}^{N}\nabla_i^2 - \frac{1}{2}\sum_{\alpha=1}^{M}\frac{1}{M_\alpha}\nabla_\alpha^2 + \frac{1}{2}\sum_{j\neq 1}^{N}\sum_{i=1}^{N}\frac{1}{|\mathbf{r}_i-\mathbf{r}_j|} \\ &+ \frac{1}{2}\sum_{\alpha\neq\beta}^{M}\sum_{\beta=1}^{M}\frac{Z_\alpha Z_\beta}{|\mathbf{R}_\alpha-\mathbf{R}_\beta|} - \sum_{i=1}^{N}\sum_{\alpha=1}^{M}\frac{Z_\alpha}{|\mathbf{r}_i-\mathbf{R}_\alpha|} \\ &= \hat{T}_e + \hat{T}_N + \hat{V}_{ee} + \hat{V}_{NN} + \hat{V}_{Ne}\end{aligned} \tag{1.2}$$

where $\hat{T}_e$ is the electron kinetic energy operator, $\hat{T}_N$ is the nucleus kinetic operator, M_α is the nuclear mass indexed by α at the position $\mathbf{R}_\alpha$, $\hat{V}_{ee}$ is the electron-electron repulsive potential operator, $\hat{V}_{NN}$ is the nuclei repulsive potential operator, and $\hat{V}_{Ne}$ is the attractive potential energy between electron and nucleus. The i and j indices refer to electrons and α and β to nuclei. Using atomic units, the electron mass, charge, and Planck constant are unitary.

A second step toward the simplification of the equation 1.2 is the Born-Oppenheimer approximation. It states that since the electron mass is almost two thousand times smaller than

that of the proton, they move much faster than the nuclei and therefore we can decouple the movement and fix the nuclei:

$$\hat{\mathscr{H}} = \hat{T}_e + \hat{V}_{ee} + \hat{V}_{Ne} + \hat{V}_{NN} = \hat{\mathscr{H}}_{ele} + \hat{V}_{NN}. \tag{1.3}$$

We can now solve separately the electron part of the hamiltonian, in which the resulting wavefunction will depend explicitly on the electron coordinates and parametrically on the nuclei coordinates:

$$\hat{\mathscr{H}}_{ele}\Phi_{ele}(\{\mathbf{r}_i\};\{\mathbf{R}_\alpha\}) = E_{ele}\Phi_{ele}(\{\mathbf{r}_i\};\{\mathbf{R}_\alpha\}). \tag{1.4}$$

The total energy of the system can be defined as [27]:

$$E_{total} = E_{ele} + \frac{1}{2}\sum_{\alpha\neq\beta}^{M}\sum_{\beta=1}^{M}\frac{Z_\alpha Z_\beta}{|\mathbf{R}_\alpha - \mathbf{R}_\beta|}, \tag{1.5}$$

where E_{ele} is the total electronic energy, which provides a potential to the nuclei movement.

Even with these approximations, obtaining the electron wavefunction is a complex problem. The main challenge comes from the repulsive interaction between the N electrons in the Schroedinger equation for molecules or solids. The first approach to this problem is through the independent particle approximation: Each electron moves independently in an effective potential which brings the effect of the remaining electrons. In this approximation, the problem of calculating the electron wavefunction Φ_{ele} for N electrons divides in searching for a set of solutions $\{\phi_i\}$ for N one-electron equations.

The electron wavefunction must also satisfy the symmetrization postulate, which states that the wavefunction of fermions (such as electrons) must obey the Fermi-Dirac distribution and be antisymmetric under coordinates exchange:

$$\Phi(\mathbf{x}_1,...,\mathbf{x}_i,...,\mathbf{x}_j,...,\mathbf{x}_N) = -\Phi(\mathbf{x}_1,...,\mathbf{x}_j,...,\mathbf{x}_i,...,\mathbf{x}_N). \tag{1.6}$$

One can construct the total electron wave function as a combination of Slater determinants which forms a complete base:

$$|\Phi\rangle = c_0|\Psi_0\rangle + \sum_{ra} c_a^r|\Psi_a^r\rangle + \sum_{\substack{a<b\\r<s}} c_{ab}^{rs}|\Psi_{ab}^{rs}\rangle + \ldots, \tag{1.7}$$

where $|\Psi_0\rangle$ is the ground state Slater determinant constructed from the set of N one electron states:

$$|\Psi_0\rangle = \frac{1}{\sqrt{N!}}\begin{vmatrix} \phi_i(\mathbf{x}_1) & \phi_j(\mathbf{x}_1) & \ldots & \phi_k(\mathbf{x}_1) \\ \phi_i(\mathbf{x}_2) & \phi_j(\mathbf{x}_2) & \ldots & \phi_k(\mathbf{x}_2) \\ \vdots & \vdots & & \vdots \\ \phi_i(\mathbf{x}_N) & \phi_j(\mathbf{x}_N) & \ldots & \phi_k(\mathbf{x}_N) \end{vmatrix}, \tag{1.8}$$

and $|\Psi_a^r\rangle$ is the excited determinant, in which the occupied orbital ϕ_a was replaced by the virtual orbital ϕ_r.

1.2 The Hartree-Fock method

If one truncates the infinite series 1.7 in the first term, only the ground state Slater determinant (equation 1.8) will be used to describe the electron wave function and to solve the Schroedinger equation. This is the essence of the Hartree-Fock (HF) method. Let us assume that each $\phi_i(\mathbf{x}_1)$ is a spin-orbital function, obtained by the product of an position function $\psi_i^\sigma(\mathbf{r}_j)$ and a spin variable function $\alpha_i(\sigma_j)$. For simplicity, let us consider a spin-independent hamiltonian, for which the total electronic energy is given by:

$$\begin{aligned}\langle\Phi|\hat{\mathscr{H}}|\Phi\rangle = &\sum_{i,\sigma}\int d^3r\,\psi_i^{\sigma*}(\mathbf{r})\left[-\frac{1}{2}\nabla^2 + v_{ext}(\mathbf{r})\right]\psi_i^\sigma(\mathbf{r}) + V_{NN} \\ &+\frac{1}{2}\sum_{i,j,\sigma_i\sigma_j}\int d^3r d^3r'\,\psi_i^{\sigma_i*}(\mathbf{r})\psi_j^{\sigma_j*}(\mathbf{r}')\frac{1}{|\mathbf{r}-\mathbf{r}'|}\psi_i^{\sigma_i}(\mathbf{r})\psi_j^{\sigma_j}(\mathbf{r}') \\ &-\frac{1}{2}\sum_{i,j,\sigma}\int d^3r d^3r'\,\psi_i^{\sigma*}(\mathbf{r})\psi_j^{\sigma*}(\mathbf{r}')\frac{1}{|\mathbf{r}-\mathbf{r}'|}\psi_j^{\sigma}(\mathbf{r})\psi_i^{\sigma}(\mathbf{r}')\end{aligned} \tag{1.9}$$

where the two first terms groups the one particle mean values which involve sums over all orbitals and the mean value of the potential energy of the nuclei (V_{NN}). The third and fourth terms are the "direct" and exchange interactions among the electrons, respectively, which are both double sums. We kept the $i = j$ terms because they cancel out in the direct and exchange sums, allowing us to obtain the electron density from summing over all orbitals. The minimization of the total energy with respect to the ψ_i orbitals, while keeping the orthogonality among them, leads to the Hartree-Fock equations:

$$\hat{\mathscr{H}}_{HF}^i\psi_i^\sigma(\mathbf{r}) = \left[-\frac{1}{2}\nabla^2 + V_{ext}(\mathbf{r}) + V_H(\mathbf{r}) + \hat{V}_x^{i,\sigma}(\mathbf{r})\right]\psi_i^\sigma(\mathbf{r}) = \varepsilon_i^\sigma\psi_i^\sigma(\mathbf{r}) \tag{1.10}$$

where $V_H(\mathbf{r})$ is the direct potential (or Hartree potential) and $V_{ext}(\mathbf{r})$ is the exchange potential which comes from the antisymmetrization of the wavefunctions, acting to keep electrons with the same spin apart. The direct potential is the average Coulomb repulsion between the electron described by ψ_i and the other electrons. Although this average potential allows the separation of the problem in N independent problems, the correlation effect in the electrons is lost since the exact Coulomb repulsion changes when the other electrons move. In order to include correlation effects in the electronic hamiltonian, one must go beyond the HF method, that is, include more terms of the series in 1.7, a method called Configuration Interaction (CI). However, the computational cost of CI increases fast, being limited to very simple systems.

1.3 The density functional theory

The density functional theory (DFT) is an ab initio formalism (free of empirical parameters) to the description of the ground state of matter. The main advantages of DFT over HF and CI is the relatively low computational cost even for big systems and the inclusion of correlation

effects. The fundamental idea of DFT is that the properties of a many-body interacting system can be described as a functional of the electron ground state density n_0. The theory was proposed by Pierre Hohenberg, Walter Kohn, and Lu Jeu Sham [29, 30] and is based on the Hohenberg-Kohn theorems and the Kohn-Sham equations, that we shall describe in the next subsections.

1.3.1 The Hohenberg-Kohn theorem

The two theorems demonstrated by Hohenberg and Kohn can be stated as [29]:

Theorem 1.3.1. *For any interacting particle system in an external field $V_{ext}(\mathbf{r})$, the potential $V_{ext}(\mathbf{r})$ is solely defined by the density of the ground state $n_0(\mathbf{r})$, excepted by a additive constant.*

Theorem 1.3.2. *One can define an energy functional $E[n]$ in terms of the density $n(\mathbf{r})$, valid for any external potential $V_{ext}(\mathbf{r})$. For a specific $V_{ext}(\mathbf{r})$, the exact ground state energy is an global minimum of $E[n]$, and the ground state density $n_0(\mathbf{r})$ minimizes this functional.*

The proof of these theorems can be found extensively in literature [29, 31–33], therefore we will focus only on the main consequences. We can summarize the physical implications of these theorems in three important points [31]:

1. The ground state wavefunction is a unique functional of the ground state electron density.

$$\Psi_0(\mathbf{r}_1, \mathbf{r}_2, \ldots, \mathbf{r}_N) = \Psi_0([n_0(\mathbf{r})]). \tag{1.11}$$

   As a consequence, the expected value of the ground state over any observable $\hat{O}$ is a functional of $n_0(\mathbf{r})$,

$$O_0 = O[n_0] = \langle \Psi[n_0] | \hat{O} | \Psi[n_0] \rangle . \tag{1.12}$$

2. The ground state energy E_0,

$$E_0 = E[n_0] = \langle \Psi[n_0] | \hat{\mathscr{H}} | \Psi[n_0] \rangle , \tag{1.13}$$

   has the variational property

$$E[n_0] \leq E[n'], \tag{1.14}$$

   where n_0 is the ground state density, n' is any other density, $\hat{\mathscr{H}} = \hat{T} + \hat{V}_{ee} + \hat{V}$ is the hamiltonian, $\hat{T}$ is the kinetic energy, $\hat{V}_{ee}$ is the interaction energy between the electrons and $\hat{V}$ is the potential energy of the external field due to the positively charged nuclei. Therefore, the ground state electron density minimizes the total energy of the many-body system.

3. The kinetic energy and interaction energy of a non-relativistic Coulomb system are described using universal operators, and $E[n]$ can be written as

$$E[n] = T[n] + V_{ee}[n] + V[n] = F[n] + V[n], \tag{1.15}$$

where $F[n]$ is a universal operator of the type 1.12 and independent of the external potential. However, this potential energy due to an external potential $v_{ext}(\mathbf{r})$ can be written explicitly as

$$V[n] = \int n(\mathbf{r}) v_{ext}(\mathbf{r}) d^3r \tag{1.16}$$

is non-universal, that is, it depends on the system to be studied. Therefore, once the system is specified, the functional $V[n]$ is known.

Despite a great theoretical advance, the theorems of Hohenberg and Kohn do not provide a systematic method for solving the many-body problem. We must then look into the formalism derived by Kohn and Sham [30]: The single-body auxiliary system.

1.3.2 The Kohn-Sham equations

The Kohn-Sham (KS) equations [30] map into the problem of many interacting electrons to a problem of non-interacting electrons moving in an effective potential due to all the other electrons. First, we rewrite the electronic density as

$$n(\mathbf{r}) = \sum_{\sigma} n(\mathbf{r}, \sigma) = \sum_{\sigma} \sum_{i=1}^{N^\sigma} |\psi_i^\sigma(\mathbf{r})|^2, \tag{1.17}$$

the kinetic energy of the non-interacting system as

$$T_s = -\frac{1}{2} \sum_{\sigma} \sum_{i=1}^{N^\sigma} \langle \psi_i^\sigma | \nabla^2 | \psi_i^\sigma \rangle = \frac{1}{2} \sum_{\sigma} \sum_{i=1}^{N^\sigma} \int d^3r |\nabla \psi_i^\sigma(\mathbf{r})|^2, \tag{1.18}$$

and the Coulomb energy associated with the electron density $n(\mathbf{r})$ as

$$E_H[n] = \frac{1}{2} \int d^3r d^3r' \frac{n(\mathbf{r}) n(\mathbf{r}')}{|\mathbf{r} - \mathbf{r}'|}. \tag{1.19}$$

KS's approach to the interacting system is to rewrite the total energy functional of the system in the form:

$$E_{KS} = T_s[n] + \int d^3r V_{ext}(\mathbf{r}) n(\mathbf{r}) + E_H[n] + E_{NN} + E_{xc}[n], \tag{1.20}$$

where all the correlation and exchange effects are grouped under the term $E_{xc}[n]$:

$$E_{xc}[n] = T_c[n] + V_c[n] + V_x[n], \tag{1.21}$$

where $T_c[n]$ is the contribution to the kinetic energy of the correlated system, $V_c[n]$ and $V_x[n]$ is the electronic correlation potential and exchange interaction, respectively.

By minimizing the equation 1.20 with respect to density $n(\mathbf{r}, \sigma)$, one can obtain the solution for the KS auxiliary system for the ground state. However, T_s is expressed explicitly as an orbital functional, and all other terms are considered density functionals, so we must use the chain rule to derive the variational equation:

$$\frac{\delta E_{KS}}{\delta \psi_i^{\sigma *}(\mathbf{r})} = \frac{\delta T_s}{\delta \psi_i^{\sigma *}(\mathbf{r})} + \left[\frac{\delta E_{ext}}{\delta n(\mathbf{r}, \sigma)} + \frac{\delta E_H}{\delta n(\mathbf{r}, \sigma)} + \frac{\delta E_{xc}}{\delta n(\mathbf{r}, \sigma)} \right] \frac{\delta n(\mathbf{r}, \sigma)}{\delta \psi_i^{\sigma *}(\mathbf{r})} = 0 \tag{1.22}$$

subject to the condition of orthonormality

$$\langle \psi_i^\sigma | \psi_j^{\sigma'} \rangle = \delta_{i,j}\delta_{\sigma,\sigma'}. \tag{1.23}$$

The minimization process leads to the effective hamiltonian:

$$\hat{\mathscr{H}}_{KS}^\sigma(\mathbf{r}) = -\frac{1}{2}\nabla^2 + V_{KS}^\sigma(\mathbf{r}), \tag{1.24}$$

with

$$\begin{aligned} V_{KS}^\sigma &= V_{ext}(\mathbf{r}) + \frac{\delta E_H}{\delta n(\mathbf{r},\sigma)} + \frac{\delta E_{xc}}{\delta n(\mathbf{r},\sigma)} \\ &= V_{ext}(\mathbf{r}) + V_H(\mathbf{r}) + V_{xc}^\sigma. \end{aligned} \tag{1.25}$$

Once the independent particle equations are obtained, the potential must be calculated self-consistently with the resulting density. If it were possible to know the exact exchange and correlation functional, then the hamiltonian 1.24 would lead to the exact ground state energy and density. Fig. 1.1 illustrates the cycle for calculating physical observables in the KS formalism.

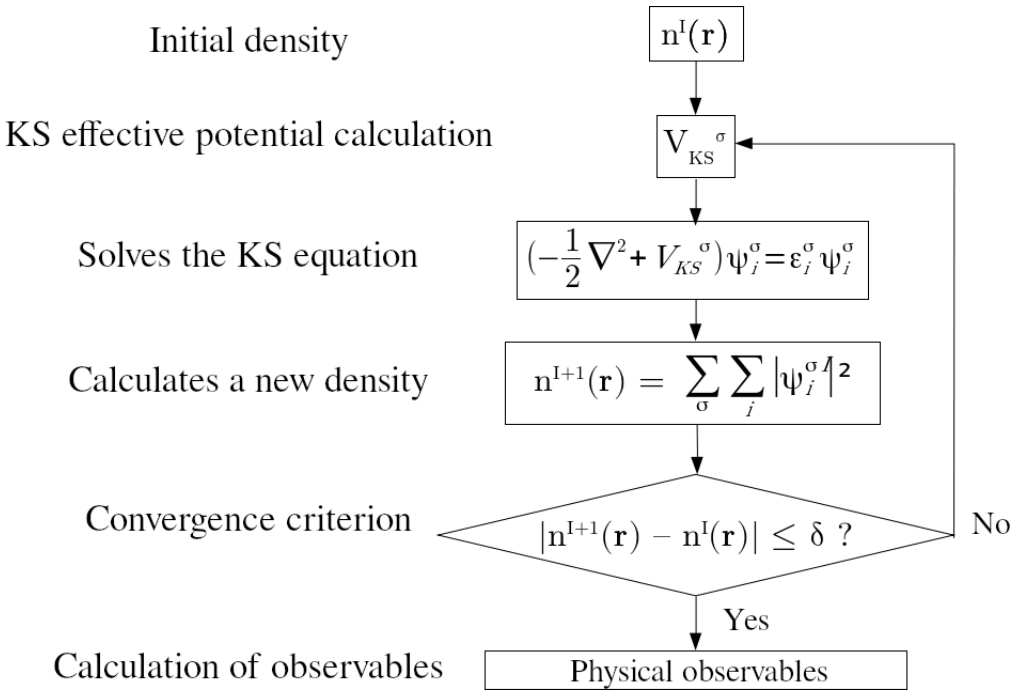

Figure 1.1 – DFT self-consistent cycle

However, an explicit expression for the $E_{xc}[n]$ is unknown. To be able to apply all the formalism developed, one must assume new approximations to the exchange-correlation functional: The local density approximation (LDA).

1.3.3 Approximations in the DFT

In their original work, Kohn and Sham argued that in certain cases a metal could be approximately treated as a homogeneous ideal gas. In this limit, it is known that the exchange

and correlation energy has a local character and therefore they proposed that the exchange and correlation energy density $\varepsilon_{xc}([n],\mathbf{r})$ is the same as that in a homogeneous electron gas with the same density at a point $\mathbf{r}$. Then $E_{xc}[n]$ can be written as

$$E_{xc}^{LDA}[n] = \int d^3 r n(\mathbf{r}) \varepsilon_{xc}^{hom}(n(\mathbf{r})). \tag{1.26}$$

This approximation is known as the local density approximation (LDA) and is one of the most common approaches to treat the exchange-correlation functional since $\varepsilon_{xc}^{hom}(n(\mathbf{r}))$ can be obtained by numerical methods such as Monte Carlo [34]. There is also an approach to improve the results obtained by the LDA in certain systems. In the generalized gradient approximation (GGA) it is proposed to modify the behavior of the functions including the dependence on the density gradient, leading to:

$$E_{xc}^{GGA}[n] = \int d^3 r n(\mathbf{r}) \varepsilon_{xc}(n(\mathbf{r}), |\nabla n(\mathbf{r})|). \tag{1.27}$$

One of the most used approaches nowadays and which obtains excellent results is the functional GGA-PBE, proposed by Perdew, Burk, and Enzenholf in 1996 [35].

1.4 Molecular dynamics

In one of the projects of this thesis, we also performed ab initio molecular dynamics (AIMD) calculations. Via numerical solutions to Newton's equation of motion, one can use molecular dynamics to simulate the temporal evolution of a system. The equation of motion for a set of nuclei treated as classical masses are

$$M_I \ddot{\mathbf{R}}_I = -\frac{\partial E}{\partial \mathbf{R}_I} = \mathbf{F}_I[\{\mathbf{R}_J\}], \tag{1.28}$$

where $E[\{R_J\}]$ are the interacting energy depending of the particle positions $\{R_J\}$. Several different algorithms can be used to solve the discretized equation with discrete time steps, such as the Verlet algorithm [36]. At each time step t, the idea is to update the atomic position of each nucleus to the next time step t + Δt depending on the forces acting on it at the present time step (see the derivation on Appendix A):

$$R_I(t+\Delta t) = 2R_I(t) - R_I(t-\Delta t) + \frac{(\Delta t)^2}{M_I} F_I[\{R_J\}]. \tag{1.29}$$

Classical molecular dynamics uses predefined (usually empirical) potentials to describe the interatomic interaction. However, molecular dynamics simulations with forces derived directly from the DFT formalism are possible thanks to advances in electronic structure calculations.

MD calculations are usually performed in a closed system in a microcanonical ensemble, where the energy (E), number of particles (N), and volume (V) are kept fixed (NVE). However,

we will be using a different ensemble for the calculations in this thesis: Using the canonical ensemble, one can use the Nosé thermostat [37] to control the temperature over the simulation time steps.

1.5 Pseudopotentials

After the development of the HK theorems, the KS equations, and the appropriate approximations for the exchange and correlation functional, we can finally carry out the electronic structure calculations in a systematic way. However, the high computational cost for large systems is still a challenge that must be addressed. In the pseudopotential approximation, the strong Coulomb potential of the nuclei and the effects of the electrons strongly bounded to the nucleus are replaced by an effective ionic potential acting on the valence electrons. The justification for this approximation is that the electrons close to the nucleus are so strongly bound to it that they do not effectively participate in chemical bonds. In this way, the electronic structure calculations become simpler and more efficient.

1.5.1 Norm-conserving pseudopotentials

The concept of the norm-conserving pseudopotentials was established by Hamann, Schlüter and Chiang [38] to define a category of pseudopotentials with a list of desirable properties:

1. Real eigenvalues and pseudo eigenvalues must be equal for a given atomic configuration;
2. The real wave function and the pseudo wave function (PP) must be the same for $r > r_c$, with r_c being the cutoff radius that separates the nucleus from the valence electrons:

$$\psi^{PP}(\mathbf{r}) = \psi^{real}(\mathbf{r}) \qquad r > r_c; \tag{1.30}$$

3. the integrals from 0 to r of the charge density and the pseudo charge density must be equal for $r > r_c$ for each valence state:

$$\int_0^r |\psi^{PP}(\mathbf{r})|^2 dr = \int_0^r |\psi^{real}(\mathbf{r})|^2 dr \qquad r > r_c; \tag{1.31}$$

4. the logarithmic derivatives of the real wave function and the pseudo wavefunction and their respective first derivatives must be equal for $r > r_c$.

Such properties are crucial to ensure good transferability of the pseudopotential to a variety of chemical environments. Fig. 1.2 illustrates property 2 for the pseudo-wave function, and also shows an example of a pseudopotential and its comparison with the Coulomb potential.

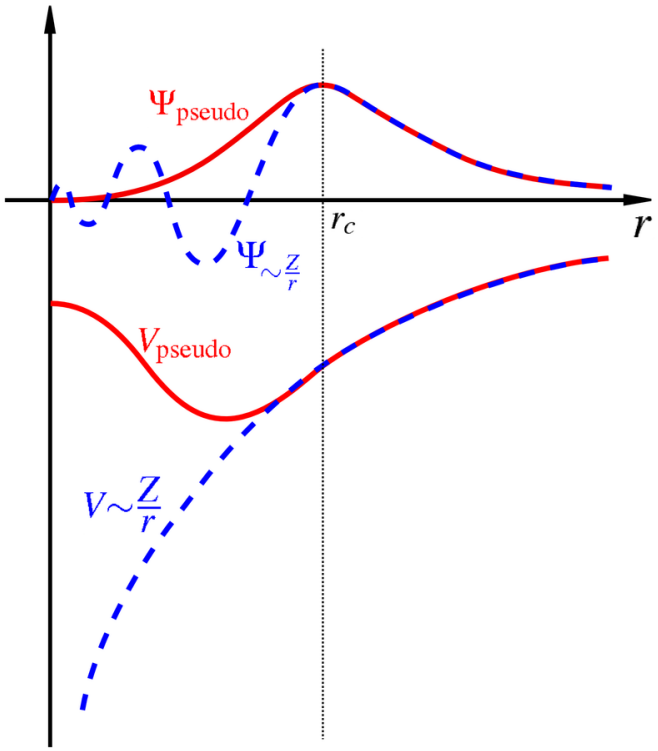

Figure 1.2 – Comparison between the wave function and the real Coulomb potential with the pseudo wavefunction and the pseudopotential.

1.6 Implementation

Once the fundamental theoretical formalism was established, we need to address the different ways one can numerically implement it. In this thesis, we used two of the most common ways to apply DFT methods: The Linear Combination of Atomic Orbitals (LCAO) and the plane waves (PW) method.

1.6.1 The LCAO method

In the LCAO formulation, the basis functions used to solve the HK equations are defined as atomic or atomic-like functions. As such, this basis provides a physical motivated description of the electronic states in materials. The LCAO code that we will use in this thesis is the SIESTA (Spanish Initiative for Electronic Simulations With a Thousand of Atoms) [39]. In the LCAO method, which in employed in the SIESTA code, the calculations of molecular properties are done by expressing the KS orbitals as a linear combination of atom-centered basis functions:

$$\psi_i(\mathbf{r}) = \sum_{\nu=1}^{\kappa} C_{\nu i}\phi_\nu. \tag{1.32}$$

Among the possible functional forms for the basis functions ϕ_ν, the most commonly used are Slater-type orbitals, Gaussian functions, and numerical basis functions. Therefore, using

the expansion 1.32 in the KS equations we have

$$\begin{aligned} \hat{\mathscr{H}}\psi_i(\mathbf{r}) &= E_i\psi_i(\mathbf{r}) \\ \sum_\mu C_{\mu i}\hat{\mathscr{H}}\phi_\mu(\mathbf{r}) &= E_i\sum_\mu C_{\mu i}\phi_\mu . \end{aligned} \tag{1.33}$$

If we multiply by ϕ_ν^* and integrate it over the entire space, we can rewrite the equation 1.33 as

$$\sum_\mu \left[\int d^3r\phi_\nu^*(\mathbf{r})\hat{\mathscr{H}}\phi_\mu(\mathbf{r}) - E_i\int d^3r\phi_\nu^*(\mathbf{r})\phi_\mu(\mathbf{r})\right] C_{\mu i} = 0 \tag{1.34}$$

and we can write the this equation in matrix form:

$$\sum_\mu \left(\mathscr{H}_{\nu\mu} - E_i S_{\nu\mu}\right) C_{\mu i} = 0, \tag{1.35}$$

where we define the elements of the overlap matrix as

$$S_{\nu\mu} = \langle\phi_\nu|\phi_\mu\rangle = \int d^3r\phi_\nu^*(\mathbf{r})\phi\mu(\mathbf{r}), \tag{1.36}$$

and $\mathscr{H}_{\nu\mu}$ as the matrix elements of the KS hamiltonian given by 1.24 calculated on the basis 1.32

$$\mathscr{H}_{\nu\mu} = \langle\phi_\nu|\mathscr{H}_{\nu\mu}|\phi_\mu\rangle = \int d^3r\phi_\nu^*(\mathbf{r})\hat{\mathscr{H}}\phi_\mu(\mathbf{r}). \tag{1.37}$$

The procedure proceeds through matrix diagonalization, leading to eigenvalues and eigenvectors, from which a new density is obtained. This new density defines another hamiltonian, where new matrices are calculated, and the cycle continues in a self-consistent way until convergence is obtained. One of the main advantages of the LCAO method over PW is the relatively low computational cost even for big systems, favoring the investigation of supercell systems, defects, and twisted systems without the need for large superclusters.

1.6.2 The plane wave method

Another approach to spawn the KS wavefunctions is using the PW method. The Bloch theorem [40] states that the wavefunction of an electron in a periodic potential can be written as

$$\psi_{i,k}(\mathbf{r}) = u_i(r)e^{ik\cdot r}, \tag{1.38}$$

where $u_j(r)$ has the same periodicity of the crystal, $e^{ik\cdot r}$ is a wave-like function, i indicates the band index, and k is a continuous wavevector that lives in the first Brillouin zone. We can express $u_j(r)$ in terms of discrete plane wave set with reciprocal lattice vectors G:

$$u_i(r) = \sum_G c_{i,G}e^{iG\cdot r}, \tag{1.39}$$

where $G \cdot R = 2\pi m$, m is an integer, R are the crystal lattice vectors and $c_{i,G}$ are the plane wave coefficients. Finally, combining equations 1.39 and 1.38, we obtain the linear combination of plane waves which will form the basis set to KS wavefunctions:

$$\psi_{i,k}(\mathbf{r}) = \sum_G c_{i,k+G} e^{i(k+G)\cdot r}. \tag{1.40}$$

Similar to the LCAO, calculation of the hamiltonian using 1.40 for the wavefunctions will lead to matrix equations that can be solved self-consistently until convergence (see Fig. 1.1). The numerical implementations of the PW method are abundant, we will use the VASP (Vienna Ab initio Simulation Package) code [41]. A few of the advantages of the PW method over the LCAO is the simplicity in the basis definition, where one can define a basis set that is independent of the type of crystal and treat all the space equally. PW also offers extremely efficient Ab initio molecular dynamics algorithms [42].

Once all the basic theoretical foundations have been laid, we start the investigation of the electronic and structural properties of novel two-dimensional nanomaterials. Before entering the main results of this thesis, we will introduce the system of interest in the next chapter: The antimony-based nanomaterials.

2 Antimony (Sb)

"Sem estresse, trabalho só me engrandece
Que nem Super Mario, depois do cogumelo"

Linhas de soco - Rincon Sapiência

A major part of this work is dedicated to the study of the electronic and structural properties of antimony (Sb) based nanomaterials. As such, a general introduction to Sb properties and different phases is necessary. In this chapter we will discuss the different Sb phases, and the two-dimensional Sb counterpart - Antimonene - and its properties.

The group 5A (group VA or V or 15) of the periodic table contains the pnictogens - nitrogen (N), phosphorus (P), arsenic (As), antimony (Sb), and bismuth (Bi). The name "pnictogens" is derived from the greek word *pnigein*, which means "choke" or "stifle" - common effects of beading pure Nitrogen gas [43]. They all have five electrons on their highest-energy orbitals, that is 2 electrons in the s subshell and 3 unpaired electrons in the p subshell (ns^2np^3). They also compose multiple one-element layered structures that represent great interest among solid state physicists. Among them, antimony (and its sub-structures) has been drawing increasing attention due to its interesting properties and advantages to others. Sb present interesting electronic properties regarding application on novel 2D electronics such as layer-dependent semi-metal to semiconductor and topological transitions [44–48], high carrier mobility [49], and strain-tunable indirect-to-direct band gap and topological transitions [44, 45, 50]. Additionally, applications on sustainable energy and catalysis are also receiving a lot of attention recently, where Sb may be included as an anode material in next-generation Li- and Ni-o batteries [51–53] or play an important roll in electro-catalysis [54, 55], photovoltaics [56], supercapacitors [57], and thermoelectrics [58]. First, let us start with the general properties of the thick or three-dimensional (3D) (Bulk) form of antimony.

2.1 Bulk antimony

Similar to the other members of the VA group, Sb has several different allotropes: one stable form called grey Sb (or β-Sb) and three metastable forms, which are explosive, black, and yellow. All the Sb structures used in this work are derived from β-Sb, therefore we will discuss only the properties of this structure and its 2D counterpart in this chapter.

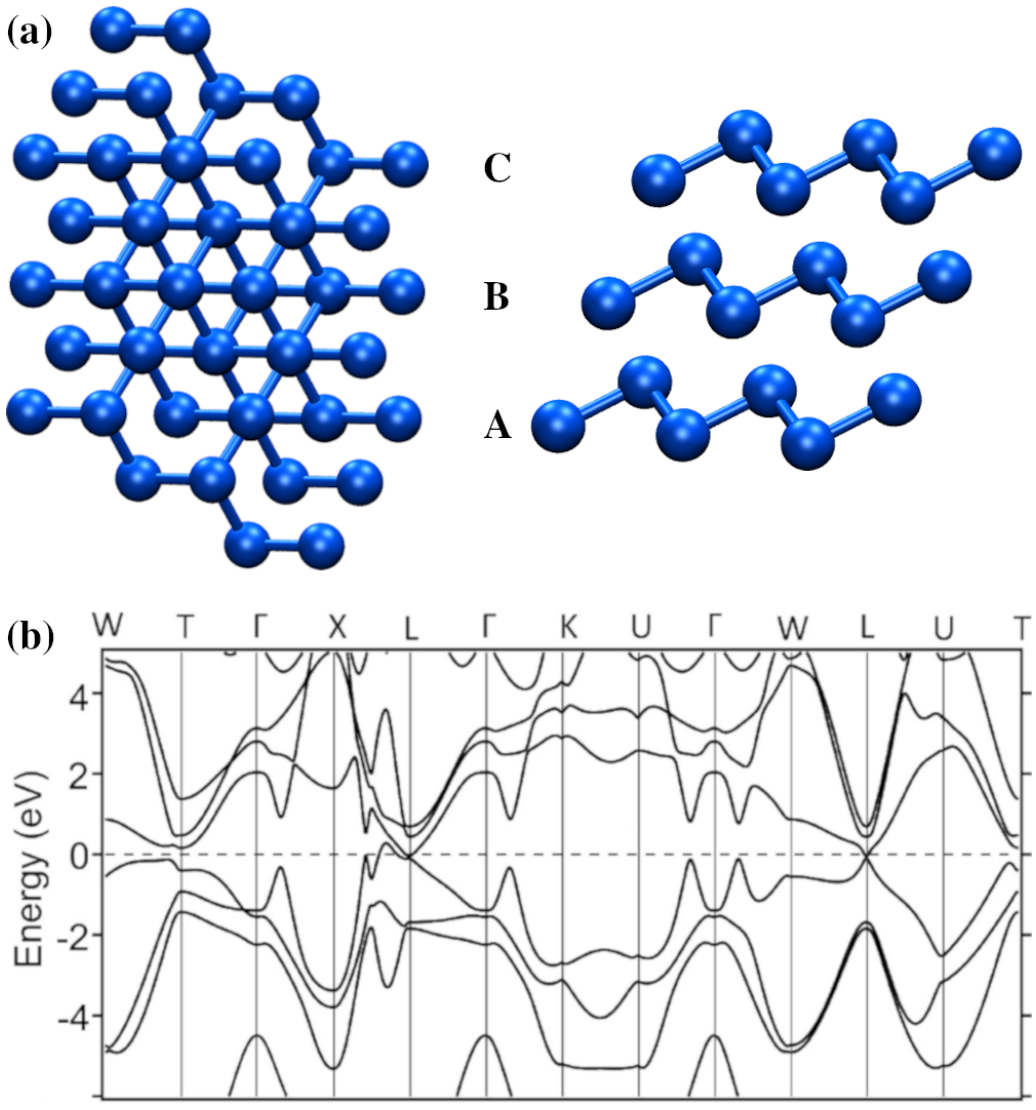

Figure 2.1 – β-phase bulk antimony. (a) Top and side view of the ABC stacked bulk antimony. (b) Electronic bandstructure of bulk Sb with SOC [59]. Blue spheres represent Sb atoms. The Fermi level is set to zero.

At ambient conditions, the most stable form of Sb crystallizes in a rhombohedral A7 structure with space group $R\bar{3}m$ [60]. The A7 structure can be regarded as a diagonally distorted fcc NaCl structure. The crystal can also be viewed as hexagonal atomic layers with an ABC stacking along the (111) direction as shown in Fig.2.1-(a). In each of the layers, the Sb atoms form three equidistant covalent bonds where the calculated atomic distance (at the DFT GGA-PBE level) is 2.90 and the angle between bonds is 95.70°. The interlayer distance (d_i) is 2.27 and the distance between the top and bottom atom inside a monolayer is 1.53 . The lattice parameter calculated to bulk Sb is 4.38 . Each of the ABC layers is called an antimonene monolayer. Also, the bulk has been described as a pseudolayered structure [61] due to a relatively large binding energy derived from the interaction of lone pair orbitals in adjacent layers [45].

Antimony is known to have a considerable spin orbit coupling (SOC) (only losing

to Bismuth in the group). It is also predicted to be a topological semimetal (TS) [48, 62], which means that the valence bands of the Sb bulk (Fig.2.1-(b)) are topologically non trivial. Moreover, G. Bian et. al. [46] experimentally observed helical surface bands in an Sb film (≈ 79) using angle-resolved photoemission spectroscopy (ARPES) . Interestingly, different topological transitions are predicted to take place in Sb narrower films as shown in Fig. 2.2, which is a motivation to investigate the nanostructures as we shall discuss in the next sections.

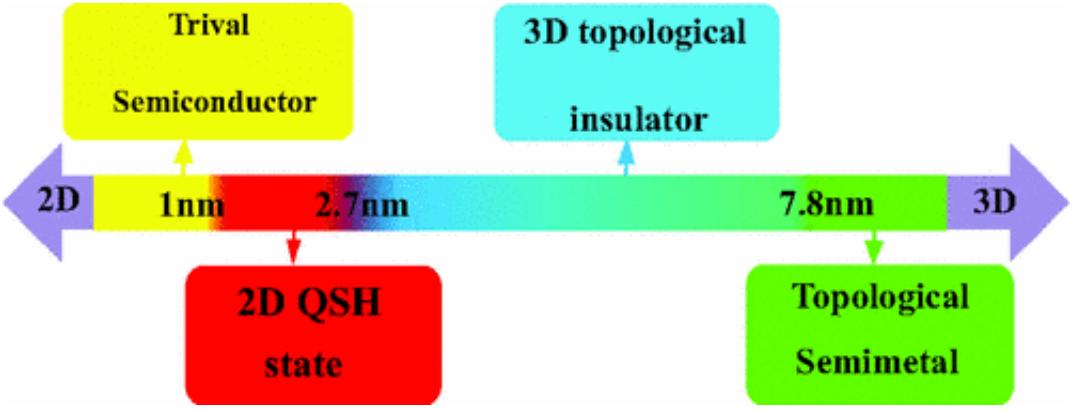

Figure 2.2 – Diagram showing the different topological phases of Sb as a function of the thickness, ranging from trivial semiconductor to topological semimetal. Figure obtained from [48].

2.2 Two dimensional antimony

Decreasing the thickness of Sb film reveals several interesting electronic transitions as shown in Fig. 2.2. Theoretical results show that around 7.8 nm (or 22 antimonene layers) a transition from the TS to a topological insulator phase (TI) happens. Furthermore, a quantum spin Hall (QSH) phase emerges at 2.7 nm (8 antimonene layers) followed by a topologically trivial semiconductor phase under 1.0 nm (3 antimonene layers) [48]. Several experimental techniques [63] - micromechanical exfoliation [64], van der Waals epitaxy [65], liquid-phase exfoliation [66, 67], molecular beam epitaxy [64], electromechanical exfoliation [64] are examples - may provide high quality few-layer antimonene samples where these properties can be investigated. Sung Hwan Kim et. al. [47] performed scanning tunneling microscopy/spectroscopy (STM/STS) in ultrathin Sb film grown on Bi_2Te_2Se by a thermal effusion cell at room temperature. The authors identified the trivial to QSH transition (3 to 4 layers), and they observed robust edge electronic states for the 4 and 5 layers in contrast with the 3 layer films. Although trivial topologically, the structures of the extreme left of the diagram on Fig.2.2 present quite remarkable properties and it will inevitably end on the thinnest possible Sb film: The antimonene monolayer which we will discuss in the next section.

2.3 The antimonene monolayer

The thinnest Sb film possible - the antimonene monolayer - is predicted to be a buckled hexagonal structure [44, 45] as one can see in Fig. 2.3-(a). It has a lattice parameter of 4.10 , a distance between the top and bottom atoms of 1.66 , and it is a trivial indirect semiconductor as shown in the electronic bandstructure in Fig.2.3-(b). However, several ways of tuning the electronic structure of antimonene were reported in the literature.

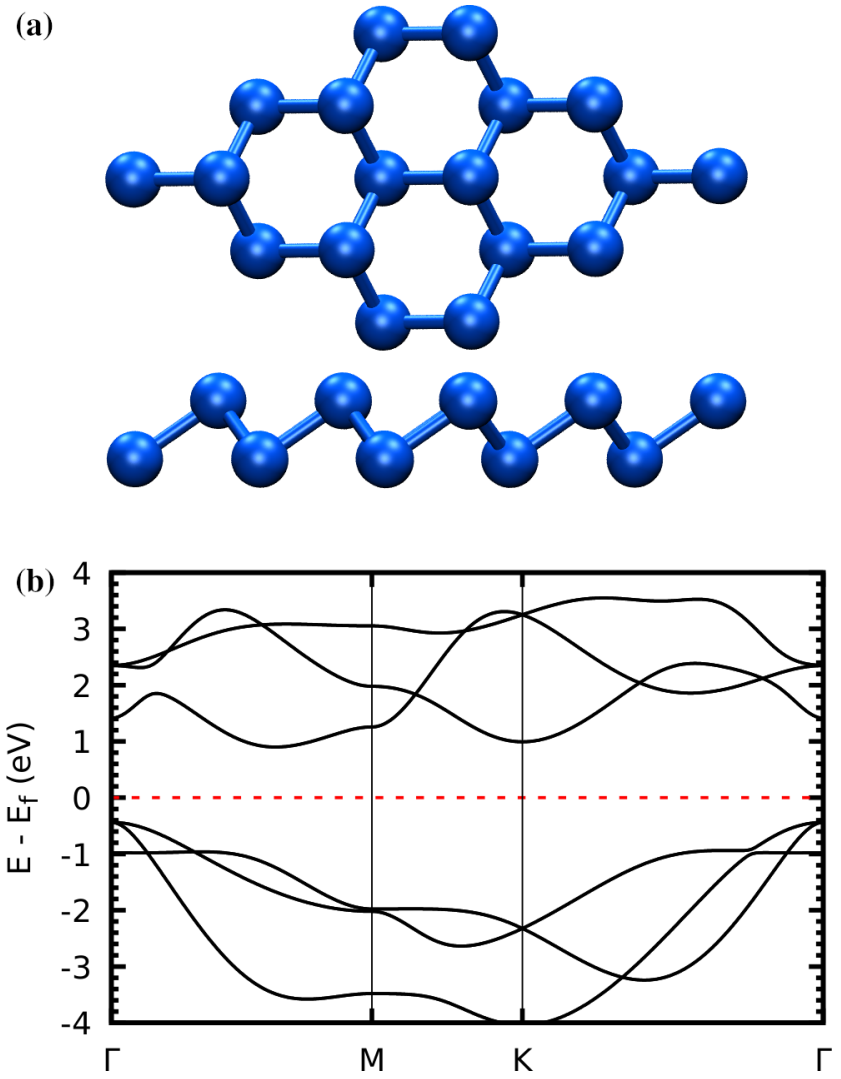

Figure 2.3 – The antimonene monolayer. (a) Top and side view of the antimonene monolayer. (b) Calcukated electronic bandstructure of antimonene at the DFT-GGA level. The Fermi level is set to zero.

D.M. Hoat et. al. [68] presented theoretical evidences of electronic modulation of the bandgap using strain. They reported an indirect to direct band gap transition with 4% tensile strain within the dynamical stability range observed in the phonon spectra. The reported strain also enhanced the optical absorption in a wide energy range (from infrared to ultraviolet) as well the thermoelectric properties, showing great versatility of antimonene for technological applications. Furthermore, Mingwen Zhao et. al. [50] reported strain-driven band inversion in

atimonene monolayers . The aplication of a biaxial tensile strain of 14.5% was sufficient to reduce the buckling height of the lattice, modifying the hybridization of the p_x, p_y, and p_z, and leading to a topological insulator phase [50]. On the other hand, electronic structure modulation on antimonene monolayer can be achieved by methods other than strain, such as chemical oxidation. Indeed, Shengli Zhang et. al. [69] reported theoretical calculations where several antimonene oxides - antimonene supercells with different concentrations of adsorbed oxygen - were investigated. These structures are predicted to have a direct band gap, covering the range of 0 to 2.28 eV and high carrier mobility. Moreover, the fully oxidized antimonene is expected to be a 2D topological insulator with a global bandgap of 0.177 eV, with a nontrivial Z_2 topological invariant in the bulk and topological edge states.

Although antimonene can be directly exfoliated from few layers [70], the relatively stronger interlayer interaction [44] makes the process slightly more difficult when compared to graphene and other 2D materials. However, several routes to manipulate and synthesize high-quality antimonene monolayers are being reported. Xu Wu et. al. [71] synthesized antimonene monolayer on 2D transition-metal-dichalcogenide $PdTe_2$ by molecular beam epitaxy. Using similar techniques, Tianchao Niu et. al. [72] reported the synthesis of antimonene on dielectric copper oxide. These results are important steps to the integration of novel two-dimensional nanomaterials with current semiconductor technologies. Additionally, Yan Shao et. al. [73] reported epitaxial growth of flat antimonene monolayer on Ag(111) substrate, while Shuo Sun et. al. [74] went in the opposite direction, reporting the synthesis of an antimonene monolayer with a three-heights-buckling configuration overlaid on $SbAg_2$ surface alloy-covered Ag(111).

Altogether, antimonene few- and monolayer are promising candidates for several technological applications as well as an excellent playground to explore fundamental physics. In the next three chapters, we will explore some of these interesting properties from different points of view: Chemical functionalization of the few layers with different agents, electronic band structure modulation induced by rotation of bilayers, and low-temperature effects on the phonon bandstructure of monolayers.

3 Oxidation driven structural transitions in few-layer antimonene

"Essa é a verdade, criança
aprende cedo a ter caráter
A distinguir sua classe, estude Marx
Seja um Mártir, às vezes um Luther King, um Sabotage"

Canão foi tão bom - Sabotage

3.1 Introduction

In this chapter, we shall investigate the possibility of formation of ordered Sb nanoribbons upon chemical functionalization.

The ordered transition from two- to one-dimensional (1D) structures – a restructuring which makes layers evolve into ribbons – is a cornerstone to the observation of physical phenomena and a challenge in the manipulation of matter at nanoscale. Half-metallicity in carbon ribbons induced by transverse in-plane electric fields, for instance, is associated exclusively to zig-zag edges [75]. As a consequence, protocols have been reported for a controlled synthesis of carbon ribbons, focusing on chemical routes within a bottom-up strategy [76, 77]. Edge geometry also plays a crucial role in ribbons built from other nanostructures. Depending on the crystallographic orientation of edges, antimonene nanoribbons may have magnetic ground states [61], and passivated ribbons may be direct or indirect band gap semiconductors [78]. Indeed, antimony two-dimensional (2D) structures [79, 80] have been attracting attention due to their topological insulator behavior under strain [81], the topological semi-metallicity of their few-layer counterpart, which, depending on the thickness, changes into a topological insulator state [48], and due to their potential applications in optoelectronic devices [64, 79, 82–84]. The present work concerns this material: We report calculations which show that oxidation of few-layer antimonene may lead to an atomic restructuring with formation of ordered multilayer zig-zag nanoribbons. The widths are uniquely determined by the number of layers of the initial structure, allowing the synthesis of ultranarrow ribbons and chains. These results definitely put antimony in a central position within the 2D research scenario and draw attention to its 1D ribbon counterparts. However, the rich phenomenology that has been predicted for such ribbons,

including existence of distinct magnetic phases and modulation of electronic behavior, requires precisely ordered edges in order to be experimentally detected.

3.2 Objectives

This brings the objectives of this chapter: we will focus on the description of a mechanism which emerges in a first principles approach when antimonene layers are completely functionalized with oxidizing agents, such as fluorine atoms or OH radicals. Briefly, we can summarize our goals in the following topics:

- We will study the chemical functionalization effect on antimonene from one to eight layers;
- We will also investigate the effects of semi-functionalization (chemical groups adsorbed only on the top layer);
- We will verify the replicability of this mechanism to other two-dimensional nanomaterials.

3.3 Computational details

We employed the SIESTA [39] implementation of the pseudopotential spin density functional theory, expanding the Kohn-Sham eigenfunctions in a finite range double-ζ basis set augmented by polarization functions (DZP basis set). To make sure we correctly described the pseudolayered character of the antimonene stacking, we compared three distinct approaches for the exchange-correlation functional: Local Density Approximation (LDA) with the Ceperley-Alder parametrization [34], Gradient Generalized Approximation (GGA) within the Perdew-Burke-Ernzerhof (PBE) parametrization [35], and a van der Waals density functional approach [85]. The results were basically the same, and the results presented in our work are all related to the GGA-PBE approach.The overall restructuring process and electronic modulation were similar for all different exchange-correlation approximations tested, with small differences only on the geometrical aspects such as lattice parameter and stacking distance (all within a 5% difference approximately). As such, the results presented in our work are all related to the GGA-PBE approach. A mesh cutoff of 400 Ry defined the grid for real space integrations, and the geometries were considered relaxed when the maximum force component in any atom was less then 10 meV/Å . To sample the Brillouin zone, we defined a k-grid cutoff of 120 Å in all calculations.

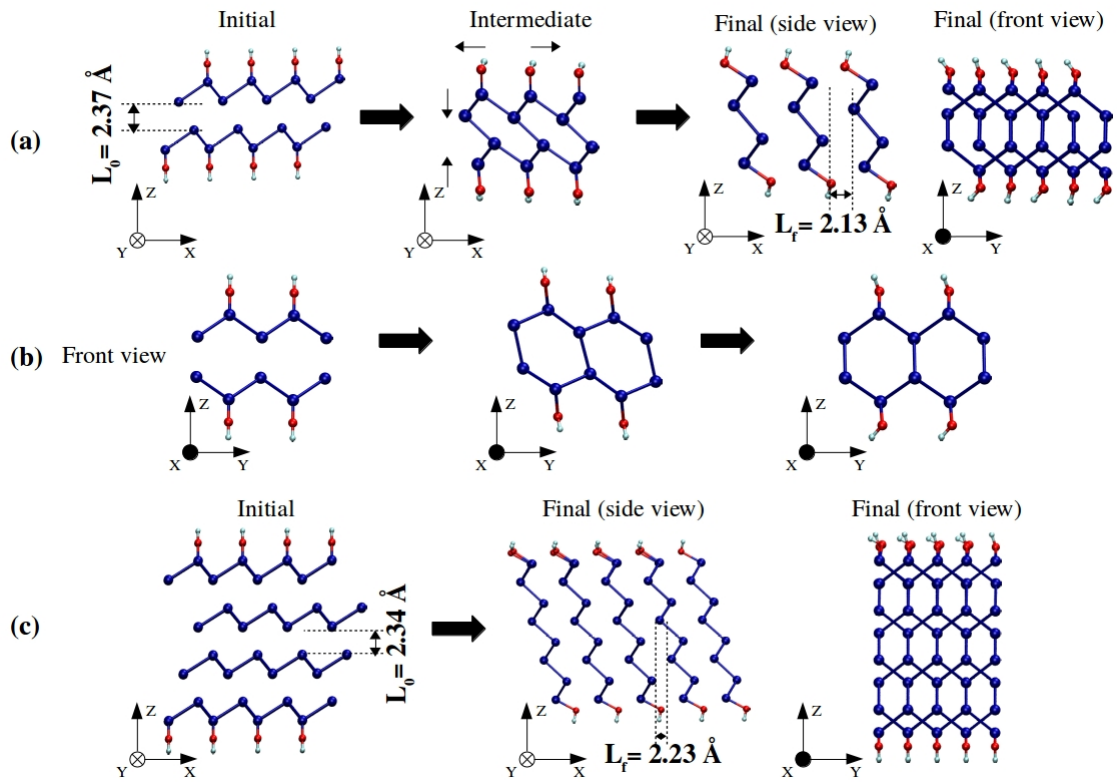

Figure 3.1 – Oxidation-driven formation of ordered antimonene multiribbons. (a) Initial, intermediate and final steps in the geometric relaxation of a -OH functionalized bilayer antimonene. The oxidation with hydroxyl groups induces the formation of interlayer bonds and the disruption of lateral Sb-Sb bonds. The arrows in the intermediate step emphasize these trends. The result is a multilayer one-hexagon-width zig-zag ribbon, shown in side and front views in the right panel. (b) Front view of the restructuring process emphasizing the edge sliding which leads to a perfect alignment of zig-zag edges. For clarity purposes, we omitted the neighboring atoms. (c) The four-layer antimonene case: initial geometry and two views of the final structure corresponding to a 10.61-Å-width multilayer ribbon. Antimony, oxygen and hydrogen atoms are represented by blue, red and white circles, respectively.

3.4 Results and discussion

3.4.1 The restructuring process

Figs. 3.1-(a) and 3.1-(c), on the left, show the models for two- and four-layer antimone fully oxidized with OH radicals. We found analogous results for F, so we will skip them. The initial geometries, with the z-axis defined as stacking direction, present the extra species placed in a covalent distance from the topmost and bottommost Sb atoms in previously optimized antimonene structures. The middle panel in Fig. 3.1-(a) shows an intermediate step in the geometric relaxation, in which the layers approach each other along z-direction, generating interlayer bonds. Simultaneously, lateral displacements, indicated by arrows in the figure , tend to disrupt the Sb-Sb bonds in the in-plane x-direction, while a sliding of zig-zag Sb-SbOH-Sb

terminations along the y-direction tend to align the edges, forming a sequence of periodic bucked hexagons. Fig. 3.1-(b) shows this latter restructuring omitting neighboring atoms for clarity purposes. The result is a complete transition to an array of zig-zag nanoribbons, as the right panel in Fig. 3.1-(a) and 3.1-(c) show: each ribbon has periodicity along the y-direction, the stacking is along the x-direction, and the ribbon width is measured along the z-direction. The ribbon width is, therefore, fixed by the initial number of layers, being a single-hexagon size (5.47) for a bilayer-originated structure and increasing by a half-hexagon size for each additional layer in the initial sample. Our calculations suggest that this phenomenology occurs for initial structures up to eight layers, which result in a 25.61-Å-width ribbon.

Structural and energetic aspects support the classification of the final structures as multilayer ribbon systems. Indeed, as indicated in Fig. 3.1-(a) and 3.1-(c), the distances L_f between ribbon layers are, respectively, 2.13 and 2.23 Å, close to the interlayer distance in the original geometry (L_0 = 2.37 Å), while the Sb-Sb bond length formed during the restructuring process is 2.89 Å, again consistent with the covalent bond in the initial structure, which was 2.90 Å. The interlayer distance is measured as the smallest vertical distance between Sb atoms – since these atoms are not aligned, the smallest Sb-Sb distance in adjacent layers is larger, 3.26 Å, which is enough to charatecterize it as non-covalent.

3.4.2 How strong are interlayer interactions?

The nature of the interlayer interaction may be quantitatively characterized by evaluating the order of magnitude of the binding energy. In fact, by calculating the total energy as a function of the distance L between layers, we estimated the bulk binding energy to be 163 meV/atom, which is higher, for instance, than that found for MoS_2 (60 meV/atom) [86]. As for the multilayer ribbons, especifically the one-hexagon-width ribbon originated from the oxidized bilayer antimonene, a similar set of calculations yields a binding energy of 189 meV/atom, larger than the Sb bulk value, but keeping the same order of magnitude. Fig. 3.2-(c) summarizes these results, and suggests that the layer interaction in the ribbon system is similar to that found in the stacked bulk, with van der Waals and orbital overlap contributions. The ribbons can be further characterized by determining hole and electron effective masses and carrier mobilities using an approach based on the calculation of the stretching moduli and deformation potentials [87]. We found relatively small effective masses (0.229 and 0.143 m_e for isolated ribbons originated from mono- and bilayer antimonene, respectively). However, due to edge effects, deformation potentials are large, yielding relatively small carrier mobilities (in the range 10^1 – 10^2 $cm_2V^{-1}s^{-1}$, see appendix **??** for details and calculation methods).

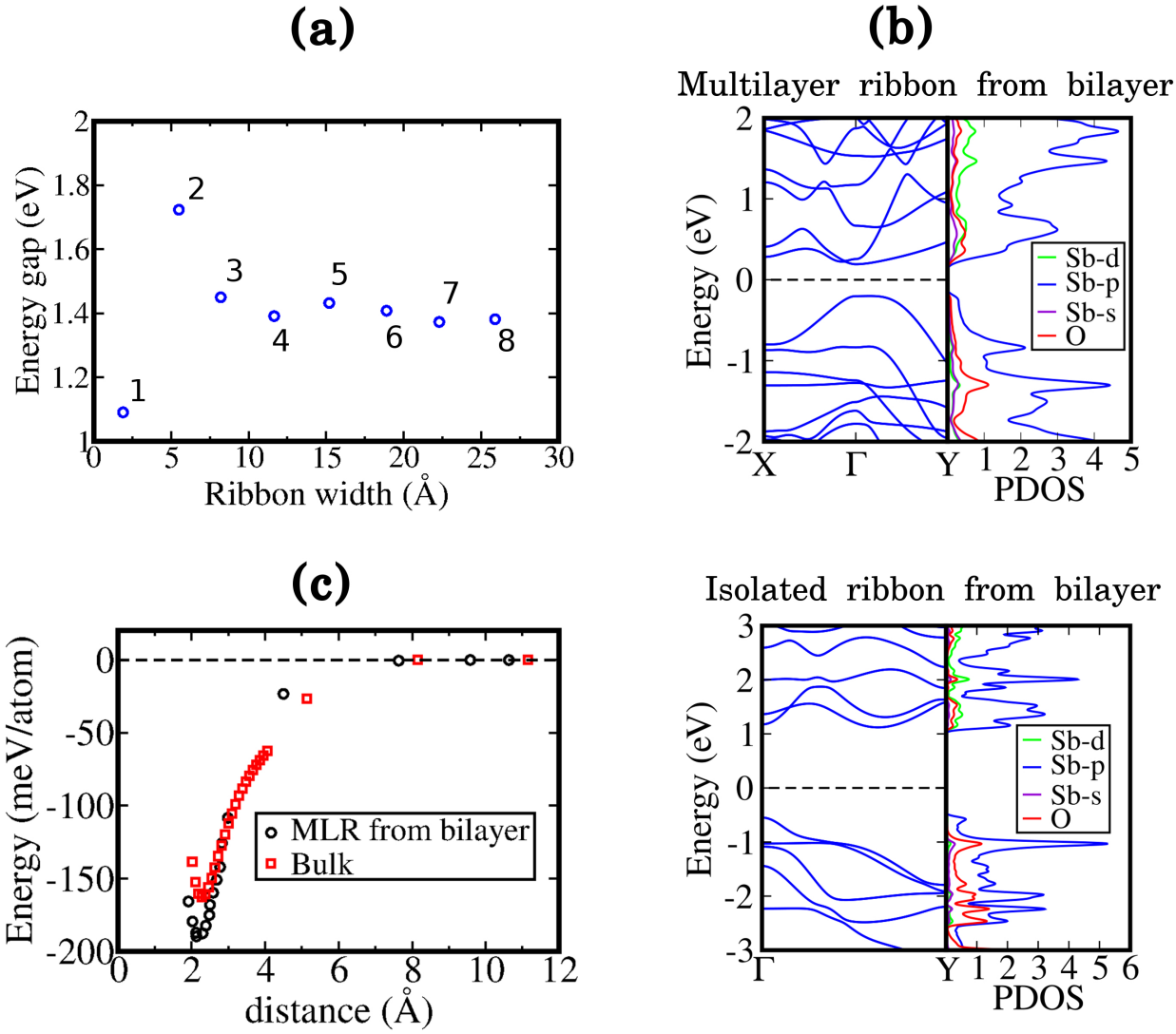

Figure 3.2 – Binding energy and electronic properties of the resulting antimonene ribbons. (a) Band gaps of the isolated ribbons as a function of the width of the final ribbon. The numbers close to the points indicate the number of antimonene layers in the initial structures. (b) Band structures and corresponding projected density of states (PDOS) for the multilayer ribbon (upper plot) and an isolated ribbon (lowerplot). The Fermi level is set to zero in both plots and is indicated by dashed lines. The ribbons are along the Y-direction and the stacking direction is the X-axis.(c) Total energy as a function of the distance between layers for bulk antimonene (redsquares) and for the multilayer ribbon (MLR) system originated from the bilayer antimonene (black circles). The binding energie sare 163 and 189 meV, respectively.

3.4.3 The final electronic structure

The electronic structure also gives a picture consistent with this idea. Fig. 3.2-(b) shows the band structures and corresponding projected density of states of the one-hexagon-width system for the multilayer ribbon (upper panel) and for an isolated ribbon (lower panel). In both, the ribbon axis is along the Y-direction, and the states close to the Fermi level (set to zero) come

predominantly from the 5p states of antimony. Quantum confinement is responsible for a band gap of 1.73 eV in the isolated case. This band gap decreases for wider ribbons, as expected – for the system originated from the three-, four- and seven-layer antimonene the values are 1.45, 1.39 and 1.37 eV, respectively, as shown in Fig. 3.2-(a). All band gaps are direct in the isolated structures, as reported for passivated zig-zag Sb ribbons. The change in the electronic structure upon stacking, a clear feature shown in the upper panel of Fig. 3.2-(b), reflects the pseudolayered character of Sb systems and is also present in the 2D antimonene case [61].

3.4.4 The monolayer case

A special case concerns the monolayer antimonene. As mentioned in chapter 2, its complete oxidation with O atoms has been described in the literature [69]. The result is still the buckled hexagonal lattice, with a larger lattice parameter (4.73 Å). The Sb-O bond in this structure has a strong polar character due to high electronegativity of Sb compared to O and the availability of the electron lone pair in Sb [69]. We have also carried out calculations for this case and we found similar results: a lattice parameter within 5% relative to the value reported in literature, and no disruption of in-plane Sb-Sb bonds. However, we did find that a change of the oxidizing specie may induce the same phenomenology previously described for two-, three- and four-layer antimonene, this time leading to the narrowest possible ribbon or stripe, that is, a layered (or pseudolayered) Sb zig-zag chain. Fig. 3.3-(a) shows the initial OH-functionalized Sb monolayer and the resulting chains. Their stacking induce a semimetallicity in the otherwise direct band gap behavior, as shown in Fig. 3.3-(b).

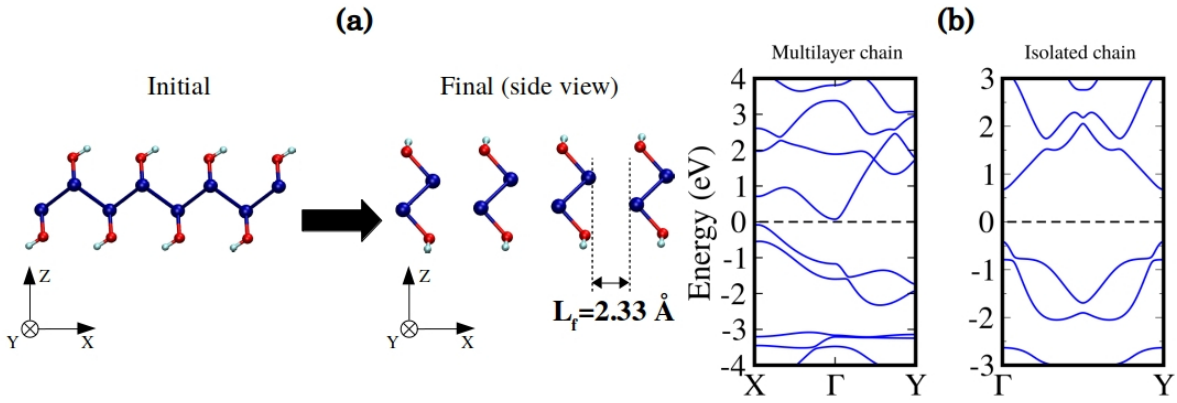

Figure 3.3 – The case of monolayer antimonene. (a) Initial and final structures for antimonene functionalized with -OH groups. The relaxation leads to multilayer zig-zag chains, the narrowest possible 1D structures. (b) Band structures of the multilayer system (left) and of the isolated chain (right). The semimetallicity of the multilayer configuration evolves to a semiconducting behavior in the isolated case.

Having established the mechanism to generate ordered ribbons, four relevant questions must be addressed: How would such ribbons be important to the material science field?; Would it be possible to extend the proposed mechanism to other materials?; and, How to experimentally

realize the proposed ribbon formation mechanism?; and, finally, does a single-side functionalization yields the same phenomenology? The answer to the first question is twofold. First, antimonene ribbons are related intriguing physical phenomena. Application of strain and/or transverse electric field combined with effects induced by the spin orbit coupling may lead to modulation of electronic properties [81], and behaviors dictated by topological order [48]. It leads, therefore, to a rich physical phenomenology which may shed light on the electronic behavior at nanoscale. Secondly, the band gap range found in antimonene ribbons may pave the way for applications related to optical properties as well as to nanoelectronic devices [82].

3.4.5 The arsenene case

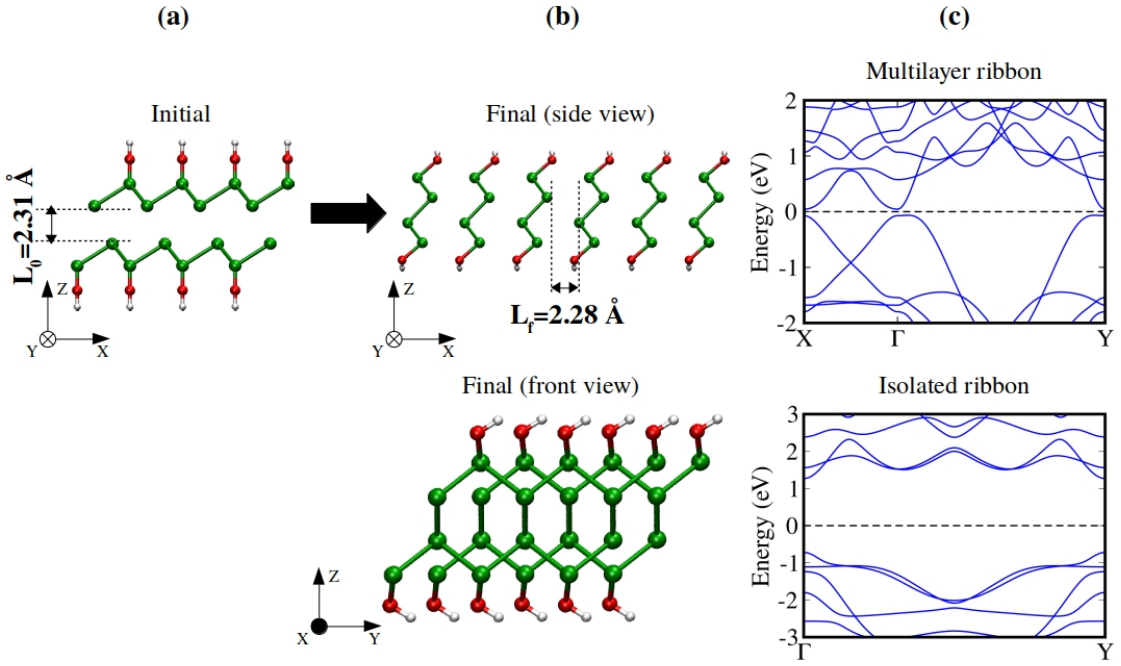

Figure 3.4 – The case of arsenene. (a) Initial geometry for bilayer arsenene functionalized with -OH groups. Arsenic, oxygen and hydrogen atoms are denoted by green, red and white circles, respectively. (b) Two views of the final structure. The system evolves to a multilayer ribbon configuration following the same path described for antimonene. (c) Band structures for the multilayer ribbon (upper plot) and for an isolated ribbon (lower plot).

For the second question, we have conducted additional calculations to investigate the arsenene case, and the answer is affirmative. Arsenic and antimony have similar bulk structures. Like in antimonene, strain-induced topological transitions in the electronic behavior is present in arsenene [88, 89], band gaps in arsenene ribbons depend on edge termination [90], and few-layer samples may be prepared in a liquid phase exfoliation procedure [91]. In Figs. 3.4-(a)-(b), we show that functionalization with OH groups turns a bilayer arsenene into a one-hexagon-width multilayer ribbon, exactly like in the antimonene case. As shown in Fig. 3.4-(c), the ribbon

system is semiconducting with a direct band gap of 0.12 eV (upper plot), and this value increases to 1.99 eV in the isolated ribbon (lower plot).

As for the third question, Zhang et al [69] suggest a series of experiments which could lead to fully oxidized antimonene samples, including protocols similar to those employed in graphene chemistry to yield graphane [88]. Besides, experiments in which 2D nanostructures are submitted to pressure in presence of chemical groups have been reported in the literature [92, 93], and the results indicate emergence of materials in which a covalent interlayer binding is mediated by functionalization. In particular, experiments conducted in pressure vessels [17] may expose both sides of the samples to the oxidizing agent. If performed with few-layer antimonene, the pressure may facilitate the restructuring mechanism and the oxidizing agents may be generated from the medium at both surfaces of the sample.

3.4.6 The single-side case

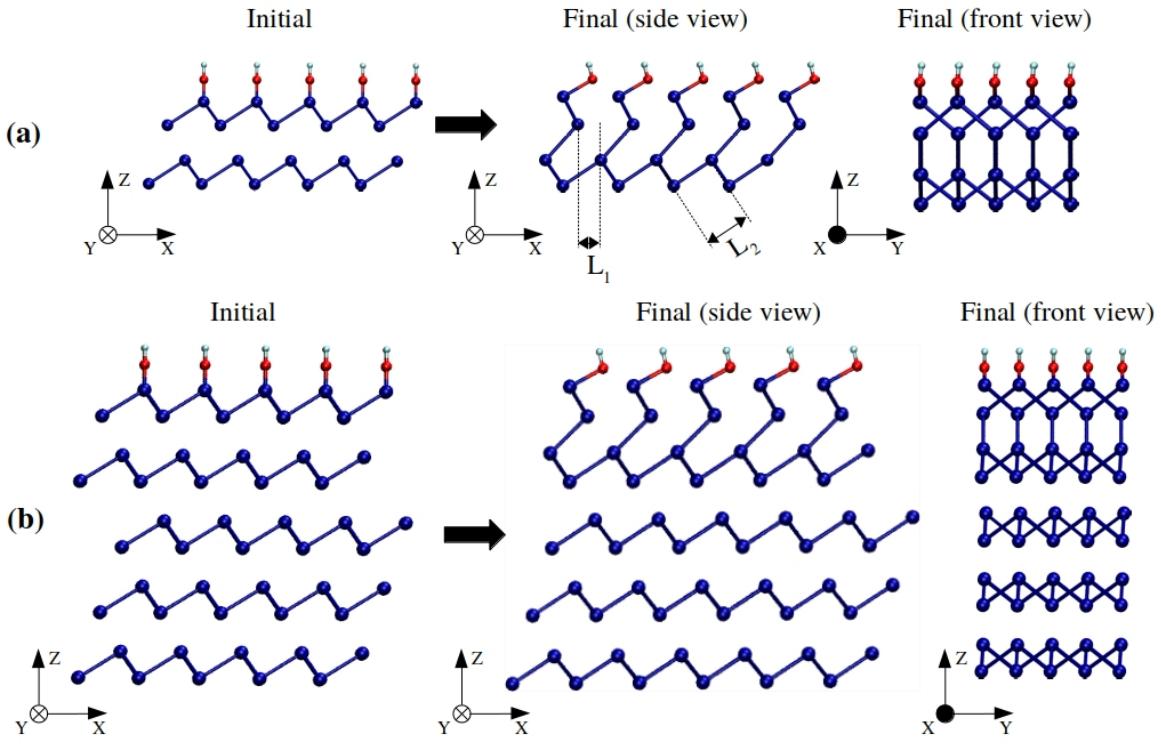

Figure 3.5 – Single-side OH-functionalized (a) bilayer and (b) five-layer antimonene. Initial and final geometries are shonw on the left and in the middle panels, respectively. Front views of the final geometries are shown on the right. Important to observe that interlayer bonds are formed only in the first two layers and disruption of lateral bonds are restricted to the first layer.

Finally, we have also addressed the fourth question – the single-side functinalization problem – through first-principles calculations. We found a partial restructuring. In fact, for all structures considered, including antimonene bilayer and multilayer systems up to eight layers,

interlayer bonds were formed only between the first two layers, and disruption of lateral bonds were observed only in the first layer. The resulting geometries for bi- and five-layer cases may be viewed in Fig. 3.5. We added the initial (left) and final (right) configurations, which ilustrates the above-mentioned phenomenology. More specifically, the interlayer distance (L_1 in Fig. 3.5-(a)) is 1.51 Å, which is small compared with the double-side functionalization (1.93 Å), and it is not enough to disrupt Sb-Sb bonds. These results are related to those observed by X. Peng and Q. Wei [22] and also by D. W. Bouklvalov et al [94] in monolayer phosphorene. They observed the so-called chemical scissors effect, which is responsible for the bond disruption in monolayer systems with orthorhombic symmetry.

3.5 Conclusion

In summary, our work shows that antimonene and arsenene multilayers may undergo a structural transformation upon functionalization with oxidizing agents. This transformation recovers the Sb-sp_3 original network, except at the chemically stabilized edges, and is characterized by the formation of well-ordered multilayer zig-zag nanoribbons whose widths are precisely determined by the initial number of Sb layers. With this process, it is possible to achieve ultranarrow structures and the electronic structure is strongly dependent on both the ribbon width and the number of stacked ribbons, suggesting potential applications in nano and optoelectronic devices. Since our work establishes a route for controlled synthesis of ordered ribbons, it provides a connection between a variety of theoretical predictions concerning physical mechanisms in antimonene structures and their experimental realization. These results were published in Journal of Physics: Condensed Matter 32.16 (2020): 165302, where I'm the first author of the paper.

4 Flat-band phenenomelogy in twisted antimonene bilayers

“Eu bolo o plano, os mano, e canto o esquema:
Triunfo, se não for coletivo, é do sistema”

O céu é o limite - Devastoprod feat Emicida

4.1 Introduction

In this chapter, we will discuss the possibility of flat band emergence on twisted antimonene bilayers for “non-magic” angles and how to tune the resulting bandstructure using non-covalent bonding.

The experimental observation of unconventional superconductivity in twisted bilayers graphene (TBG) [95] established a new milestone in the investigation of two-dimensional (2D) materials. After that, observation of insulating states [96], magnetism [97], and optically induced flat bands [98] showed that rotated multilayer graphene structures are a rich playground for fundamental physics, in which the existence of Bloch flat bands plays [99] a crucial role. One of the most important aspects of these findings is the strong rotation angle dependence, which is behind the existence of the so-called “magic angles” [100] for the observation of TBGs exotic properties. In these angles, the interlayer interactions become strong and the competition between kinetic and Coulomb potential changes the density of states giving rise to flat bands in the vicinity of the Fermi level. In addition, results for twisted double bilayer graphene (tDBG) [101] showed a strong stacking dependence of the flat bands in angles slightly higher than 1.1°, which suggests that it is possible to “functionalize” the TBG with controlled incorporation of 2D layers [102]. Besides graphene, other 2D van der Waals materials, such as hexagonal boron nitride (hBN), can also present interesting electronic modulation due to layer rotation. Indeed, theoretical results have shown the emergence of flat Bloch bands in twisted bilayer hBN without the magic angle mechanism [103] . In this case, different regions of moiré superlattice are characterized by different stacking patterns and, if the twisted angle is small enough, electronic states arising from these patterns could fall into the insulator gap and form non-dispersive bands with spatially localized wavefunctions. A common feature in all these systems is that the phenomenology occurs only for very small angles - 1.1° for TBG, less than 2.13° for tDTGB, and less than 3° for

hBN. Consequently, the theoretical descriptions of these states rely on tight-binding approaches or continuous models [104–109] which give important insights into the electronic structure and allow for the exploitation of its angular dependence.

There is yet another class of 2D materials in which the idiosyncrasies of the twisted configurations may show up with important particularities. The β phase honeycomb structures of the pnictogens As, Sb, and Bi are characterized by relatively stronger interlayer interactions, which classify these materials as pseudolayered compounds [61]. May these interactions drive localized out-of-plane deformations in rotated structures with separated regions of well defined stacking patterns? If this is the case, is it possible to establish an interplay between geometric distortions and electronic localization underlying the flat band phenomenology in these materials?

4.2 Objectives

In order to address the above questions, we define the following objectives to this chapter:

- We will seach for any sign of flat band emergence on the electronic bandstructure of twisted antimonene bilayers using several moiré superlattice;
- From the geometrically optimized moiré superlattices, we will investigate the importance of the interlayer displacements on the different stacking regions for each twisted structure;
- Lastly, we will use non-covalent bonding of electron donor molecules to modulate the electronic bandstructure of the moiré superlattice.

4.3 Computational details

We employed the SIESTA [39] implementation of the pseudopotential spin DFT formalism [29, 30], expanding the Kohn-Sham eigenfunctions in a finite range double-ζ basis set augmented by polarization functions (DZP basis set). We made use of the Gradient Generalized Approximation (GGA) within the Perdew-Burke-Ernzerhof (PBE) parametrization [35] for the exchange-correlation functional. We tested the flat-band phenomenology against a van der Waals density functional approach [85] and found overall similar electronic modulation. We employed a mesh cutoff of 450 Ry to define the grid for real space integrations, and the geometries were considered relaxed when the maximum force component in any atom was less than 10 meV/Å. To sample the Brillouin zone, we defined a k-grid using the Monkhorst-Pack scheme with 3x3x1, 7x7x1, 12x12x1 and 15x15x1 meshes for the 6.01°, 9.43°, 13.17°, and 21.79° structures, respectively.

4.4 Results and discussion

4.4.1 The twisted structures

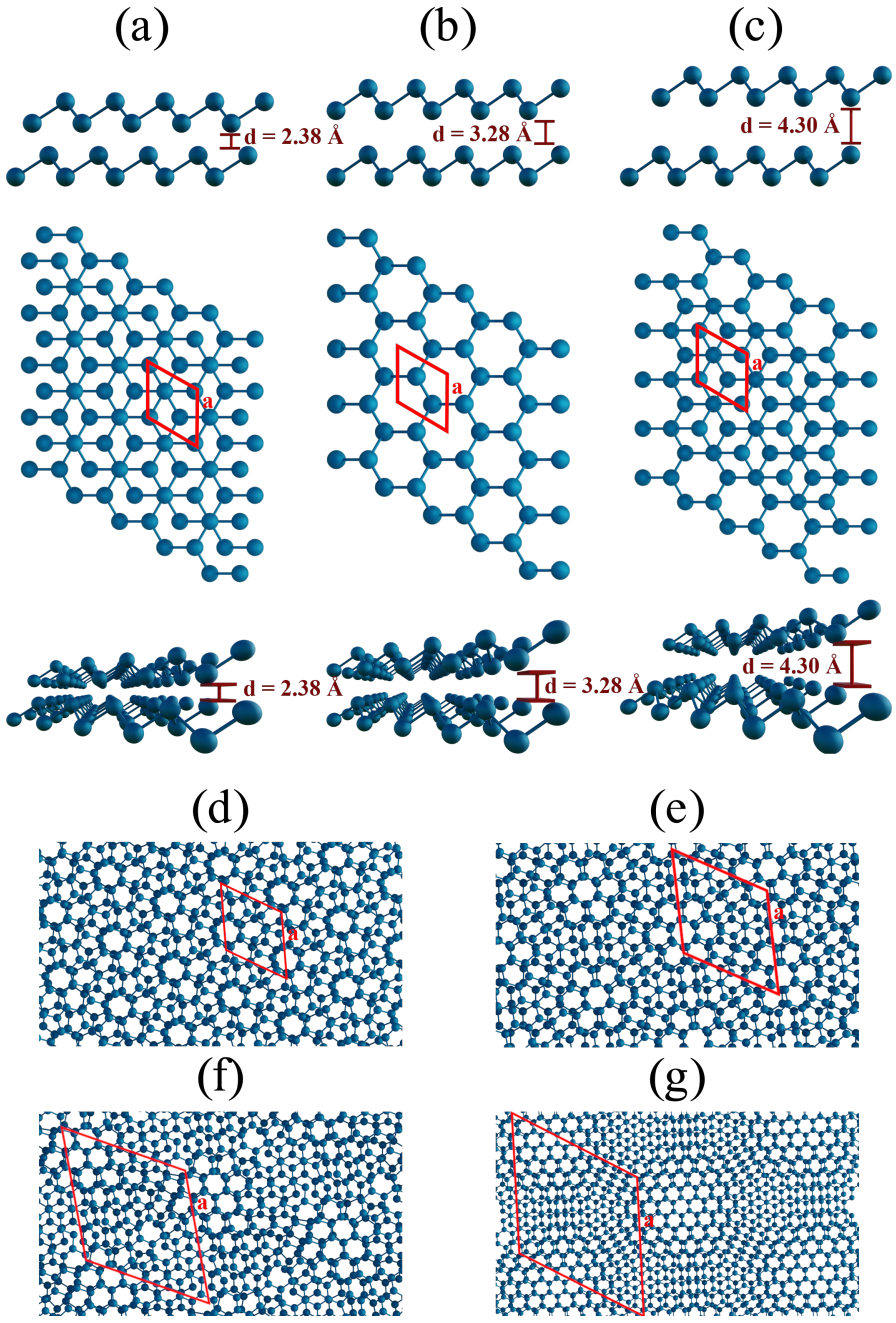

Figure 4.1 – Bilayer antimonene: Optimized structures for (a) AB, (b) AA and (c) AC stacking orders in side view (upper panel), top view (middle panel) and in perspective (bottom panel). Top views of the relaxed rotated bilayer antimonene structures with twist angles of (d) 21.79°, (e) 13.17°, (f) 9.43°, and (g) 6.01°. In the top views, the primitive cells are indicated by red lines.

Figs. 4.1-(a) - (c) show top and side views of bilayer antimonene built upon the β-phase in three stacking orders, AB, AA and AC, respectively. The AC stacking may be constructed

from the AB by translating the top layer of two-thirds and one-third in the direction of each in plane lattice vector, respectively. The same procedure in the bottom layer leads to the AA stacking. Important to the reasoning we shall pursue in this project, the relative orientation of the atoms in different layers, as the side views in Fig. 4.1 clearly show, implies a strong dependence of the interlayer distance with the stacking order: 2.38, 3.28, and 4.30 for AB, AA, and AC, respectively, as determined by DFT calculations within our implementation scheme, which also indicate the AB as the energetically most favorable bilayer stacking, followed by AA and AC (0.018 and 0.039 eV/atom relative to AB, respectively).

Therefore, in our models, we started from the AB stacking, and we built four moiré superlattices with twist angles of 21.79°, 13.17°, 9.43°, and 6.01°. The models comprise 28, 76, 148 and 364 atoms, respectively. For each of them, we performed a full geometry optimization. We show in Figs. 4.1-(d) - (g) the top views of the resulting structures, which allow for a clear identification of AA domains. The distance between these domains constitute the moiré length – we found 10.9, 17.9, 25.1, and 39.5 in each case, respectively.

4.4.2 The twisted electronic band structure

Next, we characterized the electron states for each moiré superlattice by determining the DFT band structures, as shown in Fig. 4.2. The semiconducting behaviour with indirect energy gap is a common feature. A sizable reduction of the bandgap upon decreasing twist angle is clearly seen - the energy difference between the bottom of the conduction band and the occupied band indicated by a blue curve in the figure varies from $\sim$1.0 eV (21.79°) to $\sim$0.4 eV (6.01°). Concerning the flat band formation, the effect of the twist angle shows up as a notable modulation of the valence band maximum (VBM, highlighted in blue in all figures) from dispersive (Fig. 4.2-(a) with 21.79°) to completely flat (Fig. 4.2-(c) with 6.01°). In this respect, the results are similar to those reported for the other pnictogens, phosphorous and arsenic, both β-phase bilayers [110, 111]. Fig. 4.2 indicates that the band evolution can be addressed in three steps: (I) The VBM for 21.79° is still slightly dispersive and mixed with other valence bands (Fig. 4.2-(a)); (II) For 13.17°, a great decrease in the VBM band dispersion leads to quasi-flat isolated bands in the proximity of the other valence bands (Fig. 4.2-(b)); (III) For 9.43° and 6.01° (Figs. 4.2-(c) and (d), respectively), well-defined dispersionless bands within the bandgap are clearly distinguished in the band structures.

This is interesting since unconventional superconductivity [95] and insulating strongly correlated states [96] are ascribed to the existence of flat bands below the Fermi level in twisted structures, but only for very small magic angles. The emergence of flat bands in the relatively greater twist angles shown in Fig. 4.2 is mostly due to two important physical aspects of antimonene which we shall discuss in the next section: the strong interlayer interactions and the atomic displacements in the different stacking patterns across the superlattice.

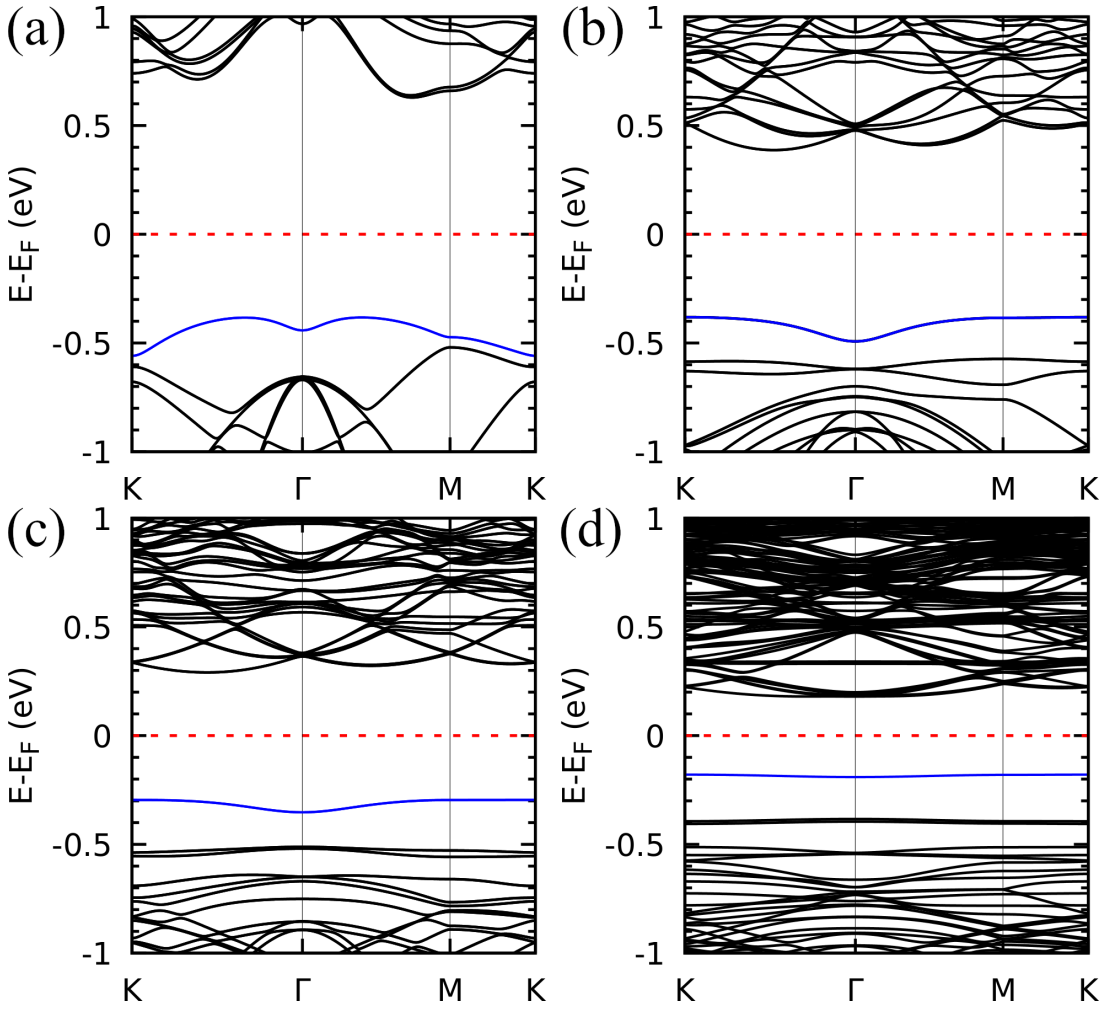

Figure 4.2 – The flat band emergence: Band structure for the twist angles (a) 21.79°, (b) 13.17°, (c) 9.43°, and (d) 6.01°. The valence band maximum is highlighted in blue for visualization purposes. The Fermi level is set to zero.

4.4.3 Electronic localization and interlayer displacements

To pursue a further understanding on the nature of the flat bands, we reproduce in Fig. 4.3-(a) the band structure for the 9.43° twisted Sb bilayer, presenting also the projected density of states (PDOS). The predominant contribution to the flat bands comes from p_z orbitals due to the expected hybridization scheme in hexagonal structures and the consequent role of the alignment of p_z orbitals in the interlayer orbital overlap, which defines the strength of interlayer interactions.

This points out to the importance of geometric aspects in defining these interactions. To characterize these aspects in greater detail, we first show that, similar to the phenomenology reported for hBN [103], the electronic density associated to the flat bands is well localized in real space. Indeed, Fig. 4.3-(b) presents an electron density isosurface plot corresponding to the flat band (indicated by the blue curve in Fig 3(a)), clearly showing its localized character, which, as we shall show, is related to well separated AB stacking patterns within the superlattice.

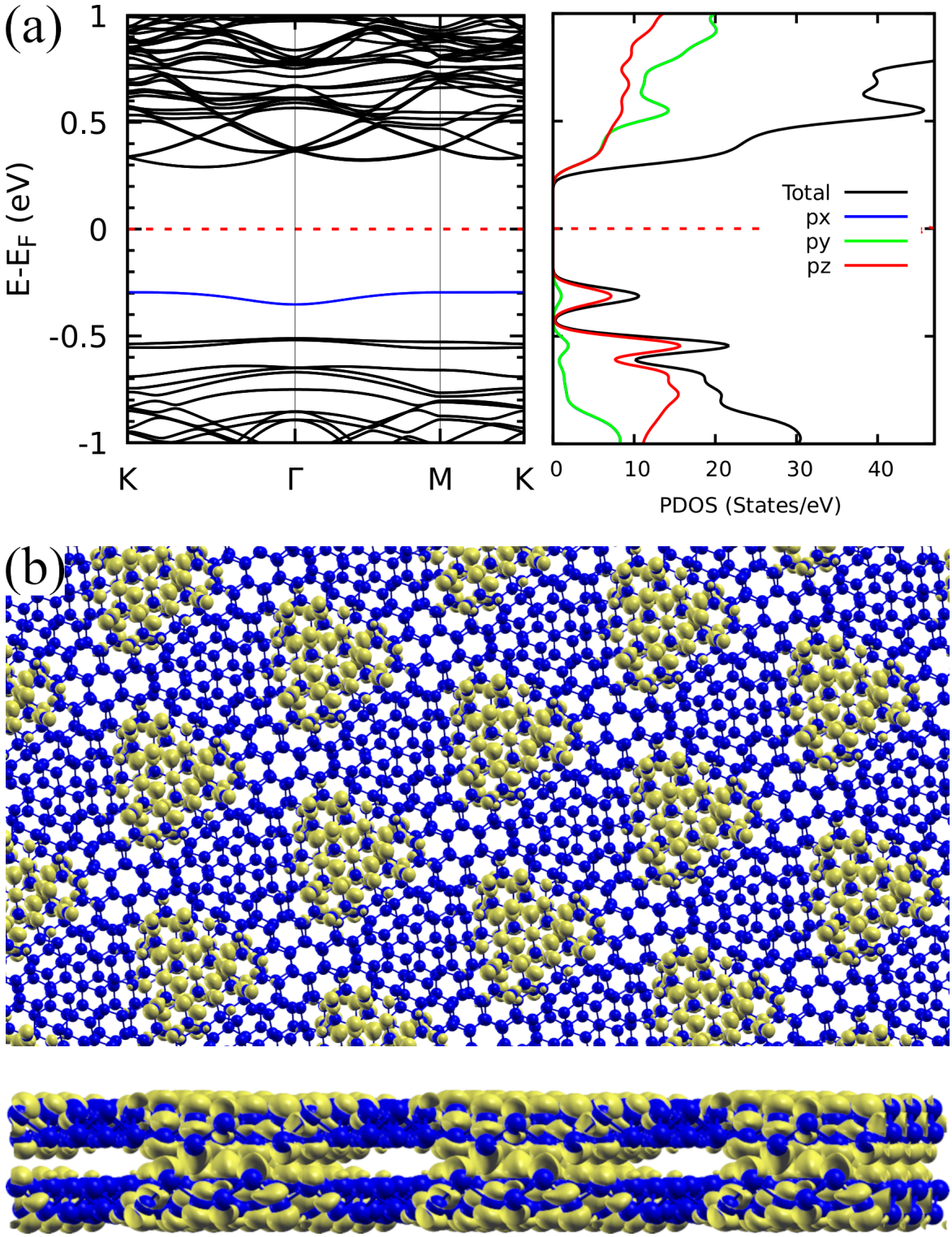

Figure 4.3 – Orbital character and localization for the 9.43° case: (a) Band structure for the bilayer antimonene twisted in 9.43° and projected density of states. (b) Top and side views of the corresponding relaxed structure (antimony atoms represented by blue spheres) superimposed to the isosurface plot of the charge density associated to the flat band highlighted in blue in the band structure. The isosurface value is of 0.00015 electron/Bohr^3.

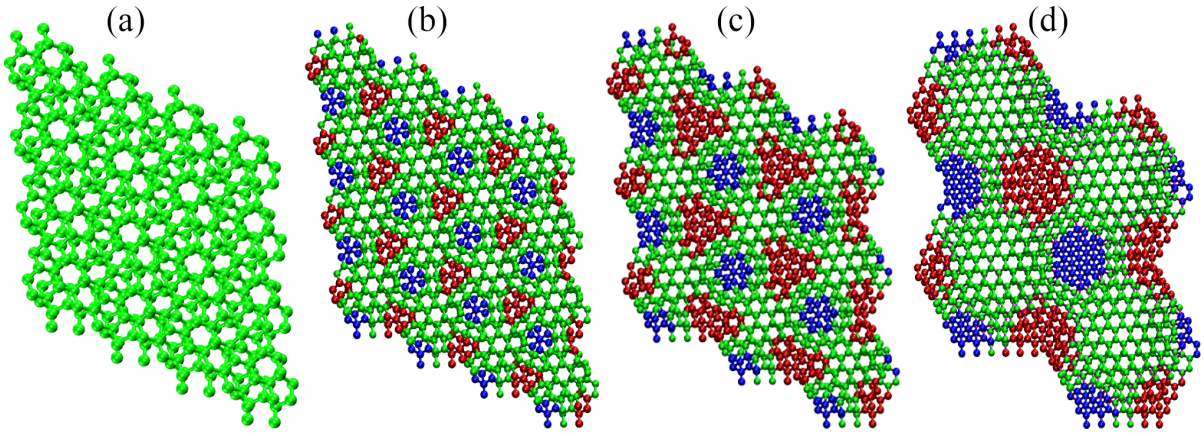

Figure 4.4 – Stacking patterns in Sb superlattices: From left to right, the relaxed geometries for antimonene bilayers twisted in (a) 21.79°, (b) 13.17°, (c) 9.43°, and (d) 6.01°. Green, blue, and red spheres represent atoms with vertical distances typical of those of the AA, AC, and AB stacking configurations, respectively.

Moreover, the bottom panel of Fig. 4.3-(b) suggests a crucial peculiarity of the pnictogen case: out-of-plane displacements for small angles in the vicinity of the AB stacking patterns, which enhances the electronic density in the interlayer region. The phenomenology can be clearly visualized in Fig. 4.4, and relies on the fact that, in the lowest energy AB configuration of the Sb bilayer, the interlayer distance is smaller than those of the other stackings (2.38, 3.28, and 4.30 for AB, AA and AC, respectively). Figs. 4.4-(a) - (d) show the four twisted configurations in a representation in which the green, blue and red spheres represent Sb atoms with interlayer distances characteristic of the AA, AC and AB stackings, respectively. For large twist angles,as shown in Fig. 4.4-(a) for 21.79°, the moiré length is small and the stacking patterns are poorly defined. As a consequence, the interlayer distance is rather uniform along the structure and matches that of the AA pattern. On the other hand, when the moiré length is high enough to create and isolate well defined regions with AB, AA and AC patterns, as shown in Figs 4.4-(b) - (d) for 13.17°, 9.43°, 6.01°, respectively, out-of-plane displacements may be stabilized in the AB and AC regions. This must have profound consequences in the tunneling between layers, which is associated with flat bands [100].

4.4.4 Non-covalent flat band modulation

Once the flat band phenomenology has been established, a question arises on the possible modulation of its energy position. A possible strategy may be based on non-covalent functionalization with electron acceptor molecules. In fact, Abellan G. et al [112] have reported the efficiency of this mechanism in tailoring the electronic properties of few layer antimonene through formation of stable complexes involving, for instance, tetracyanoquinodimethane (TCNQ - $C_{12}H_4N_4$) molecules. Therefore, we performed calculations for TCNQ interacting with bilayer antimonene twisted by 13.17°. We considered adsorption onto sites with stacking patterns

characteristic of the AA, AB and AC configurations.

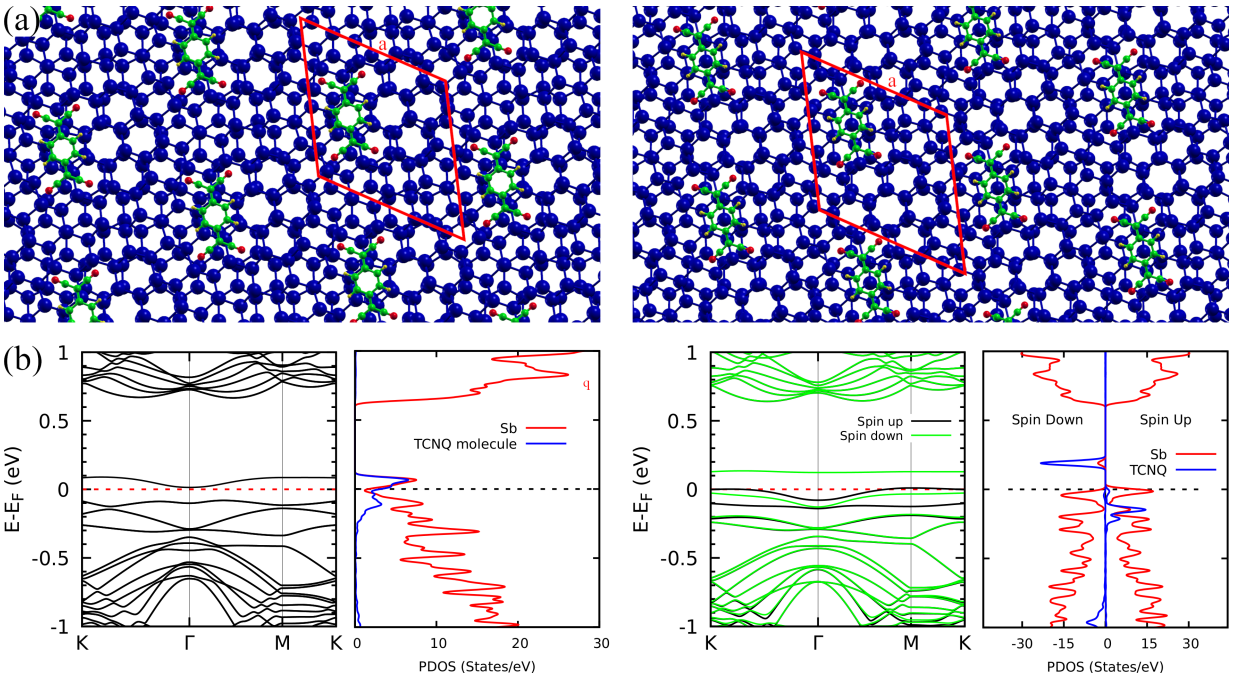

Figure 4.5 – The Sb + TCNQ case: (a) Relaxed structures for the 13.17° twisted antimonene bilayer with the TCNQ molecule adsorbed initially onto the AB (left) and AC (right) regions. The blue, green, red, and yellow spheres represents the Sb, C, N and H atoms respectively. (b) Bandstructure and projected density of states for the AB (left) and AC (right) cases. The electronic states shown in the bandstructure on the left are not spin polarized. In the bandstructure shown on the right, green and black curves represent the two spin components. The blue and red curves of the PDOS plots represent projections on the TCNQ molecule and on the Sb atoms, respectively.

Figs. 4.5-(a) - (b) show, respectively, the relaxed geometries (upper panels) and band structures with the corresponding projected density of states (bottom panels) for the AB (left) and AC (right) cases. We omitted the AA electronic characterization since it is very similar to the AB case. For the AB case, the TCNQ molecule shifts to a region between the AB and AA patterns during the geometric optimization, as shown in the left panel of Fig. 4.5-(a). For all relative positions, we verified the strong charge transfer nature of the interaction, which defines the low energy features of the spectra. In the AC configuration, shown in the right part of the figure, this brings an antimonene flat band to the Fermi level, while the states associated to the molecule become spin polarized and can be clearly identified above and below the Fermi level. For the other configurations, as shown on the left of Fig. 4.5-(a) for the AB case, flat states are found at energies $\pm$ 0.1 eV from the Fermi level, and present a high degree of hybridization between antimonene and the molecule. Adsorption on the AC pattern is energetically more favourable by 0.044 and 0.127 eV when compared to AB and AA patterns, respectively. This phenomenology

is not restricted to a specific twist angle: We observed similar trends - the shift of flat states to the Fermi level - in calculations performed for a twist angle of 6.01°.

4.5 Conclusions

In conclusion, through first-principles calculations, we demonstrated a rich interplay between structural and electronic aspects involved in flat band formation in twisted antimonene bilayers. The phenomenology has similar aspects to those observed in polar compounds, such as hBN, with well-separated stacking patterns determining the localization of flat bands. However, due to strong interlayer interactions in pnictogen compounds, which greatly distinguishes interlayer distances in different stacking patterns, the process in the Sb bilayer involves large out-of-plane deformations, which, in turn, allows for electron localization and the emergence of flat bands in relatively higher twist angles when compared to other 2D material. Moreover, using well-established techniques for noncovalent functionalization with electron acceptor molecules, it is possible to modulate the energy position of the flat bands, positioning them close to the Fermi level. Altogether, our work reinforces the idea that antimonene is an important material for the exploitation of fundamental physical phenomena, such as strongly correlated insulating states and superconductivity. We published these results in RSC advances 11.45 (2021): 27855-27859, where I'm the first author of the paper.

5 Low temperature effects on antimonene monolayer phonon bandstructure

“Eu 'tô puro ódio, revolta no pódio
Futuro rasgado, 'cês 'tão entendendo
Carro rebaixado, o som 'tá no talo
Favela não vence, tamo no veneno”

Cleane - Criolo

5.1 Introduction

In this chapter, we will discuss the low temperature effects on the vibrational modes of the antimonene monolayer using ab initio molecular dynamics calculations. This project was developed during a doctoral exchange in the United States with Prof. Vincent Meunier at the Rensselaer Polytechnic Institute.

The continuing pursuit for new two-dimensional nanomaterials with physical and chemical properties suitable for technological applications has led to the discovery that atomically thin group-V semiconductors such as P, As, Sb, and Bi present desirable properties that make them suitable for integration in nanodevices [113–117]. For example, the most stable allotrope of P is called black phosphorus (BP) with a layered puckered honeycomb structure. BP has attracted increasing attention due to its tunable direct bandgap [118, 119], relatively high carrier mobility [120], and anisotropic thermal conductivity [23]. However, one of BP’s major disadvantage is its low stability due to poor resistance to oxidation at room temperature [121]. As alredy mentioned, antimonene also presents compelling physical properties such as layer-dependent band-gap transitions [44, 122], and thickness/strain dependent topological transitions [48, 50], making it a suitable candidate for quantum nanodevices [115, 123].

Recent experimental Raman studies have demonstrated that few-layer antimonene presents strong anharmonic effects on the phonon bandstructure in the high-temperature (HT) regime - from 300 to 600 K, which is an important range in device operation [124]. The analysis of the experiment establishes the existence of a linear phonon frequency dependence with temperature, for both E_G and A_{1G} phonon modes. The frequency versus temperature dependence is markedly higher than of several other two-dimensional nanomaterials such as graphene, hBN, MoS_2, and BP [124]. To date, no theoretical or experimental evidence is available on the low-temperature anharmonic effects on antinomenene phonon bandstructure, which is also important

in developing antimonene-based quantum nanodevices in a broader range of temperatures. Further, it remains unclear, based on existent experimental data alone, if the strong anharmonicity stems from out-of-plane interactions or from intralayer interactions.

5.2 Objectives

The main objectives of this chapter are:

- Use the velocity autocorrelation method to calculate the power spectra of the antimonene monolayer projected on the Γ point to shed light on the magnitude of the anharmonic effects on the low-temperature regime - 25 K to 300 K on the phonon frequencies;
- Compare the low-temperature anharmonic effects to the high-temperature case and with other two-dimensional nanomaterials;

5.3 Computational details

The phonon bandstructure was obtained using Phonopy code and VASP [125–128] plane-wave DFT calculations with the GGA - PBE [35] exchange correlation function. Projector augmented wave psedupotential [129] was used with an energy cutoff of 500 eV for all calculations and tolerance for the electronic loop was set to $10^{-}5$eV. We used a 4x4 antimony monolayer supercell with 12Åvacuum region, 4x4x1 Γ centred K-points sampling and Gaussin smaering of 0.01eV/Å. The Ab Initio MD was carried with a 3x3 supercell, 3x3x1 Γ centred K-points sampling, and $0.5fs$ time-step for $40ps$. We fixed the temperatures ranging from 25 K to 600 K using a Nosé-Hoover chain thermostat [37, 130, 131].

5.4 Results and discussion

5.4.1 The antimonene phonon bandstructure

The transition from bulk to few-layer antimonene leads to some of the most interesting properties regarding its application for nanodevices. Besides semi-conductor to metal and topological transitions, one particularly important transition is seen directly on the phonon frequencies. Raman spectra for bulk antimony feature two frequency peaks, the E_G and A_{1G}, around 110 and 151 cm^{-1}, respectively. A strong shift is observed as the thickness of the antimony flake hits the few-layer level - reaching around 140 and 166 $cm^{-}1$ for a 5 nm flake, for E_G and A_{1G}, respectively [65]. The antimonene monolayer has a hexagonal buckled structure with lattice parameter a = 4.10 , as one can see in the right side of Fig. 5.1-(a).

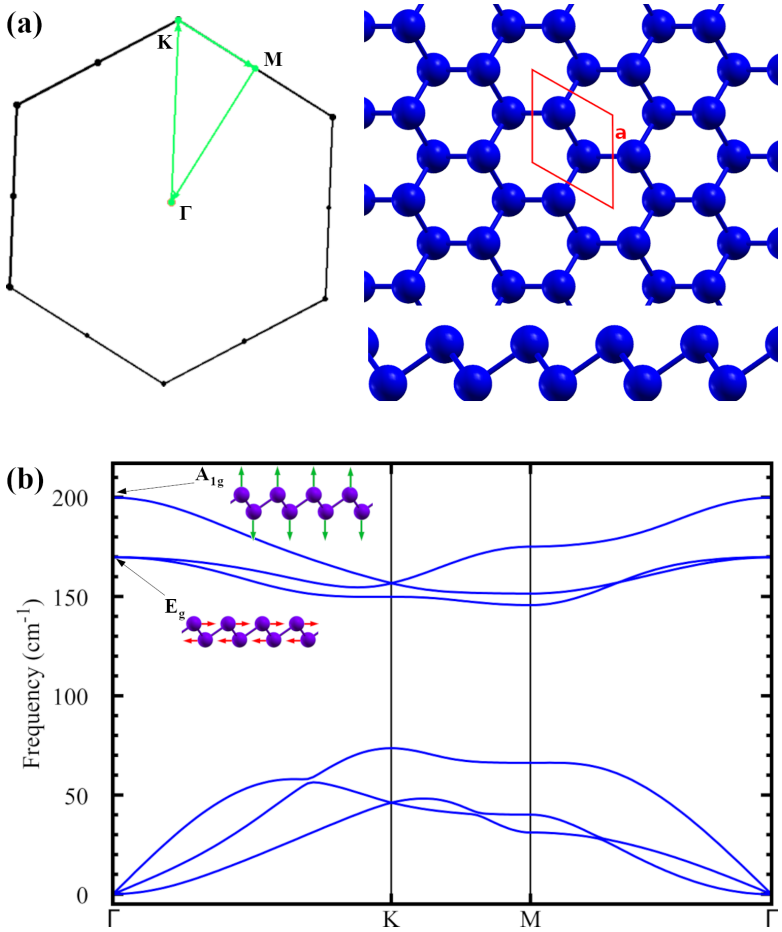

Figure 5.1 – (a) Brillouin zone with the path along the high symmetry points (left) and the Antimonene monolayer geometry (right) with the lattice parameter a = 4.32 A and the unit cell represented by the red lines.(b) The antimonene phonon bandstructure at the DFT level. The A_{1G} and E_G vibrational modes are represented in the inset where the arrows points to the direction of the atomic movement.

Using Phonopy and VASP codes, we obtained the antimonene monolayer phonon dispersion following the path in the high-symmetry points of the Brillouin zone as shown in the left hand-side of Fig. 5.1-(a). The results are shown in Fig. 5.1-(b) together with the representation of the phonon vibrational modes. We found the 161 and 199 cm$^-$1 for or E_G and A_{1G},respectively, which follows the same trend of shift to higher frequencies observed in the experimental data and also close to that reported in the literature [45]. There are two degenerate in-plane optical modes at 161 cm^{-1} and one optical out-of-plane mode at 199cm^{-1} which are visualized in Fig. 5.1-(b), where the arrows point to the direction of motion. It is important to notice that the phonon frequencies obtained by the DFT method within the harmonic approximation miss any temperature and non-linear effects. This means that anharmonic effects such as scattering and three phonon processes do not contribute to the phonon bandstructures shown in Fig. 5.1-(b).

5.4.2 The power spectra from molecular dynamics

Within the computational material science community, one of the most widely used methods to investigate anharmonicity (and, in turn, temperature dependence of the phonon frequencies) is the velocity auto-correlation function (VACF) [23–26]. From the trajectories of *ab initio* molecular dynamics calculations performed on a supercell using the canonical ensemble, one can obtain the velocities at each time-step t for each of the N atoms and then project the result onto any commensurable $\mathbf{k}$ point in the unit cell atoms using:

$$\mathbf{v}_i^{\mathbf{k}}(t) = \sum_{\rho} \mathbf{v}_{\rho N}(t) e^{-i\mathbf{k}\cdot\mathbf{X_0}}, \tag{5.1}$$

where the sum ρ goes over all the unit cell replicates in the supercell and X_0 is the initial atomic position of the atoms. The power spectra are obtained by the absolute value of the Fourier transform of the VACF [23]:

$$P(\omega) = m \left| \int_{-\infty}^{+\infty} \sum_{N} \left\langle \mathbf{v}_i^{\mathbf{K}}(t) \cdot \mathbf{v}_i^{\mathbf{K}}(t+\tau) \right\rangle \mathrm{e}^{-i\omega\tau} \mathrm{d}\tau \right|, \tag{5.2}$$

where m, ω, and τ are the atomic mass, phonon frequency, and time-step, respectively. By analysing the shifts of peaks in the power spectra for different temperatures, one can determine the magnitude of anharmonic effects compared with the phonon bandstructure obtained by standard harmonic approximations.

In order to obtain the temperature-dependent phonon frequency and include anharmonic effects, we performed the AIMD calculations, collected the trajectories of the supercell for each time step during the 40.0 ps of the simulation and calculated the velocity. We ran several simulations with temperatures between 50 K and 300 K - at 50 K intervals, as well as 25 K and 600 K - and calculated the power spectra for each of them. Firstly, Fig. 5.2-(a) shows the power spectra calculated using all the velocity components (v_x, v_y and v_z) in equation 5.2. One can see a strong shift for both vibrational modes, even at temperatures in which the peaks are broadened. The broadening we calculate has two major contributions: (1) an intrinsic one due to the physical process and (2) a numerical contribution due to the finite-time of the simulation. The latter effect can be controlled by monitoring how the broadening converges with longer and longer simulation times. Fig. 5.2-(b) and (c) show the power spectra using only the v_x and v_z components, respectively, confirming the in-plane and out-of-plane character of the E_G and A_{1G}, respectively.

5.4.3 Frequency vs temperature

In order to qualitatively describe the linear shift observed in the calculations, we first fitted a Lorentz function for each of the spectra to obtain the frequency peak value, and then used

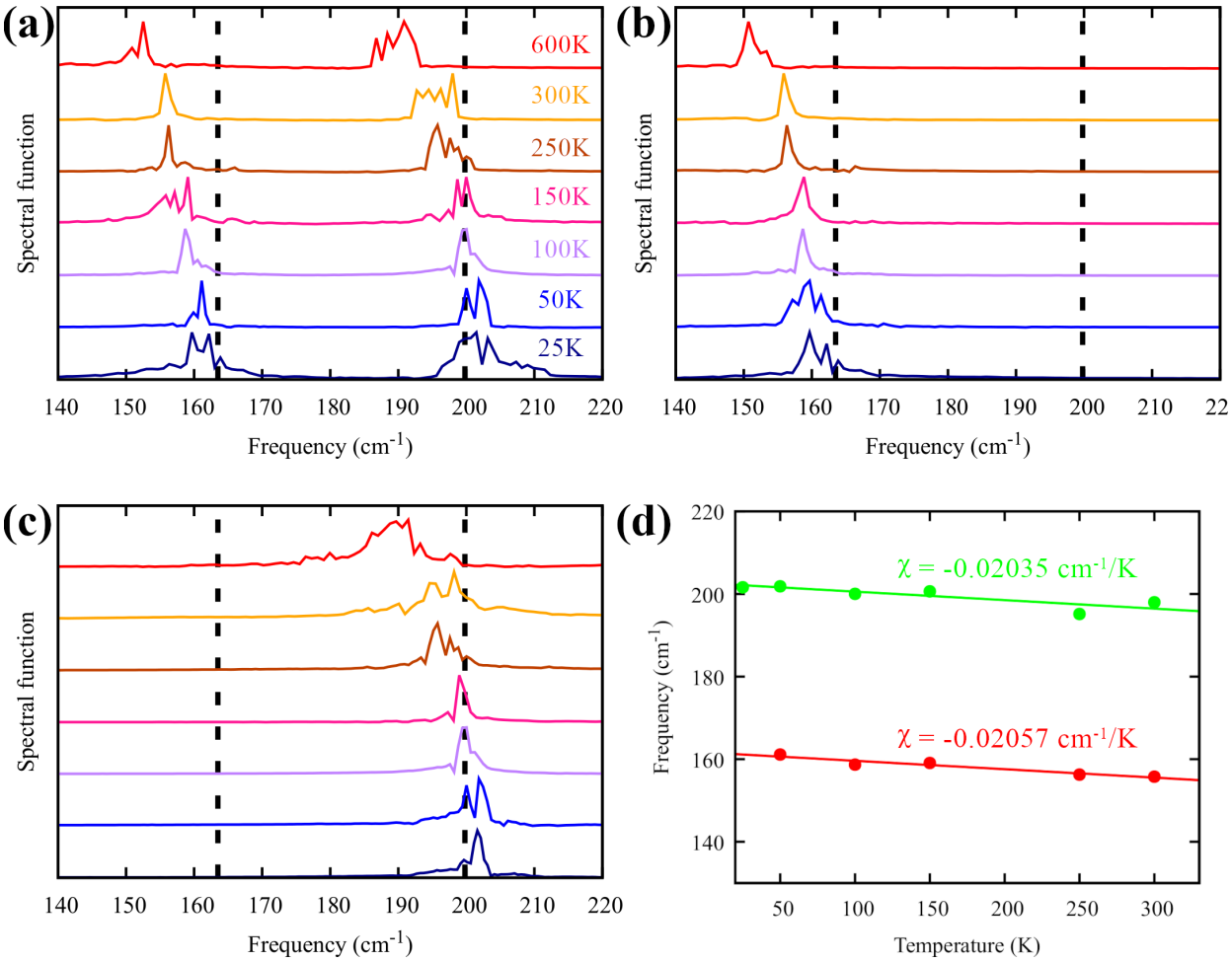

Figure 5.2 – Spectral function for temperatures ranging from 25 K to 600 K calculated using all the velocity components (a), only the x componente (b), and only the z component (c). Linear fit for the E_G and A_{1G} frequencies with temperature using all the velocity components.

this peak in a linear fit described by [132]:

$$\omega(T) = \omega_0 + \chi T \tag{5.3}$$

where ω_0 is the frequency at the origin (0 K) and χ is the first-order temperature coefficient. The fit is show in Fig.5.2-(d) together with the χ values of 0.02057cm^{-1}K^{-1} and 0.02035cm^{-1}K^{-1} for the E_G and A_{1G}, respectively. Firstly, we see that the values for both vibrational modes differ by only 2.2%. The χ found by fitting the experimental Raman spectra at higher temperatures for few-layer antimonene are -0.025 cm^{-1}K^{-1} and -0.027cm^{-1}K^{-1} for the E_G and A_{1G}, respectively, [124], differing by approximately 7% among each other and similar to the results presented here. Second, we notice that our χ values are higher than other two-dimensional nanomaterials such as graphene, MoS_2 and BP as one can see in the Table 1, indicating a stronger anharmonic response. Recent results in the literature have pointed out that the χ value in a number of layered materials

is associated with the van der Waals interlayer interaction [133, 134]. However, comparison between the present DFT results and experiment indicates that the major contribution to χ originates from intra-layer interactions.

Table 1 – The first-order temperature coefficient χ was calculated from the velocity autocorrelation function in this work and the experimental values obtained from the temperature-dependent Raman spectra for other 2D materials.

materials	Raman modes	χ ($cm^{-1}K^{-1}$)	Reference
Sb monolayer	A_{1G} E_G	-0.02057 -0.02035	This Work
Sb nanosheets	A_{1G} E_G	-0.027 -0.025	[124]
Sb_2O_3	$\alpha-^1$ A_g β-A_g	-0.025 -0.023	[135]
Monolayer graphene Bilayer graphene	G mode	-0.016 -0.015	[136]
MoS_2	A_{1g} $E_{2g}{}^1$	-0.012 -0.013	[137]
BP	A_{1g} A_{2g} B_{2g}	-0.010 –0.014 -0.013	[138]
SnSe	B_{3g} A_{g2} A_{g3}	-0.033 -0.037 -0.015	[139]

Another important aspect we can observe in Fig. 5.2-(a), (b), and (c) is that difference between the frequency peak for the lowest temperature (25 K) and the harmmonic calculation in the DFT-level (vertical black dashed line). As one can see, the phonon frequency for 25 K is still lower than harmonic approximation frequencies for the E_G and higher for the A_{1G}. The 2.0 cm^{-1} and 2.5 cm^{-1} difference for the E_G and A_{1G}, respectively, was expected in light of the fact that the molecular dynamics calculations allow non-linear behavior, including anharmonic effects. Similar results using analogous methodologies were also found in other two-dimensional nanomaterials such as BP monolayers [23] for temperatures as low as 4K with a discrepancy of about 1.5cm^{-1}, which reinforces that low temperature anharmonic effects can not be disregarded in these atomically thin group-V semiconductors.

5.5 Conclusion

We performed first-principles molecular dynamics calculations and used the velocity autocorrelation function to investigate the temperature effects on the phonon frequencies of the antimonene monolayer. We found the same trend of strong frequency blueshift observed for high-temperature antimonene few-layers obtained by Raman spectroscopy for both vibrational modes E_G and A_{1G}. Moreover, we found a linear dependence between the frequency and temperature for both vibrational modes, and our results for the linear temperature coefficient χ are close to the few-layers results, indicating that further investigation should be addressed in the role of the interlayer interaction on the χ value. We plan to submit a paper with these results in the next weeks.

6 Pressure induced electronic and structural transitions on two-dimensional nanomaterials

"Vinte e sete anos contrariando a estatística"

Capítulo 4 Versículo 3 - Racionais MC's

6.1 Introduction

By this point, we only discussed the electronic and structural properties of antimony-based (and arsenene) nanomaterials. However, we also investigated the pressure-induced transitions on another two-dimensional system: Graphene/hexagonal boron nitride (hBN) heterostructures. This project was started in my master's and finished during the first year of my PhD. The full list of experimental and theoretical collaborators for this project can be seen in [140].

Applying pressure in few-layers graphene is one of the most promising ways of obtaining 2D diamond-like structures. These nanodiamonds gather a lot of research interest due to the possibility of combining diamond's unique properties, such as hardness [141] and heat conduction [142], to the striking properties emerging from the reduced dimensionality. In the past thirteen years, several different structures have been theoretically proposed [143–146] in which stability is achieved by surface functionalization at both top and bottom surfaces - usually called "diamane" [143] for bilayers and "diamondoids" [147] for ticker layers. Martins et al. [17] proposed a different structure, called "diamondene", in which the chemical groups are covalently bounded only on the top surface while the bottom exhibits a periodic array of dangling bonds. Interestingly, these unpaired electrons and their periodic distribution give rise to two spin-polarized bands, making diamondene an excellent playground for spintronics [17, 145]. Martins et al. [17] also performed high-pressure Raman experiments on CVD graphene samples, monitoring the bond-stretching G mode's frequency with laser energy. The authors observed a sp^2-sp^3 transition for 5 and 7.5 GPa in bilayer chemical vapor deposition (CVD) graphene for two different samples when water was used as pressure transmitting medium (PTM). Intriguingly, these results were absent in pressured graphene monolayer or in bilayer graphene compressed in mineral oil up to 13 GPa - indicating a crucial role of the water in the reduction of critical pressure. Besides graphene, compression-induced transitions are also reported in the literature for other two-dimensional

material: hBN bilayers. Barboza et al. [18] observed insulating to conducting transitions on hBN bilayers compressed in an atomic force microscopy experiment. The authors proposed a structural transition (following the electronic one) in which the final structure, called *bonitrol*, is a 2D ferromagnetic diamond-like sp^3-hybridized BN system. On the other hand, the association of different 2D materials into van der Waals heterostructures has also been the subject of intensive research in the last few years [10, 148–151]. In this subject, graphene and hBN present as an excellent pair: Their weak electronic coupling between adjacent layers and the flat interlayer morphology on graphene/hBN heterostructures enable the investigation of exotic electronic properties such as fractal quantum Hall effects and superconductivity [8, 152]. Moreover, the role of pressure in the coupling magnitude between the layers as well as the resultant structural transition can lead to interesting phenomena as already discussed for the electronic transitions on a few layers of graphene [17] and hBN [18].

6.2 Objectives

We can summarize the main objectives of this chapter as:

- Use DFT to investigate the electronic and structural transitions induced by pressure on graphene/hBN heterostructures;
- Explain the behavior of the measured charge injection as a function of applied pressure using the simulated covalent structures in the different pressure ranges.

In the next section, we will briefly describe the experimental setup and the results that motivate this project.

6.3 Experimental details

6.3.1 Effective charging efficiency in compressed graphene/hBN heterostructures

To experimentally study the pressure effects on grahpene/hBN heterostructures, atomic force microscopy (AFM) and electrostatic force microscopy (EFM) were carried out. Fig. 6.1-(a) shows a topographic image of a typical trilayer graphene (TLG) + BN heterostructure sample, which was made by transferring a mechanically exfoliated trilayer graphene atop a mechanically exfoliated hBN flake (in greenish shades) that was deposited onto a conventional p-doped Si/SiO_X substrate (blue-violet shares) [153]. It is important to mention that since the crystallographic orientation of each h-BN flake is unknown, one should expect random values for the relative angle between graphene and hBN flakes after sample fabrication.

After the morphological characterization, a biased electrostatic force microscopy tip is employed to simultaneously apply forces and inject charges onto a given heterostructure

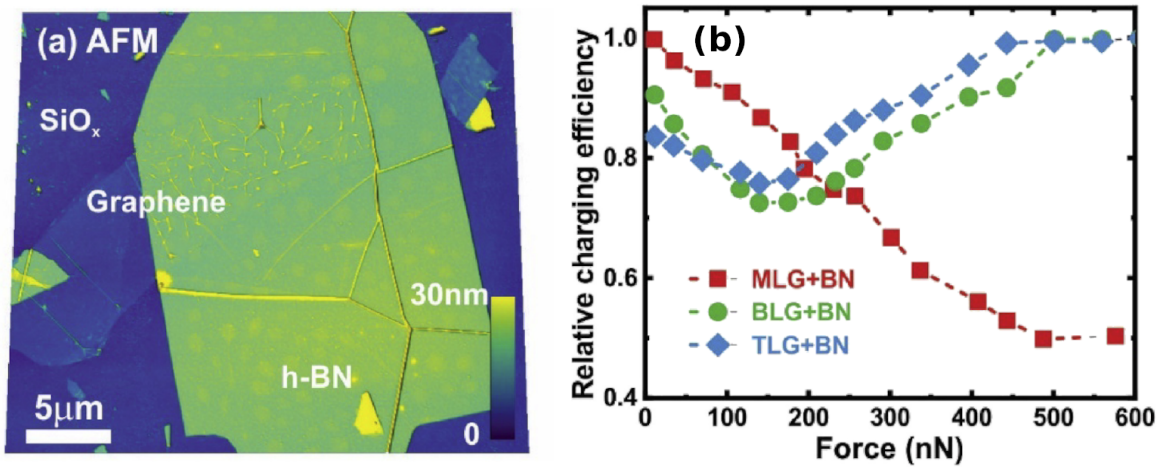

Figure 6.1 – Relative charging efficiency on graphene/hBN heterostructures. (a) Topographic AFM image showing a multilayered h-BN flake (in green-yellow shades) deposited onto a SiO_x surface (violet-blue). A trilayer graphene flake was also transferred onto the h-BN flake. (b) Graph of the relative charging efficiency as a function of the applied tip compression force for each graphene/hBN heterostructure (MLG + BN - red squares, BLG + BN - green circles and TLG + BN - blue diamonds) [140].

(monolayer graphene (MLG) + BN, bilayer graphene (BLG) + BN and trilayer graphene (TLG) + BN)). Subsequently, EFM imaging monitors the frequency shift $\Delta\omega$ of the cantilever frequency, which is proportional to the amount of injected charges q ($q \propto \Delta\omega^{1/2}$) [18, 145, 154]. In order to make the visualization easier among all the samples, we define a relative charging efficiency η ($\eta = (\Delta\omega/\Delta\omega_{max})^{1/2}$, where $\Delta\omega_{max}$ is the maximum frequency shift observed for a given sample). We summarize the results in Fig.6.1-(b) for relative charging efficiency as function of applied tip compression force for MLG + BN (red), BLG + BN (green), and TLG + BN (blue). From Fig. 6.1-(b), one can observe two distinct behaviors: (a) A monotonically decrease of the relative charging efficiency with the increase of the pressure for the monolayer case; (b) an initial decrease of the η until a force around 200 N, followed by an increase of the relative charging efficiency for both BLG and TLG cases. These results provide indications of pressure-induced conductor/non-conductor (MLG) and conductor/non-conductor/conductor (BLG and TLG) transitions. Therefore, the goal of this subproject is to use DFT to understand the final structural morphology of the graphene/hBN heterostructures and their electronic properties.

6.4 Computational details

First principles calculations were performed within the pseudopotential spin density functional theory formalism [29, 30] as implemented in the SIESTA program [39]. To expand the Kohn-Sham eigenfunctions a finite range double-ζ basis set plus polarization functions, the so-called DZP basis set, was used. Norm-conserving pseudopotentials [155] in the Kleinman-Bylander factorized form [156] and the generalized gradient approximation within the

Perdew-Burke-Ernzerhof (PBE) parametrization [35] for the exchange-correlation functional were employed. The grid for real space integrations was defined by a mesh cutoff of 400 Ry, and a force tolerance of 10 meV/Å in the atomic position optimizations was set. To sample the Brillouin zone, a k-grid cutoff of 120 Å was defined in all calculations. With these parameters, the convergence in total energy is of the order of 0.1 meV.

6.4.1 Pressure protocol

To obtain the sp^3 hybridized structures, we used a pressure protocol in which several calculations were performed varying the interlayer distance d (See Fig.6.2 for the graphene three-layer + hBN) and limiting the movement of specific atoms in the z direction. In this "hard wall" protocol, we started with a distance of d = 3.3 and performed 10 different calculations decreasing d_{CC} by 0.1 . The initial Carbon-Oxygen and Oxygen-Hydrogen distances was d_{CO} = 1.5 and d_{OH} = 1 in all the calculation. We imposed a movement constraint during the structural optimization,in which the z components of the top (bottom) atoms were made equal to zero if the forces in the +z (-z) direction were non zero and the z coordinates were outside the predefined range (the "hard wall range"). The value of pressure could be determined using the constrained forces in one of the surfaces at the end of the optimization process.'

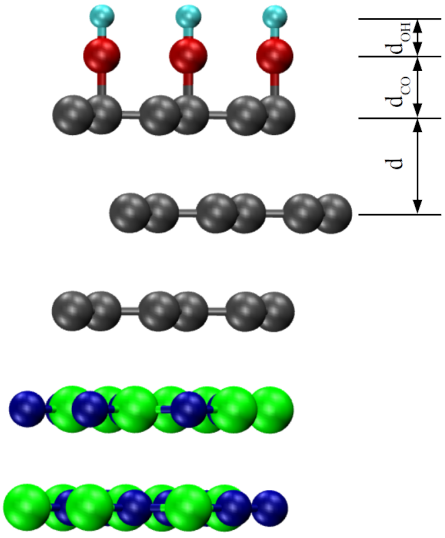

Figure 6.2 – Pressure protocol. Side view of the three-layer graphene + hBN showing the interlayer distance d, Carbon-Oxygen distance d_{CO} and Oxygen-Hydrogen distance d_{OH}. We performed several calculations varying the graphene interlayer distance ranging from 3.3 to 2.2 in 0.1 steps and restricting the movement in the z direction of the C atoms in the top layer and B/N atoms in the bottom layer. Carbon, Nitrogen, Boron, Oxygen, and Hydrogen atoms are represented by grey, blue, green, red, and ligh blue spheres, respectively.

6.5 Results and discussion

6.5.1 The AA and AB structures

We considered several different structures to represent the possible final morphologies of graphene/hBN heterostructures. For each, we performed an initial geometrical optimization setting the interlayer distance d within the covalent bond range and applied the hard wall protocol described in section 6.4.1. Then, we reached the final structures upon a second optimization, in which we let the system relax freely.

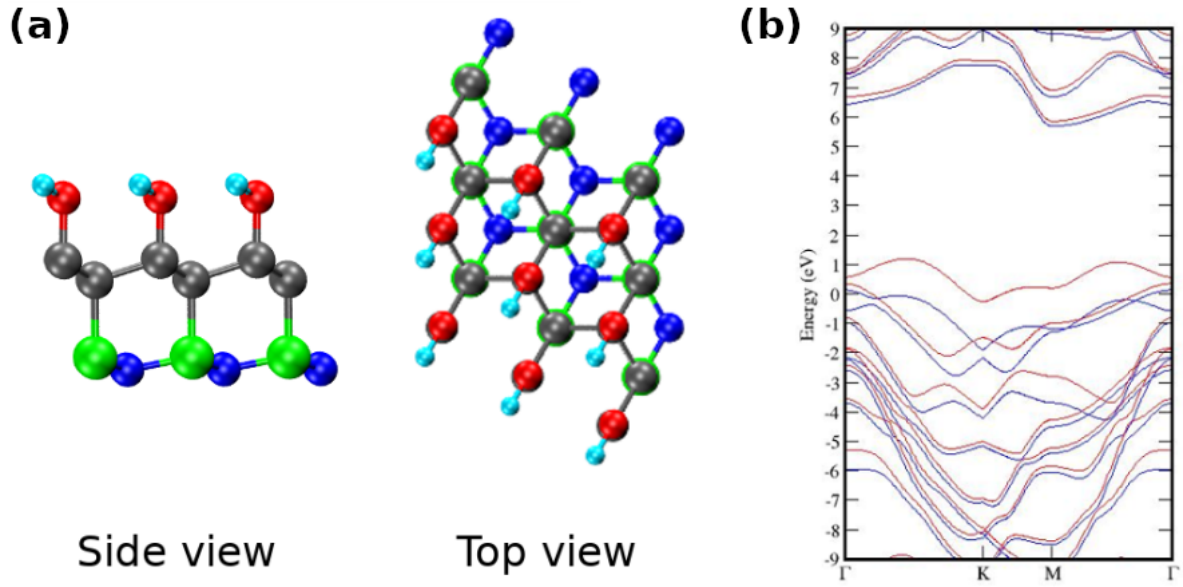

Figure 6.3 – The AB case. (a) Two views of the graphene/h-BN in the zero-angle case. (b) The corresponding band structure, with blue and red lines denoting the two spin components.

The first model that we considered was the perfect aligned graphene/hBN sheets, i.e., AA and AB stacking. Fig. 6.3-(a) shows two views of the final structure obtained for the AB stacking between the graphene and hBN sheets. As one can see, a complete sp^3 hybridization characterizes all the carbon and boron bonds, while the nitrogen atoms in the bottommost layer remain three-fold coordinated. The resulting ordered array of dangling bonds gives rise to dispersive bands crossing the Fermi level rendering the metallic character of the material as shown in Fig. 6.3-(b). We obtained similar results for the AA stacking, which do not agree with the observed decrease of charge injection efficiency upon pressure. Indeed, as should be expected, to realistically represent the deposition of one material on top of the other, our models should include a non-zero relative angle between graphene and hBN layers due to the random nature of the relative orientation of deposited layers in the experimental procedure. These structures will be detailed in the next section.

6.5.2 The moiré structures

Since the relative angle between the graphene/hBN flakes are unknown and the perfect aligned cases do not agree with the experimental data, we considered two different models that could capture these features: graphene/hBN heterostructures with two different twist angles, 21.79° and 13.17° for the monolayer case and 21.79° for bi- and three-layer. The reasoning behind these angles is two-fold: First, we need to impose periodic boundary conditions (PBC) in our calculations, therefore these twist angles generates a moiré pattern (large scale periodic interference patterns). Besides 21.79° and 13.17°, graphene and hBN systems also generates moiré patterns for other angles such as 9.43°, 7.34 °, 6.00°, and 5.09° [32]. This brings the second reason: The smallest angles have bigger moiré length, which means that the system would be big and computationally expensive to describe. The unit cells of the 21.79° and 13.17° MLG+BN have 42 and 114 atoms, respectively, and a moiré length of 6.64 for the 21.79° and 10.94 for the 13.17°. For the BGL and TGL + BN, we used only the 21.79° because the number of atoms increased quickly for these systems - the TGL+BN with 13.17° would have 228 atoms in the unit cell. Once established the models, we follow to the next subsection to describe the results for the BGL + BN case.

6.5.3 The twisted monolayer case

Applying the geometrical optimization described above, we observed the formation of stable covalent heterostructures in both cases, as shown in Fig. 6.5-(a). The structures are characterized by layer corrugation and a disordered pattern of interlayer bonds, which have a profound effect on the electronic structure. Fig. 6.5-(b) shows both band structures, where the localization induced by disorder leads to a spectral gap opening for both geometries. The 13.17° case have a small bandgap (0.13 eV) when compared with the 21.79° case (1.27 eV). However, the mobility band gap, the energy range between the highest occupied dispersive band and the lowest unoccupied dispersive band, is large (greater than 2eV) due to the flatness of all non-occupied bands within this energy range. Therefore, due to such predicted gap opening, the DFT calculations suggest a decrease in the charge injection efficiency as a function of pressure [145], in agreement with the experimental results in Fig. 6.1-(b).

As mentioned, it is not possible to perform calculations in random relative orientations because is necessary to impose PBC. Nevertheless, is expected that they would lead to even more disordered structures. Models for similar disordered systems, with tetrahedrally bonded atoms, show that their electronic structure may be defined by short-range order [157], which would still lead to semiconducting behaviors. Additional calculations performed for the heterostructures with 21.79° indicate that interlayer bonds are not formed for initial distances greater than 2.7 . In this low-pressure regime, the observed high charge efficiency is ascribed to the conductive properties of graphene. In the next subsection, we now turn our attention to the electronic and structural transitions for two- and three-layer graphene/hBN heterostructures.

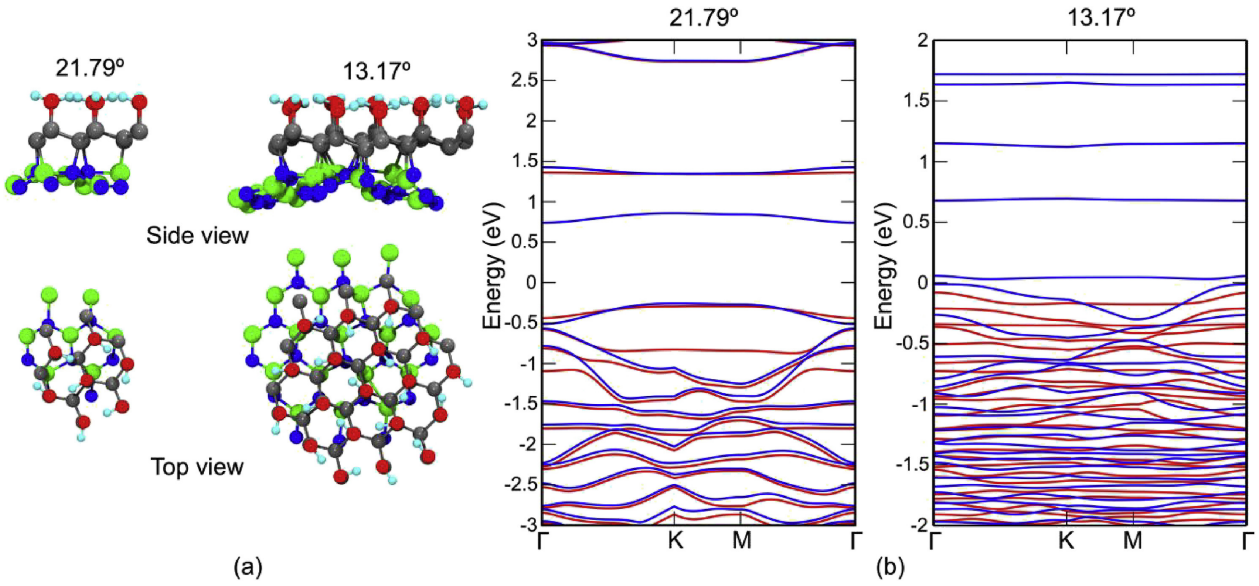

Figure 6.4 – Monolayer graphene/hBN (MLG + BN) heterostructures. (a) Side and top views of the optimized heterostructures for two relative angles: 21.79° (left) and 13.17° (right). (b)Band structures of the MLG þ BN heterostructures. Blue and red lines represent spin components and Fermi levels are set to zero. The bandgaps are 1.23 and 0.13 eV for 21.79° and 13.17° cases, respectively.

6.5.4 The twisted two- and three-layer cases

The same methodology was applied in the BLG and TLG + BN heterostructures and we found an even richer phenomenology that is summarized in Fig. 6.5 for the 21.79° structures. We can describe the hybridization process in three steps: (i) At a distance of 2.7 , the graphene layers bonds to each other, resulting in a final geometry identical to the already described *diamondol* structure [17, 145] (Fig. 6.5-(a) left, OH-functionalized 2D diamond layer) atop a hBN bilayer. The corresponding bandstructure (Fig. 6.5-(a) right) has a semiconductor behavior, roughly approximated by the superposition of the band structure of diamondol (a ferromagnetic semiconductor) and hBN bilayer (an insulator). (ii) The second step takes place at a smaller interlayer distance d = 2.3 , where the upper hBN layer covalently binds with the diamondol structure, forming a three-layer heterostructure atop of a hBN monolayer, as Fig. 6.5-(b) shows. The existence of a twist angle between graphene and hBN makes the system keeps the semiconducting behavior with an even bigger band gap (1.21 eV) as the right panel of Fig. 6.5-(b) shows. Interestingly, the system resembles the twisted monolayer case described in the previous section, with localized states dominating the low-energy region of the electronic spectrum. However, a striking difference exists among them: the larger rigidity of the upper diamond-like structure compared with the monolayer graphene case may lead to a less corrugated covalently bounded hBN layer in experimental conditions. A consequence is that a third structure may arise at an even higher-pressure regime. (iii) Indeed, for smaller distances in the 21.79 prototype system the rehybridization process also reaches the second (bottom) hBN layer, which has the same

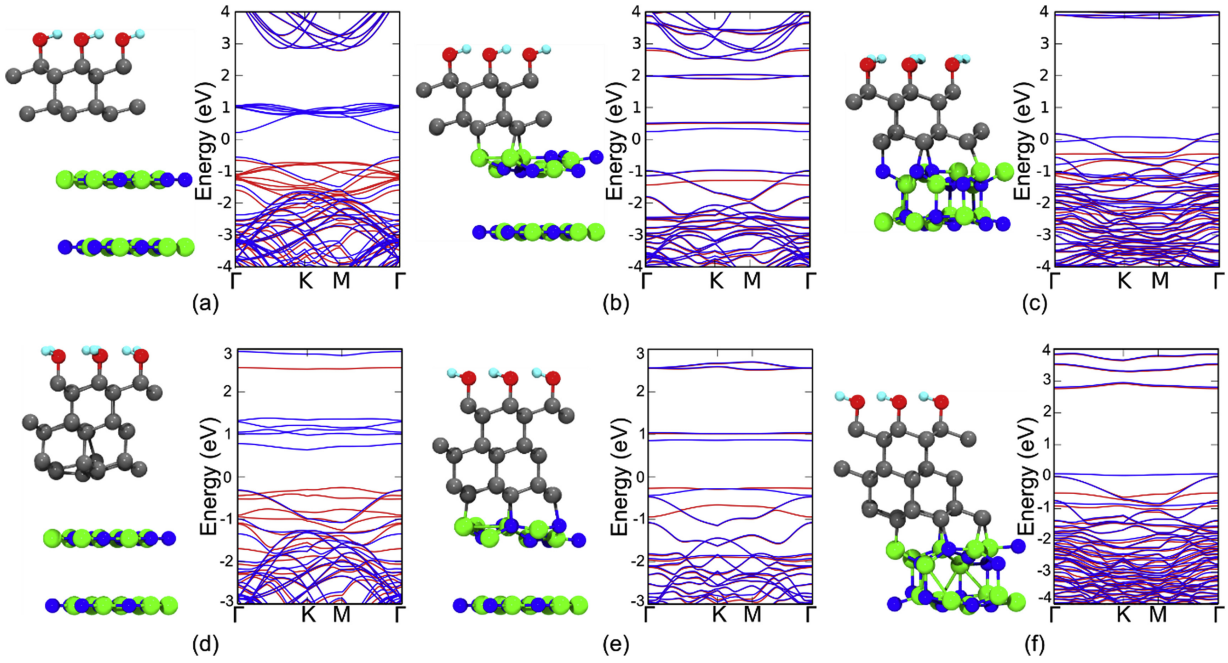

Figure 6.5 – BLG + BN and TLG + BN heterostructures. (a) BLG-BN heterostructure: optimized geometry (left) in the first rehybridization step, with a diamondol-like structure atop a h-BN bilayer, and the corresponding semiconducting (bandgap of 0.77 eV) band structure (right). (b) Converged structure and band structure in the second rehybridization step. The top h-BN layer covalently binds to the diamondol, opening up the bandgap to 1.21 eV. (c) Final heterostructure, completely rehybridized (left). Conducting states characterize its band structure, shown in the right panel. (d) TLG-BN heterostructure: Optimized geometry (left) in the first rehybridization step, with a three-layer diamondol-like structure atop a h-BN bilayer. The bandgap of 1.09 eV characterizes the band structure shown on the right. (e) Converged structure and band structure in the second rehybridization step. The top h-BN layer covalently binds to the three-layer diamondol opening up the bandgap to 1.29 eV. (f) Final heterostructure, completely rehybridized (left). As before, conducting states characterize the band structure, shown in the right panel. The Fermi level is set to zero in all plots. The relative angle between graphene and h-BN is 21.79°.

orientation as the top hBN (AB stacking). The resulting structure is shown in Fig. 6.5-(c), where a semiconductor to metal transition takes place - due to the alignment of the hBN layer, an array of dangling bonds in the bottom layer is responsible for the introduction of dispersive and conductive states [18]. The description is similar to the *bonitrol* case, a metallic 2D diamond-like structure formed by compressing hBN bilayer which is also characterized by the presence of defective and dispersive bands [18]. The formation of this structure in the experimental setup would trigger an increase in the charging efficiency in the high-pressure regime, as observed in Fig. 6.1-(b).

As for the TLG + BN case, we observed the same trends discussed for the bilayer case for both structural and electronic transitions as shown in Fig. 6.5-(d) to -(f): (i) An initial transition

leads to the formation of a three-layer diamondol with semiconducting behavior; (ii) Decreasing the interlayer distance, i.e., increasing the pressure, the upper hBN layer covalently binds with the diamondol-like structure, forming a heterostructure with a bigger band gap; (iii) Lastly, both hBN layers form sp^3 bonds, resulting in the final rehybridized structure with conductor behavior. The BLG and TLG + BN cases reinforce the argument that thicker sp^3 diamond-like systems favor more ordered structures since the corrugation of the bottommost hBN layer is 14% larger in the MLG + BN case.

Overall, the DFT calculations indicate that, as pressure increases in the AFM/EFM experiments, a first transition - the formation of two semiconducting structures - initially causes a decrease in the charge injection efficiency, while a second transition - the formation of the conducting structure - would increase the charge injection efficiency.

6.6 Conclusion

Altogether, experimental evidence of electronic transition in graphene and hBN heterostructures was reported by Prof. Ana Paula Barboza (UFOP) and Prof. Bernardo Neves (UFMG) experimental group (See [140] for the full list of collaborators), in which AFM/EFM experiments show an initial decrease of the charging efficiency for mono-, bi-, and three-layer graphene atop an hBN flake suggesting a transition to a semiconductor system. The presented DFT calculations for twisted heterostructures predict the formation of covalent bonds between the graphene and topmost hBN layer (and the diamondol with the topmost hBN for bi- and three-layers graphene), which present semiconductor behavior - in qualitative agreement with experiments. In the higher pressure regime, an inversion happens and the charging efficiency increases. In this regime, the calculations show that the bottommost hBN layer binds with the graphene/hBN covalent structure giving rise to dispersive bands crossing the Fermi level for both bi- and three-layer graphene. The formation of these metallic structures agrees with the increasing charging efficiency reported in the AFM/EFM experiment. All these results were published in Carbon 155 (2019): 108-113., where I shared the first authorship with Prof. Ana Paula Barboza (UFOP).

7 Final conclusion and perspectives

"Chegar aqui de onde eu vim
É desafiar a lei da gravidade
Pobre morre ou é preso, nessa
idade"

Junho de 94 - Djonga

In this thesis, we performed first principle calculations to investigate the electronic and structural properties of novel two-dimensional nanomaterials such as antimonene, arsenene, and graphene/hBN heterostructures. We can summarize the general idea of each project with four questions. The first question we answered was "How the structural and electronic properties of antimonene few layers would change if we functionalize it with different chemical groups?" Interestingly, we found an oxidation-induced process of 2D to quasi-1D transitions for up to eight antimonene layers. The final quasi-1D structures are stacked nanoribbons with widths controlled by the number of initial layers and precisely ordered edges. Controlling the edge morphology, oxide agent, and width of the nanoribbon can lead to interesting applications in nanoelectronics.

As for the second question, we asked "How would the flat band mechanism behave in other twisted nanomaterials, such as antimonene bilayers?" We found that due to the relatively stronger interlayer interaction on antimonene, flat bands can emerge for twist angles as high as 9.43°as a consequence of atomic displacements along the different stacking patterns on the moiré superlattice. These results put antimonene as a new candidate for exotic physics investigation without need of the small fine tune of the twist angles.

For the third question, we were interested in the anharmonic effects on antimonene, so we asked "How the low temperature affects the vibrational modes of the antimonene monolayer?" To clarify that, we performed ab initio molecular dynamics calculations for several temperatures below 300K and calculated the power spectra from the velocity autocorrelation function. We found a linear frequency shift for the low-temperature regime, in the same order of magnitude as other two-dimensional nanomaterials. Our results complement the understanding of the vibrational properties of antimonene over a wide range of temperatures, which is important for nanodevice applications and development.

Lastly, we focused on a different two-dimensional system to answer the following question: "Why the charge efficiency decreases monotonically for a graphene/hBN heterostructure under pressure, and why does it increase again for two and three graphene layers/hBN heterostructures at the high-pressure limit?" We performed several calculations using twisted graphene/hBN structures and found that due to the covalent bonding of the graphene/hBN layer,

a new diamond-like structure would be formed with semiconductor electronic behavior. The two and three graphene cases go through a similar process: First, the graphene layer forms a diamondene structure (opening the bandgap) at the top of the hBN flake; then the diamond-like structure binds to the first hBN layer increasing the bandgap; Finally, the second hBN layer binds with the graphene/hBN diamond-like structure, making the system a conductor again. The formation of covalent structures during the pressuring process explains the charge efficiency behavior observed in the atomic force microscopy experiment with a remarkable agreement.

As for future perspective, we can list a few interesting points: (i) Investigate the spin-orbit coupling on heavier twisted two-dimensional nanomaterials such as bismuthene; (ii) Extend the oxidation-induced transition to other novel nanomaterials; (iii) Study the magnetic and correlation effects on narrow gap two-dimensional correlated antimony based semiconductors; (iv) investigate point defects (such as Nitrogen-Vacancy center) in the two-dimensional diamond-like structures.

Bibliography

[1] Novoselov, Kostya S, Andre K Geim, Sergei V Morozov, De eng Jiang, Yanshui Zhang, Sergey V Dubonos, Irina V Grigorieva, and Alexandr A Firsov: *Electric field effect in atomically thin carbon films*. science, 306(5696):666–669, 2004.

[2] Tiwari, Santosh K, Vijay Kumar, Andrzej Huczko, R Oraon, A De Adhikari, and GC Nayak: *Magical allotropes of carbon: prospects and applications*. Critical Reviews in Solid State and Materials Sciences, 41(4):257–317, 2016.

[3] Yang, Yuxing, Ruili Liu, Jiayang Wu, Xinhong Jiang, Pan Cao, Xiaofeng Hu, Ting Pan, Ciyuan Qiu, Junyi Yang, Yinglin Song, *et al.*: *Bottom-up fabrication of graphene on silicon/silica substrate via a facile soft-hard template approach*. Scientific reports, 5(1):1–7, 2015.

[4] Tiwari, Santosh K, Raghvendra Kumar Mishra, Sung Kyu Ha, and Andrzej Huczko: *Evolution of graphene oxide and graphene: from imagination to industrialization*. ChemNanoMat, 4(7):598–620, 2018.

[5] Liao, Lei, Hailin Peng, and Zhongfan Liu: *Chemistry makes graphene beyond graphene*. Journal of the American chemical society, 136(35):12194–12200, 2014.

[6] Hughes, Zak E and Tiffany R Walsh: *Computational chemistry for graphene-based energy applications: progress and challenges*. Nanoscale, 7(16):6883–6908, 2015.

[7] Allen, Matthew J, Vincent C Tung, and Richard B Kaner: *Honeycomb carbon: a review of graphene*. Chemical reviews, 110(1):132–145, 2010.

[8] Cao, Yuan, Valla Fatemi, Shiang Fang, Kenji Watanabe, Takashi Taniguchi, Efthimios Kaxiras, and Pablo Jarillo-Herrero: *Unconventional superconductivity in magic-angle graphene superlattices*. Nature, 556(7699):43–50, 2018.

[9] Cao, Yuan, Valla Fatemi, Ahmet Demir, Shiang Fang, Spencer L Tomarken, Jason Y Luo, Javier D Sanchez-Yamagishi, Kenji Watanabe, Takashi Taniguchi, Efthimios Kaxiras, *et al.*: *Correlated insulator behaviour at half-filling in magic-angle graphene superlattices*. Nature, 556(7699):80–84, 2018.

[10] Geim, Andre K and Irina V Grigorieva: *Van der Waals heterostructures*. Nature, 499(7459):419–425, 2013.

[11] Behura, Sanjay K, Alexis Miranda, Sasmita Nayak, Kayleigh Johnson, Priyanka Das, and Nihar R Pradhan: *Moiré physics in twisted van der Waals heterostructures of 2D materials*. Emergent Materials, 4(4):813–826, 2021.

[12] Yuan, Long, Biyuan Zheng, Jens Kunstmann, Thomas Brumme, Agnieszka Beata Kuc, Chao Ma, Shibin Deng, Daria Blach, Anlian Pan, and Libai Huang: *Twist-angle-dependent interlayer exciton diffusion in WS2–WSe2 heterobilayers*. Nature materials, 19(6):617–623, 2020.

[13] Tran, Kha, Junho Choi, and Akshay Singh: *Moiré and beyond in transition metal dichalcogenide twisted bilayers*. 2D Materials, 8(2):022002, 2020.

[14] Hu, Guangwei, Qingdong Ou, Guangyuan Si, Yingjie Wu, Jing Wu, Zhigao Dai, Alex Krasnok, Yarden Mazor, Qing Zhang, Qiaoliang Bao, *et al.*: *Topological polaritons and photonic magic angles in twisted α-MoO3 bilayers*. Nature, 582(7811):209–213, 2020.

[15] Chiodini, Stefano, James Kerfoot, Giacomo Venturi, Sandro Mignuzzi, Evgeny M Alexeev, Bárbara Teixeira Rosa, Sefaattin Tongay, Takashi Taniguchi, Kenji Watanabe, Andrea C Ferrari, *et al.*: *Moiré Modulation of Van Der Waals Potential in Twisted Hexagonal Boron Nitride*. ACS nano, 2022.

[16] Chen, Weijong, Zeyuan Sun, Zhongjie Wang, Lehua Gu, Xiaodong Xu, Shiwei Wu, and Chunlei Gao: *Direct observation of van der Waals stacking–dependent interlayer magnetism*. Science, 366(6468):983–987, 2019.

[17] Martins, Luiz Gustavo Pimenta, Matheus JS Matos, Alexandre R Paschoal, Paulo TC Freire, Nadia F Andrade, Acrísio L Aguiar, Jing Kong, Bernardo RA Neves, Alan B de Oliveira, Mário SC Mazzoni, *et al.*: *Raman evidence for pressure-induced formation of diamondene*. Nature communications, 8(1):1–9, 2017.

[18] Barboza, Ana PM, Matheus JS Matos, Helio Chacham, Ronaldo JC Batista, Alan B de Oliveira, Mario SC Mazzoni, and Bernardo RA Neves: *Compression-induced modification of boron nitride layers: a conductive two-dimensional BN compound*. Acs Nano, 12(6):5866–5872, 2018.

[19] Liang, Theresa, Constanze N Neumann, and Tobias Ritter: *Introduction of fluorine and fluorine-containing functional groups*. Angewandte Chemie International Edition, 52(32):8214–8264, 2013.

[20] Elias, Daniel C, Rahul Raveendran Nair, TMG Mohiuddin, SV Morozov, P Blake, MP Halsall, Andrea Carlo Ferrari, DW Boukhvalov, MI Katsnelson, AK Geim, *et al.*: *Control of graphene's properties by reversible hydrogenation: evidence for graphane*. Science, 323(5914):610–613, 2009.

[21] Park, Sungjin and Rodney S Ruoff: *Chemical methods for the production of graphenes*. Nature nanotechnology, 4(4):217–224, 2009.

[22] Peng, Xihong and Qun Wei: *Chemical scissors cut phosphorene nanostructures*. Materials Research Express, 1(4):045041, 2014.

[23] Tristant, Damien, Andrew Cupo, Xi Ling, and Vincent Meunier: *Phonon anharmonicity in few-layer black phosphorus*. ACS nano, 13(9):10456–10468, 2019.

[24] Lan, Tian, Xiaoli Tang, and Brent Fultz: *Phonon anharmonicity of rutile TiO 2 studied by Raman spectrometry and molecular dynamics simulations*. Physical Review B, 85(9):094305, 2012.

[25] Wang, CZ, CT Chan, and KM Ho: *Tight-binding molecular-dynamics study of phonon anharmonic effects in silicon and diamond*. Physical Review B, 42(17):11276, 1990.

[26] Cupo, Andrew, Damien Tristant, Kyle Rego, and Vincent Meunier: *Theoretical analysis of spectral lineshapes from molecular dynamics*. npj Computational Materials, 5(1):1–12, 2019.

[27] Szabo, Attila and Neil S Ostlund: *Modern quantum chemistry: introduction to advanced electronic structure theory*. Courier Corporation, 2012.

[28] Martin, Richard M: *Electronic structure: basic theory and practical methods*. Cambridge university press, 2020.

[29] Hohenberg, Pierre and Walter Kohn: *Inhomogeneous electron gas*. Physical review, 136(3B):B864, 1964.

[30] Kohn, Walter and Lu Jeu Sham: *Self-consistent equations including exchange and correlation effects*. Physical review, 140(4A):A1133, 1965.

[31] Capelle, Klaus: *A bird's-eye view of density-functional theory*. Brazilian journal of physics, 36:1318–1343, 2006.

[32] Matos, Matheus Josué Souza: *ESTUDO TEÓRICO DAS PROPRIEDADES DE NITRETO DE BORO HEXAGONAL E GRAFENO: RESPOSTA DIELÉTRICA, EMPILHAMENTO E ESTRUTURA ELETRÔNICA*. PhD thesis, Tese apresentada para a Universidade Federal de Minas Gerais como requisito . . . , 2014.

[33] Reis Souza, Alan Custodio dos: *Transformações estruturais e eletrônicas em nanomateriais bidimensionais sob pressão*. 2018.

[34] Ceperley, David M and Berni J Alder: *Ground state of the electron gas by a stochastic method*. Physical review letters, 45(7):566, 1980.

[35] Perdew, John P, Kieron Burke, and Matthias Ernzerhof: *Generalized gradient approximation made simple*. Physical review letters, 77(18):3865, 1996.

[36] Verlet, Loup: *Computer"experiments"on classical fluids. I. Thermodynamical properties of Lennard-Jones molecules*. Physical review, 159(1):98, 1967.

[37] Nosé, Shuichi: *A unified formulation of the constant temperature molecular dynamics methods*. The Journal of chemical physics, 81(1):511–519, 1984.

[38] Hamann, DR, M Schlüter, and C Chiang: *Norm-conserving pseudopotentials*. Physical Review Letters, 43(20):1494, 1979.

[39] Soler, José M, Emilio Artacho, Julian D Gale, Alberto García, Javier Junquera, Pablo Ordejón, and Daniel Sánchez-Portal: *The SIESTA method for ab initio order-N materials simulation*. Journal of Physics: Condensed Matter, 14(11):2745, 2002.

[40] Ashcroft, Neil W and N David Mermin: *Solid State Physics, College edn*. Thomson Learning Inc, 1976.

[41] Hafner, Jürgen: *Ab-initio simulations of materials using VASP: Density-functional theory and beyond*. Journal of computational chemistry, 29(13):2044–2078, 2008.

[42] Car, Richard and Mark Parrinello: *Unified approach for molecular dynamics and density-functional theory*. Physical review letters, 55(22):2471, 1985.

[43] Girolami, Gregory S: *Origin of the terms pnictogen and pnictide*. Journal of chemical education, 86(10):1200, 2009.

[44] Zhang, Shengli, Zhong Yan, Yafei Li, Zhongfang Chen, and Haibo Zeng: *Atomically thin arsenene and antimonene: semimetal–semiconductor and indirect–direct band-gap transitions*. Angewandte Chemie, 127(10):3155–3158, 2015.

[45] Wang, Gaoxue, Ravindra Pandey, and Shashi P Karna: *Atomically thin group V elemental films: theoretical investigations of antimonene allotropes*. ACS applied materials & interfaces, 7(21):11490–11496, 2015.

[46] Bian, Guang, Thomas Miller, and T C Chiang: *Passage from spin-polarized surface states to unpolarized quantum well states in topologically nontrivial Sb films*. Physical Review Letters, 107(3):036802, 2011.

[47] Kim, Sung Hwan, Kyung Hwan Jin, Joonbum Park, Jun Sung Kim, Seung Hoon Jhi, and Han Woong Yeom: *Topological phase transition and quantum spin Hall edge states of antimony few layers*. Scientific reports, 6(1):1–7, 2016.

[48] Zhang, PengFei, Zheng Liu, Wenhui Duan, Feng Liu, and Jian Wu: *Topological and electronic transitions in a Sb (111) nanofilm: The interplay between quantum confinement and surface effect*. Physical Review B, 85(20):201410, 2012.

[49] Pizzi, Giovanni, Marco Gibertini, Elias Dib, Nicola Marzari, Giuseppe Iannaccone, and Gianluca Fiori: *Performance of arsenene and antimonene double-gate MOSFETs from first principles*. Nature communications, 7(1):1–9, 2016.

[50] Zhao, Mingwen, Xiaoming Zhang, and Linyang Li: *Strain-driven band inversion and topological aspects in Antimonene*. Scientific reports, 5(1):1–7, 2015.

[51] Tian, Weifeng, Shengli Zhang, Chengxue Huo, Daming Zhu, Qingwei Li, Lei Wang, Xiaochuan Ren, Lei Xie, Shiying Guo, Paul K Chu, *et al.*: *Few-layer antimonene: anisotropic expansion and reversible crystalline-phase evolution enable large-capacity and long-life Na-ion batteries*. ACS nano, 12(2):1887–1893, 2018.

[52] Cui, Chunyu, Jiantie Xu, Yiqiong Zhang, Zengxi Wei, Minglei Mao, Xin Lian, Shuangyin Wang, Chongyin Yang, Xiulin Fan, Jianmin Ma, *et al.*: *Antimony nanorod encapsulated in cross-linked carbon for high-performance sodium ion battery anodes*. Nano letters, 19(1):538–544, 2018.

[53] Chen, Bochao, Ming Liang, Qingzhao Wu, Shan Zhu, Naiqin Zhao, and Chunnian He: *Recent Developments of Antimony-Based Anodes for Sodium-and Potassium-Ion Batteries*. Transactions of Tianjin University, pages 1–27, 2021.

[54] Gusmão, Rui, Zdeněk Sofer, Daniel Bouša, and Martin Pumera: *Pnictogen (As, Sb, Bi) nanosheets for electrochemical applications are produced by shear exfoliation using kitchen blenders*. Angewandte Chemie, 129(46):14609–14614, 2017.

[55] Yu, Xiang, Weiyuan Liang, Chenyang Xing, Keqiang Chen, Jianming Chen, Weichun Huang, Ni Xie, Meng Qiu, Xiaobing Yan, Zhongjian Xie, *et al.*: *Emerging 2D pnictogens for catalytic applications: status and challenges*. Journal of Materials Chemistry A, 8(26):12887–12927, 2020.

[56] Wang, Xin, Junjie He, Benqing Zhou, Youming Zhang, Jiatao Wu, Rui Hu, Liwei Liu, Jun Song, and Junle Qu: *Bandgap-tunable preparation of smooth and large two-dimensional antimonene*. Angewandte Chemie, 130(28):8804–8809, 2018.

[57] Martínez-Periñán, Emiliano, Michael P Down, Carlos Gibaja, Encarnación Lorenzo, Félix Zamora, and Craig E Banks: *Antimonene: a novel 2D nanomaterial for supercapacitor applications*. Advanced Energy Materials, 8(11):1702606, 2018.

[58] Chen, Kai Xuan, Shu Shen Lyu, Xiao Ming Wang, Yuan Xiang Fu, Yi Heng, and Dong Chuan Mo: *Excellent thermoelectric performance predicted in two-dimensional buckled antimonene: a first-principles study*. The Journal of Physical Chemistry C, 121(24):13035–13042, 2017.

[59] Chang, Tay Rong, Qiangsheng Lu, Xiaoxiong Wang, Hsin Lin, T Miller, Tai Chang Chiang, and Guang Bian: *Band topology of bismuth quantum films*. Crystals, 9(10):510, 2019.

[60] Liu, Yi and Roland E Allen: *Electronic structure of the semimetals Bi and Sb*. Physical Review B, 52(3):1566, 1995.

[61] Aktürk, O Üzengi, V Ongun Özçelik, and S Ciraci: *Single-layer crystalline phases of antimony: Antimonenes*. Physical review B, 91(23):235446, 2015.

[62] Fu, Liang and Charles L Kane: *Topological insulators with inversion symmetry*. Physical Review B, 76(4):045302, 2007.

[63] Ares, Pablo, Fernando Aguilar-Galindo, David Rodríguez-San-Miguel, Diego A Aldave, Sergio Díaz-Tendero, Manuel Alcamí, Fernando Martín, Julio Gómez-Herrero, and Félix Zamora: *Mechanical isolation of highly stable antimonene under ambient conditions*. Advanced Materials, 28(30):6332–6336, 2016.

[64] Zhang, Shengli, Shiying Guo, Zhongfang Chen, Yeliang Wang, Hongjun Gao, Julio Gómez-Herrero, Pablo Ares, Félix Zamora, Zhen Zhu, and Haibo Zeng: *Recent progress in 2D group-VA semiconductors: from theory to experiment*. Chemical Society Reviews, 47(3):982–1021, 2018.

[65] Ji, Jianping, Xiufeng Song, Jizi Liu, Zhong Yan, Chengxue Huo, Shengli Zhang, Meng Su, Lei Liao, Wenhui Wang, Zhenhua Ni, *et al.*: *Two-dimensional antimonene single crystals grown by van der Waals epitaxy*. Nature communications, 7(1):1–9, 2016.

[66] Gibaja, Carlos, David Rodriguez-San-Miguel, Pablo Ares, Julio Gómez-Herrero, Maria Varela, Roland Gillen, Janina Maultzsch, Frank Hauke, Andreas Hirsch, Gonzalo Abellán, and Félix Zamora: *Few-Layer Antimonene by Liquid-Phase Exfoliation*. Angewandte Chemie International Edition, 55(46):14345–14349, 2016. `https://onlinelibrary.wiley.com/doi/abs/10.1002/anie.201605298`.

[67] Lin, Wanzhen, Yaping Lian, Guang Zeng, Yanyan Chen, Zhenhai Wen, and Huanghao Yang: *A fast synthetic strategy for high-quality atomically thin antimonene with ultrahigh sonication power*. Nano Research, 11(11):5968–5977, 2018.

[68] Hoat, DM, Duy Khanh Nguyen, Asadollah Bafekry, Vo Van On, Bakhtiar Ul Haq, JF Rivas-Silva, and Gregorio H Cocoletzi: *Strain-driven modulation of the electronic, optical and thermoelectric properties of β-antimonene monolayer: A hybrid functional study*. Materials Science in Semiconductor Processing, 131:105878, 2021.

[69] Zhang, Shengli, Wenhan Zhou, Yandong Ma, Jianping Ji, Bo Cai, Shengyuan A Yang, Zhen Zhu, Zhongfang Chen, and Haibo Zeng: *Antimonene oxides: emerging tunable direct*

bandgap semiconductor and novel topological insulator. Nano letters, 17(6):3434–3440, 2017.

[70] Gibaja, Carlos, Mhamed Assebban, Iñigo Torres, Michael Fickert, Roger Sanchis-Gual, Isaac Brotons, Wendel S Paz, Juan José Palacios, Enrique G Michel, Gonzalo Abellán, *et al.*: *Liquid phase exfoliation of antimonene: systematic optimization, characterization and electrocatalytic properties*. Journal of Materials Chemistry A, 7(39):22475–22486, 2019.

[71] Wu, Xu, Yan Shao, Hang Liu, Zili Feng, Ye Liang Wang, Jia Tao Sun, Chen Liu, Jia Ou Wang, Zhong Liu Liu, Shi Yu Zhu, *et al.*: *Epitaxial growth and air-stability of monolayer antimonene on PdTe2*. Advanced Materials, 29(11):1605407, 2017.

[72] Niu, Tianchao, Qingling Meng, Dechun Zhou, Nan Si, Shuwei Zhai, Xiamin Hao, Miao Zhou, and Harald Fuchs: *Large-scale synthesis of strain-tunable semiconducting antimonene on copper oxide*. Advanced Materials, 32(4):1906873, 2020.

[73] Shao, Yan, Zhong Liu Liu, Cai Cheng, Xu Wu, Hang Liu, Chen Liu, Jia Ou Wang, Shi Yu Zhu, Yu Qi Wang, Dong Xia Shi, *et al.*: *Epitaxial growth of flat antimonene monolayer: A new honeycomb analogue of graphene*. Nano letters, 18(3):2133–2139, 2018.

[74] Sun, Shuo, Tong Yang, Yong Zheng Luo, Jian Gou, Yuli Huang, Chengding Gu, Zhirui Ma, Xu Lian, Sisheng Duan, Andrew TS Wee, *et al.*: *Realization of a buckled antimonene monolayer on Ag (111) via surface engineering*. The Journal of Physical Chemistry Letters, 11(21):8976–8982, 2020.

[75] Son, Young Woo, Marvin L Cohen, and Steven G Louie: *Half-metallic graphene nanoribbons*. Nature, 444(7117):347–349, 2006.

[76] Cai, Jinming, Pascal Ruffieux, Rached Jaafar, Marco Bieri, Thomas Braun, Stephan Blankenburg, Matthias Muoth, Ari P Seitsonen, Moussa Saleh, Xinliang Feng, *et al.*: *Atomically precise bottom-up fabrication of graphene nanoribbons*. Nature, 466(7305):470–473, 2010.

[77] Li, Xiaolin, Xinran Wang, Li Zhang, Sangwon Lee, and Hongjie Dai: *Chemically derived, ultrasmooth graphene nanoribbon semiconductors*. science, 319(5867):1229–1232, 2008.

[78] Wang, Yanli and Yi Ding: *Electronic structure and carrier mobilities of arsenene and antimonene nanoribbons: a first-principle study*. Nanoscale research letters, 10(1):1–10, 2015.

[79] Ares, Pablo, Juan José Palacios, Gonzalo Abellán, Julio Gómez-Herrero, and Félix Zamora: *Recent progress on antimonene: a new bidimensional material*. Advanced Materials, 30(2):1703771, 2018.

[80] Zhang, Shengli and Z Yan: *Li Yet al (2015) Atomically thin arsenene and antimonene: semimetal-semiconductor and indirect-direct band-gap transitions*. Angew Chem Int Ed, 54:3112–3115.

[81] Chuang, Feng Chuan, Chia Hsiu Hsu, Chia Yu Chen, Zhi Quan Huang, Vidvuds Ozolins, Hsin Lin, and Arun Bansil: *Tunable topological electronic structures in Sb (111) bilayers: A first-principles study*. Applied Physics Letters, 102(2):022424, 2013.

[82] Tsai, Hsu Sheng, Chia Wei Chen, Ching Hung Hsiao, Hao Ouyang, and Jenq Horng Liang: *The advent of multilayer antimonene nanoribbons with room temperature orange light emission*. Chemical Communications, 52(54):8409–8412, 2016.

[83] Zhang, Shengli, Meiqiu Xie, Fengyu Li, Zhong Yan, Yafei Li, Erjun Kan, Wei Liu, Zhongfang Chen, and Haibo Zeng: *Semiconducting group 15 monolayers: a broad range of band gaps and high carrier mobilities*. Angewandte Chemie, 128(5):1698–1701, 2016.

[84] Guo, Shiying, Yupeng Zhang, Yanqi Ge, Shengli Zhang, Haibo Zeng, and Han Zhang: *2D V-V binary materials: status and challenges*. Advanced Materials, 31(39):1902352, 2019.

[85] Lee, Kyuho, Éamonn D Murray, Lingzhu Kong, Bengt I Lundqvist, and David C Langreth: *Higher-accuracy van der Waals density functional*. Physical Review B, 82(8):081101, 2010.

[86] Rydberg, Henrik, Max Dion, Niclas Jacobson, Elsebeth Schröder, Per Hyldgaard, SI Simak, David C Langreth, and Bengt I Lundqvist: *Van der Waals density functional for layered structures*. Physical review letters, 91(12):126402, 2003.

[87] Li, YH, PF Yuan, ZQ Fan, and ZH Zhang: *Electronic properties and carrier mobility for penta-graphene nanoribbons with nonmetallic-atom-terminations*. Organic Electronics, 59:306–313, 2018.

[88] Zhang, Haijun, Yandong Ma, and Zhongfang Chen: *Quantum spin hall insulators in strain-modified arsenene*. Nanoscale, 7(45):19152–19159, 2015.

[89] Wang, Ya ping, Chang wen Zhang, Wei xiao Ji, Run wu Zhang, Ping Li, Pei ji Wang, Miao juan Ren, Xin lian Chen, and Min Yuan: *Tunable quantum spin Hall effect via strain in two-dimensional arsenene monolayer*. Journal of Physics D: Applied Physics, 49(5):055305, 2016.

[90] Kou, Liangzhi, Yandong Ma, Xin Tan, Thomas Frauenheim, Aijun Du, and Sean Smith: *Structural and Electronic Properties of Layered Arsenic and Antimony Arsenide*. The Journal of Physical Chemistry C, 119(12):6918–6922, 2015. `https://doi.org/10.1021/acs.jpcc.5b02096`.

[91] Beladi-Mousavi, Seyyed Mohsen, Amir Masoud Pourrahimi, Zdeněk Sofer, and Martin Pumera: *Atomically Thin 2D-Arsenene by Liquid-Phased Exfoliation: Toward Selective Vapor Sensing*. Advanced Functional Materials, 29(5):1807004, 2019. https://onlinelibrary.wiley.com/doi/abs/10.1002/adfm.201807004.

[92] Barboza, Ana P. M., Matheus J. S. Matos, Helio Chacham, Ronaldo J. C. Batista, Alan B. de Oliveira, Mario S. C. Mazzoni, and Bernardo R. A. Neves: *Compression-Induced Modification of Boron Nitride Layers: A Conductive Two-Dimensional BN Compound*. ACS Nano, 12(6):5866–5872, 2018. https://doi.org/10.1021/acsnano.8b01911, PMID: 29787237.

[93] Barboza, Ana P. M., Marcos H. D. Guimaraes, Daniel V. P. Massote, Leonardo C. Campos, Newton M. Barbosa Neto, Luiz G. Cancado, Rodrigo G. Lacerda, Helio Chacham, Mario S. C. Mazzoni, and Bernardo R. A. Neves: *Room-Temperature Compression-Induced Diamondization of Few-Layer Graphene*. Advanced Materials, 23(27):3014–3017, 2011. https://onlinelibrary.wiley.com/doi/abs/10.1002/adma.201101061.

[94] Boukhvalov, DW, AN Rudenko, DA Prishchenko, VG Mazurenko, and MI Katsnelson: *Chemical modifications and stability of phosphorene with impurities: a first principles study*. Physical Chemistry Chemical Physics, 17(23):15209–15217, 2015.

[95] Cao, Y., V. Fatemi, S. Fang, K. Watanabe, E. Kaxiras, and P. Jarillo-Herrero: *Unconventional superconductivity in magic-angle graphene superlattices*. Nature, 556:43–50, 2018.

[96] Cao, Y., V. Fatemi, A. Demir, S. Fang, S. L. Tomarken, J. Y. Luo, J. D. Sanchez-Yamagishi, K. Watanabe, T. Taniguchi, E. Kaxiras, R. C. Ashoori, and P. Jarillo-Herrero: *Correlated insulator behaviour at half-filling in magic-angle graphene superlattices*. Nature, 556:80–84, 2018.

[97] S., Chen, M. He, Y. H. Zhang, V. Hsieh, Z. Fei, K. Watanabe, T. Taniguchi, D. H. Cobden, X. Xu, C. R. Dean, and M. Yankowitz: *Electrically tunable correlated and topological states in twisted monolayer-bilayer graphene*. Nature Physics, 17:374–380, 2021.

[98] Katz, Or, Gil Refael, and Netanel H. Lindner: *Optically induced flat bands in twisted bilayer graphene*. Phys. Rev. B, 102:155123, Oct 2020. https://link.aps.org/doi/10.1103/PhysRevB.102.155123.

[99] Kohn, W. and J. M. Luttinger: *New Mechanism for Superconductivity*. Phys. Rev. Lett., 15:524–526, Sep 1965. https://link.aps.org/doi/10.1103/PhysRevLett.15.524.

[100] Bistritzer, Rafi and Allan H. MacDonald: *Moiré bands in twisted double-layer graphene*. Proceedings of the National Academy of Sciences, 108(30):12233–12237, 2011, ISSN 0027-8424. https://www.pnas.org/content/108/30/12233.

[101] Culchac, F. J., R. R. Del Grande, Rodrigo B. Capaz, Leonor Chico, and E. Suárez Morell: *Flat bands and gaps in twisted double bilayer graphene*. Nanoscale, 12:5014–5020, 2020.

[102] Liang, Xia, Zachary A. H. Goodwin, Valerio Vitale, Fabiano Corsetti, Arash A. Mostofi, and Johannes Lischner: *Effect of bilayer stacking on the atomic and electronic structure of twisted double bilayer graphene*. Phys. Rev. B, 102:155146, Oct 2020. https://link.aps.org/doi/10.1103/PhysRevB.102.155146.

[103] Zhao, Xing Ju, Yang Yang, Dong Bo Zhang, and Su Huai Wei: *Formation of Bloch Flat Bands in Polar Twisted Bilayers without Magic Angles*. Phys. Rev. Lett., 124:086401, Feb 2020. https://link.aps.org/doi/10.1103/PhysRevLett.124.086401.

[104] Santos, J. M. B. Lopes dos, N. M. R. Peres, and A. H. Castro Neto: *Graphene Bilayer with a Twist: Electronic Structure*. Phys. Rev. Lett., 99:256802, Dec 2007. https://link.aps.org/doi/10.1103/PhysRevLett.99.256802.

[105] Santos, J. M. B. Lopes dos, N. M. R. Peres, and A. H. Castro Neto: *Continuum model of the twisted graphene bilayer*. Phys. Rev. B, 86:155449, Oct 2012. https://link.aps.org/doi/10.1103/PhysRevB.86.155449.

[106] Haddadi, F., Q. Wu, A. Kruchkov, and O. V. Yazyev: *Moiré Flat Bands in Twisted Double Bilayer Graphene*. Nano Lett., 20:2410–2415, 2020. https://doi.org/10.1021/acs.nanolett.9b05117.

[107] Rickhaus, Peter, Giulia Zheng, Jose L. Lado, Yongjin Lee, Annika Kurzmann, Marius Eich, Riccardo Pisoni, Chuyao Tong, Rebekka Garreis, Carolin Gold, Michele Masseroni, Takashi Taniguchi, Kenji Wantanabe, Thomas Ihn, and Klaus Ensslin: *Gap Opening in Twisted Double Bilayer Graphene by Crystal Fields*. Nano Letters, 19(12):8821–8828, 2019. https://doi.org/10.1021/acs.nanolett.9b03660, PMID: 31670969.

[108] Wu, Fengcheng and Sankar Das Sarma: *Ferromagnetism and superconductivity in twisted double bilayer graphene*. Phys. Rev. B, 101:155149, Apr 2020. https://link.aps.org/doi/10.1103/PhysRevB.101.155149.

[109] Koshino, Mikito: *Band structure and topological properties of twisted double bilayer graphene*. Phys. Rev. B, 99:235406, Jun 2019. https://link.aps.org/doi/10.1103/PhysRevB.99.235406.

[110] Ospina, D.A., C.A. Duque, J.D. Correa, and Eric Suárez Morell: *Twisted bilayer blue phosphorene: A direct band gap semiconductor*. Superlattices and Microstructures, 97:562–568, 2016, ISSN 0749-6036. https://www.sciencedirect.com/science/article/pii/S0749603616305134.

[111] Agnihotri, Shantanu, Maneesh Kumar, Yogesh Singh Chauhan, Amit Agarwal, and Somnath Bhowmick: *Interlayer decoupling in twisted bilayers of β-phosphorus and arsenic: A computational study*. FlatChem, 16:100112, 2019.

[112] Abellán, Gonzalo, Pablo Ares, Stefan Wild, Edurne Nuin, Christian Neiss, David Rodriguez San Miguel, Pilar Segovia, Carlos Gibaja, Enrique G. Michel, Andreas Görling, Frank Hauke, Julio Gómez-Herrero, Andreas Hirsch, and Félix Zamora: *Noncovalent Functionalization and Charge Transfer in Antimonene*. Angewandte Chemie International Edition, 56(46):14389–14394, 2017. https://onlinelibrary.wiley.com/doi/abs/10.1002/anie.201702983.

[113] Yuan, Peiwen, Teng Zhang, Jiatao Sun, Liwei Liu, Yugui Yao, and Yeliang Wang: *Recent progress in 2D group-V elemental monolayers: fabrications and properties*. Journal of Semiconductors, 41(8):081003, 2020.

[114] Gupta, Tushar, Kenan Elibol, Stefan Hummel, Michael Stöger-Pollach, Clemens Mangler, Gerlinde Habler, Jannik C Meyer, Dominik Eder, and Bernhard C Bayer: *Resolving few-layer antimonene/graphene heterostructures*. npj 2D Materials and Applications, 5(1):1–11, 2021.

[115] Singh, Deobrat, Sanjeev K Gupta, Yogesh Sonvane, and Igor Lukačević: *Antimonene: a monolayer material for ultraviolet optical nanodevices*. Journal of Materials Chemistry C, 4(26):6386–6390, 2016.

[116] Li, Likai, Yijun Yu, Guo Jun Ye, Qingqin Ge, Xuedong Ou, Hua Wu, Donglai Feng, Xian Hui Chen, and Yuanbo Zhang: *Black phosphorus field-effect transistors*. Nature nanotechnology, 9(5):372–377, 2014.

[117] Viti, Leonardo, Antonio Politano, and Miriam Serena Vitiello: *Black phosphorus nanodevices at terahertz frequencies: Photodetectors and future challenges*. APL Materials, 5(3):035602, 2017.

[118] Tran, Vy, Ryan Soklaski, Yufeng Liang, and Li Yang: *Layer-controlled band gap and anisotropic excitons in few-layer black phosphorus*. Physical Review B, 89(23):235319, 2014.

[119] Liang, Liangbo, Jun Wang, Wenzhi Lin, Bobby G Sumpter, Vincent Meunier, and Minghu Pan: *Electronic bandgap and edge reconstruction in phosphorene materials*. Nano letters, 14(11):6400–6406, 2014.

[120] Long, Gen, Denis Maryenko, Junying Shen, Shuigang Xu, Jianqiang Hou, Zefei Wu, Wing Ki Wong, Tianyi Han, Jiangxiazi Lin, Yuan Cai, *et al.*: *Achieving ultrahigh carrier mobility in two-dimensional hole gas of black phosphorus*. Nano Letters, 16(12):7768–7773, 2016.

[121] Kuriakose, Sruthi, Taimur Ahmed, Sivacarendran Balendhran, Vipul Bansal, Sharath Sriram, Madhu Bhaskaran, and Sumeet Walia: *Black phosphorus: ambient degradation and strategies for protection*. 2D Materials, 5(3):032001, 2018.

[122] Kripalani, Devesh R, Andrey A Kistanov, Yongqing Cai, Ming Xue, and Kun Zhou: *Strain engineering of antimonene by a first-principles study: mechanical and electronic properties*. Physical Review B, 98(8):085410, 2018.

[123] Kumar, Ashok, Geeta Sachdeva, Ravindra Pandey, and Shashi P Karna: *Optical absorbance in multilayer two-dimensional materials: Graphene and antimonene*. Applied Physics Letters, 116(26):263102, 2020.

[124] Fickert, Michael, Mhamed Assebban, Josep Canet-Ferrer, and Gonzalo Abellán: *Phonon properties and photo-thermal oxidation of micromechanically exfoliated antimonene nanosheets*. 2D Materials, 8(1):015018, 2020.

[125] Kresse, Georg and Jürgen Hafner: *Ab initio molecular dynamics for liquid metals*. Physical review B, 47(1):558, 1993.

[126] Kresse, Georg and Jürgen Hafner: *Ab initio molecular-dynamics simulation of the liquid-metal–amorphous-semiconductor transition in germanium*. Physical Review B, 49(20):14251, 1994.

[127] Kresse, Georg and Jürgen Furthmüller: *Efficient iterative schemes for ab initio total-energy calculations using a plane-wave basis set*. Physical review B, 54(16):11169, 1996.

[128] Kresse, Georg and Jürgen Furthmüller: *Efficiency of ab-initio total energy calculations for metals and semiconductors using a plane-wave basis set*. Computational materials science, 6(1):15–50, 1996.

[129] Blöchl, Peter E: *Projector augmented-wave method*. Physical review B, 50(24):17953, 1994.

[130] Nosé, Shūichi: *A molecular dynamics method for simulations in the canonical ensemble*. Molecular physics, 52(2):255–268, 1984.

[131] Martyna, Glenn J, Michael L Klein, and Mark Tuckerman: *Nosé–Hoover chains: The canonical ensemble via continuous dynamics*. The Journal of chemical physics, 97(4):2635–2643, 1992.

[132] Zouboulis, ES and M Grimsditch: *Raman scattering in diamond up to 1900 K*. Physical Review B, 43(15):12490, 1991.

[133] Taube, A, A Łapińska, J Judek, and M Zdrojek: *Temperature dependence of Raman shifts in layered ReSe2 and SnSe2 semiconductor nanosheets*. Applied Physics Letters, 107(1):013105, 2015.

[134] Late, Dattatray J, Sharmila N Shirodkar, Umesh V Waghmare, Vinayak P Dravid, and CNR Rao: *Thermal expansion, anharmonicity and temperature-dependent Raman spectra of single-and few-layer MoSe2 and WSe2*. ChemPhysChem, 15(8):1592–1598, 2014.

[135] Han, Wei, Pu Huang, Liang Li, Fakun Wang, Peng Luo, Kailang Liu, Xing Zhou, Huiqiao Li, Xiuwen Zhang, Yi Cui, *et al.*: *Two-dimensional inorganic molecular crystals*. Nature communications, 10(1):1–10, 2019.

[136] Late, Dattatray J, Urmimala Maitra, LS Panchakarla, Umesh V Waghmare, and CNR Rao: *Temperature effects on the Raman spectra of graphenes: dependence on the number of layers and doping*. Journal of Physics: Condensed Matter, 23(5):055303, 2011.

[137] Sahoo, Satyaprakash, Anand PS Gaur, Majid Ahmadi, Maxime J F Guinel, and Ram S Katiyar: *Temperature-dependent Raman studies and thermal conductivity of few-layer MoS2*. The Journal of Physical Chemistry C, 117(17):9042–9047, 2013.

[138] Late, Dattatray J: *Temperature dependent phonon shifts in few-layer black phosphorus*. ACS Applied Materials & Interfaces, 7(10):5857–5862, 2015.

[139] Luo, Siwei, Xiang Qi, Hao Yao, Xiaohui Ren, Qiong Chen, and Jianxin Zhong: *Temperature-dependent Raman responses of the vapor-deposited tin selenide ultrathin flakes*. The Journal of Physical Chemistry C, 121(8):4674–4679, 2017.

[140] Barboza, Ana PM, Alan CR Souza, Matheus JS Matos, Juliana C Brant, Tiago C Barbosa, Helio Chacham, Mario SC Mazzoni, and Bernardo RA Neves: *Graphene/h-BN heterostructures under pressure: From van der Waals to covalent*. Carbon, 155:108–113, 2019.

[141] Zhao, Zhisheng, Bo Xu, and Yongjun Tian: *Recent advances in superhard materials*. Annu. Rev. Mater. Res, 46(1):383–406, 2016.

[142] Balandin, Alexander A: *Thermal properties of graphene and nanostructured carbon materials*. Nature materials, 10(8):569–581, 2011.

[143] Chernozatonskii, Leonid Alexandrovich, Pavel Borisovich Sorokin, Alexander Gennadievich Kvashnin, and Dmitrii Gennad'evich Kvashnin: *Diamond-like C2H nanolayer, diamane: simulation of the structure and properties*. Jetp Letters, 90(2):134–138, 2009.

[144] Chernozatonskii, Leonid A, Pavel B Sorokin, Alexander A Kuzubov, Boris P Sorokin, Alexander G Kvashnin, Dmitry G Kvashnin, Pavel V Avramov, and Boris I Yakobson: *Influence of size effect on the electronic and elastic properties of diamond films with nanometer thickness*. The Journal of Physical Chemistry C, 115(1):132–136, 2011.

[145] Barboza, Ana PM, Marcos HD Guimaraes, Daniel VP Massote, Leonardo C Campos, Newton M Barbosa Neto, Luiz G Cancado, Rodrigo G Lacerda, Helio Chacham, Mario SC Mazzoni, and Bernardo RA Neves: *Room-temperature compression-induced diamondization of few-layer graphene*. Advanced Materials, 23(27):3014–3017, 2011.

[146] Gao, Yuchen, Jianguo Jiang, Yuan Meng, Feng Yan, and Aikelaimu Aihemaiti: *A review of recent developments in hydrogen production via biogas dry reforming*. Energy Conversion and Management, 171:133–155, 2018.

[147] Piazza, Fabrice, Kathleen Gough, Marc Monthioux, Pascal Puech, Iann Gerber, Richard Wiens, Germercy Paredes, and Cristhofer Ozoria: *Low temperature, pressureless sp2 to sp3 transformation of ultrathin, crystalline carbon films*. Carbon, 145:10–22, 2019.

[148] Novoselov, KS and AH Castro Neto: *Two-dimensional crystals-based heterostructures: materials with tailored properties*. Physica Scripta, 2012(T146):014006, 2012.

[149] Britnell, Liam, Ricardo Mendes Ribeiro, Axel Eckmann, Rashid Jalil, Branson D Belle, Artem Mishchenko, Y J Kim, Roman V Gorbachev, Thanasis Georgiou, Sergei V Morozov, *et al.*: *Strong light-matter interactions in heterostructures of atomically thin films*. Science, 340(6138):1311–1314, 2013.

[150] Withers, Freddie, Del Pozo-Zamudio, A Mishchenko, AP Rooney, Ali Gholinia, K Watanabe, T Taniguchi, Sarah J Haigh, AK Geim, AI Tartakovskii, *et al.*: *Light-emitting diodes by band-structure engineering in van der Waals heterostructures*. Nature materials, 14(3):301–306, 2015.

[151] Iannaccone, Giuseppe, Francesco Bonaccorso, Luigi Colombo, and Gianluca Fiori: *Quantum engineering of transistors based on 2D materials heterostructures*. Nature nanotechnology, 13(3):183–191, 2018.

[152] Dean, Cory R, L Wang, P Maher, C Forsythe, Fereshte Ghahari, Y Gao, Jyoti Katoch, M Ishigami, P Moon, M Koshino, *et al.*: *Hofstadter's butterfly and the fractal quantum Hall effect in moiré superlattices*. Nature, 497(7451):598–602, 2013.

[153] Zomer, PJ, MHD Guimarães, JC Brant, N Tombros, and BJ Van Wees: *Fast pick up technique for high quality heterostructures of bilayer graphene and hexagonal boron nitride*. Applied Physics Letters, 105(1):013101, 2014.

[154] Barboza, APM, AP Gomes, BS Archanjo, PT Araujo, A Jorio, AS Ferlauto, H Chacham, BRA Neves, *et al.*: *Deformation induced semiconductor-metal transition in single wall carbon nanotubes probed by electric force microscopy*. Physical review letters, 100(25):256804, 2008.

[155] Troullier, Norman and José Luís Martins: *Efficient pseudopotentials for plane-wave calculations*. Physical review B, 43(3):1993, 1991.

[156] Kleinman, Leonard and DM Bylander: *Efficacious form for model pseudopotentials*. Physical Review Letters, 48(20):1425, 1982.

[157] Weaire, D and MF Thorpe: *Electronic properties of an amorphous solid. I. A simple tight-binding theory*. Physical Review B, 4(8):2508, 1971.

[158] Bardeen, J and W Shockley: *Deformation potentials and mobilities in non-polar crystals*. Physical review, 80(1):72, 1950.

Appendix

APPENDIX A – The Verlet algorithm

To obtain the basic formula for the Verlet algorithm [36] we write the Taylor series expansion for $R_I(t+\Delta t)$:

$$R_I(t+\Delta t) = R_I(t) + \Delta t \frac{dR_I}{dt} + \frac{(\Delta t)^2}{2!}\frac{d^2R_I}{dt^2} + O[\Delta t^3]. \tag{A.1}$$

and similarly for $R_I(t-\Delta t)$

$$R_I(t-\Delta t) = R_I(t) - \Delta t \frac{dR_I}{dt} + \frac{(\Delta t)^2}{2!}\frac{d^2R_I}{dt^2} + O[\Delta t^3]. \tag{A.2}$$

Keeping only the second order terms, adding the two above equations, and using equation 1.28:

$$R_I(t+\Delta t) + R_I(t-\Delta t) = 2R_I(t) + \frac{(\Delta t)^2}{M_I}F_I[\{R_J\}], \tag{A.3}$$

or

$$R_I(t+\Delta t) = 2R_I(t) - R_I(t-\Delta t) + \frac{(\Delta t)^2}{M_I}F_I[\{R_J\}], \tag{A.4}$$

and in vector form:

$$\mathbf{R}_I(t+\Delta t) = 2\mathbf{R}_I(t) - \mathbf{R}_I(t-\Delta t) + \frac{(\Delta t)^2}{M_I}\mathbf{F}_I[\{\mathbf{R}_J\}. \tag{A.5}$$

APPENDIX B – Mobility calculations

To calculate the mobility of the antimonene ribbons we first calculated the electron and hole effective masses by fitting a parabolic curve in the valence band maximum (VBM) and conduction band minimum (CBM) (Fig. B-(b)) for the monolayer antimonene nanochain:

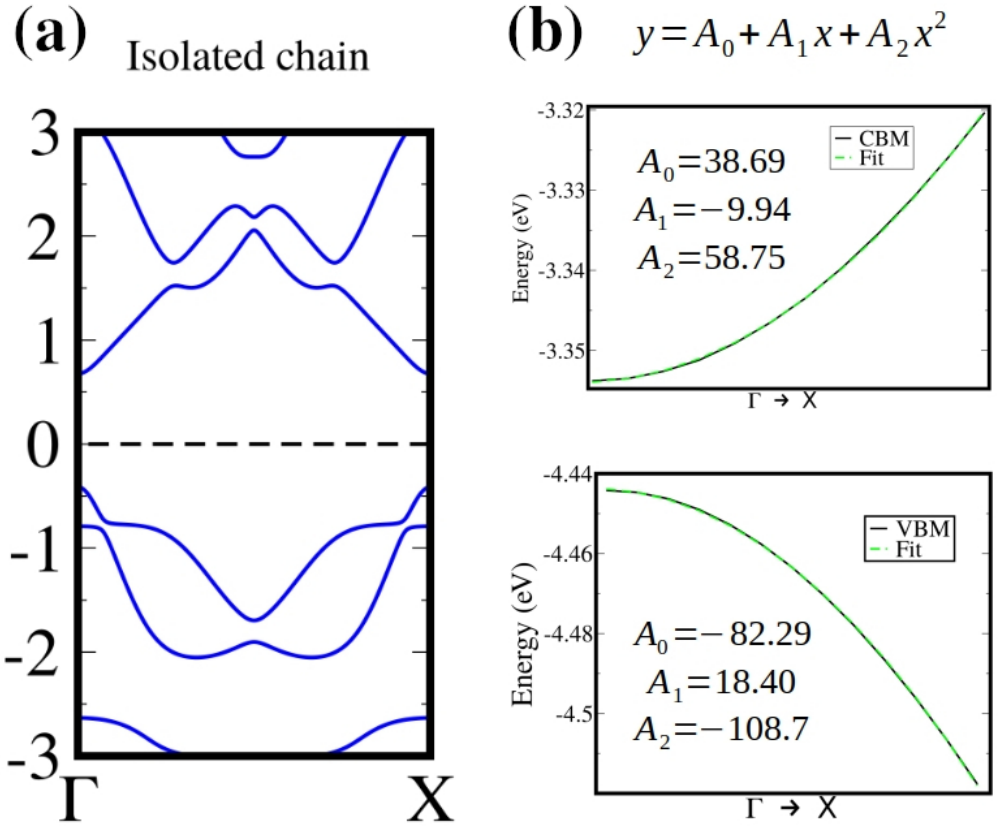

Figure B.1 – (a) The electronic bandstructure of the antimonene nanochain obtained from the monolayer . (b) The secod order fit for the VBM (top) and CBM (bottom). Units are omitted.

We calculated the effective masses for the hole and electron using:

$$\frac{1}{m^*} = \frac{1}{\hbar^2}\frac{\partial^2 E}{\partial k^2}, \tag{B.1}$$

and obtained m_h^* = 0.229 m_e and m_e^* = 0.125 m_e for the hole and electron effective mass, respectively. We calculated the mobility by using deformation potential formalism for 1D systems [87, 158]:

$$\mu = \frac{e\hbar^2 C}{\sqrt{2k_b T}|m^*|^{3/2}E_1^2} \tag{B.2}$$

in which the elastic modulus C is defined as the second derivative of the total energy E relative to the applied strain ε divided by the area S_0 of the optimized structure. The strain is give by

the relative change of the lattice vector, $\varepsilon = \frac{L-L_0}{L_0}$. The deformation potential E_1 is the derivative $\frac{\partial E_b}{\partial \varepsilon}$, in which E_b is the energy of the top of the valence bands for holes or the bottom of the conduction band for electrons. Finally, we adopted the temperature T = 300 K in the calculations.

We performed several calculations varying the lattice parameter (i.e. applying strain in the nanochain):

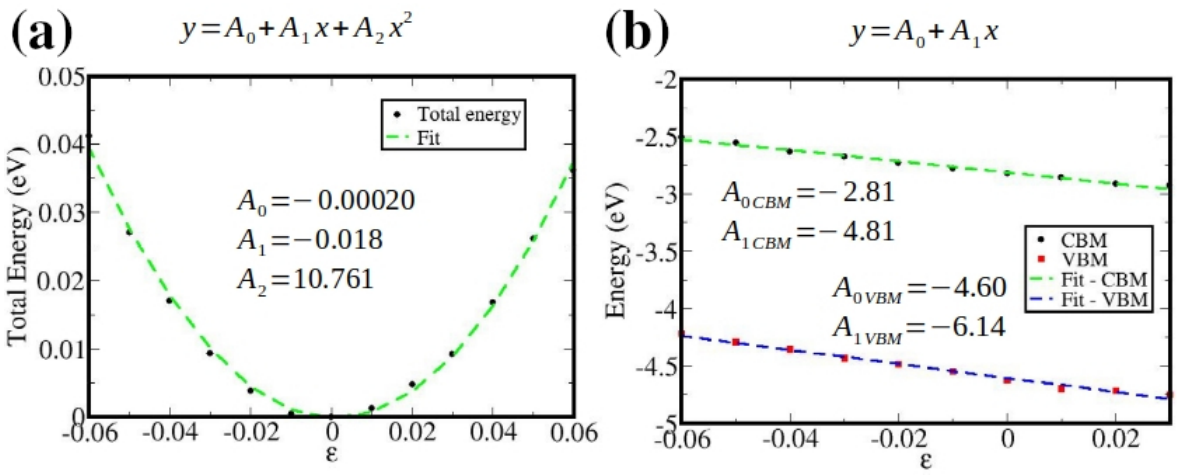

Figure B.2 – (a) The total energy (minus the ground state total energy) calculated for each nanochain under the strain ε. (b) The VBM (top) and CBM (bottom) energies for several strain ε. Units are omitted.

Using the second order fit for the total energy versus strain curves (Fig. B.2-(a)) we can calculate the elastic modulus C. Using the linear fit for the energy band versus strain (Fig. B.2-(b)) we can calculate the deformation potential E_1. We summarize all the calculated parameters for the nanorribons generated by the mono- and bilayer antimonene and for the nanoribbon obtained from the arsenene bilayer in the table 2:

Table 2 – All parameters obtained for the mobility calculations.

Structure	Type	$\lvert m_x \rvert$ (m_e)	C (eV A^{-1})	$\lvert E_1 \rvert$ (eV)	μ (cm^2 V^{-1} s^{-1})
Sb nanochain from monolayer	Hole	0.229	5.48	4.81	17.11
	Electron	0.125		6.14	26.04
Sb nanoribbon from bilayer	Hole	0.143	16.00	5.82	69.18
	Electron	0.150		9.48	24.27
As nanoribbon from bilayer	Hole	0.132	23.988	6.60	90.92
	Electron	0.161		11.41	22.58